Dipl.-Ing. Christoph M. Monsberger

Distributed Fiber Optic Shape Sensing in Structural and Geotechnical Engineering: Principles and Applications

DOCTORAL THESIS

to achieve the university degree of

Doktor der technischen Wissenschaften

submitted to

Graz University of Technology

Supervisor

Univ.-Prof. Dr.techn. Werner Lienhart

Institute of Engineering Geodesy and Measurement Systems

Graz, September 2022

AFFIDAVIT

I declare that I have authored this thesis independently, that I have not used other than the declared sources/resources, and that I have explicitly indicated all material which has been quoted either literally or by content from the sources used. The text document uploaded to TUGRAZonline is identical to the present doctoral thesis.

Date, Signature

Abstract

Civil structural health monitoring (CSHM) has become significantly more important within the last decades due to rapidly growing demand on new constructions world-wide with respect to limited space and increased sustainability, as well as longer service lifetimes of existing structures. Knowledge about the structural performance and health condition is essential to plan and design condition-based maintenance works. State-of-the-art monitoring techniques, including displacement readings at the surface (total stations, GNSS, laser scanning, etc.), internal deformation sensors (strain gauges, tilt sensors, etc.) as well as manual or image-based visual inspections, often have limitations, either in the spatial or the temporal resolution. As a consequence, local structural deficiencies might be identified belatedly or even overlooked completely.

This thesis introduces enhanced monitoring concepts for structural and geotechnical applications based on distributed fiber optic sensing (DFOS). The distributed strain sensing feature is combined

with geodetic techniques and one-dimensional displacement sensors to analyze fully-distributed curvature and bending profiles along civil structures, where the optical fibers are directly embedded inside or attached along the structure. Corresponding sensing and evaluation algorithms as well as basic characteristics of different fiber optic sensing technologies are addressed. General DFOS capabilities are demonstrated through sensor calibration results and laboratory tests on the spatial resolution.

Various applications are presented, in which individually developed approaches have been integrated into real-scale structures using different DFOS sensors and installation techniques. These include linear objects with different material composition like grouted steel anchors or concrete beams and curved structures such as tunnel linings. The installations were interrogated using fully-distributed sensing units based on Rayleigh and Brillouin scattering as well as quasi-distributed fiber Bragg grating (FBG) interrogators.

The suitability of different designs is validated within laboratory experiments, where the results are proven using pointwise displacement transducers, geodetic measurements and image-based sensing techniques. It is shown that relative errors between the independent technologies can be achieved in the sub-millimeter range, depending on the DFOS system design and sensing principle. Practical realizations and autonomous monitoring campaigns on-site also demonstrate the capabilities in field environment.

Zusammenfassung

Die zuverlässige Überwachung strukturrelevanter Parameter gewinnt in den letzten Jahrzehnten ständig an Bedeutung, nicht zuletzt infolge des weltweit steigenden Bedarfs an neuer Infrastruktur mit eingeschränkten Umsetzungsräumen und zusätzlichen Anforderungen hinsichtlich Nachhaltigkeit sowie der Erhöhung der Nutzungsdauer bestehender Bauwerke. Informationen über die strukturelle Beschaffenheit und den Zustand sind zur Planung vorausschauender Erhaltungsmaßnahmen essentiell. Konventionelle Überwachungssysteme wie z.B. Verschiebungsmessungen an der Oberfläche (Totalstation, GNSS, Laserscanning, etc.), interne Deformationsmessungen (Dehnungsaufnehmer, Neigungssensoren, etc.) oder manuelle und bildbasierte Inspektionen zeigen häufig Limitationen in der räumlichen Auflösung bzw. der Messfrequenz, weshalb lokale strukturelle Defizite erst spät oder gar nicht erkannt werden können.

In dieser Dissertation werden erweiterte Anwendungskonzepte zum strukturellen und geotechnischen Monitoring basierend auf

verteilten faseroptischen Sensoren behandelt. Die Eigenschaft der verteilten Dehnungsmessung wird mit geodätischen Messmethoden sowie eindimensionalen Verschiebungssensoren kombiniert, um eine kontinuierliche Beurteilung von Krümmungs- und Biegeprofilen entlang von Strukturen abzuleiten. Die optische Glasfaser ist hierbei direkt im Bauwerk integriert oder an der Oberfläche appliziert. Entsprechende Auswertealgorithmen und grundsätzliche Eigenschaften faseroptischer Sensorsysteme werden im Rahmen der Arbeit diskutiert. Zugehörige Sensorkalibrierungen und Laboruntersuchungen im Bezug auf die räumliche Diskretisierung zeigen allgemeine Fähigkeiten verteilter faseroptischen Systeme.

Die Anwendungsbeispiele präsentieren individuell entwickelte Konzepte mit unterschiedlichen Sensortypen und Installationstechniken, welche in Infrastrukturbauwerke im Realmaßstab integriert wurden. Diese inkludieren lineare Objekte mit unterschiedlichen Materialen (mantelverpresste Stahlstabanker oder Betonbalken) sowie Strukturen mit initial gekrümmter Form (Tunnelschalen). Die Instrumentierungen wurden sowohl mit verteilten faseroptischen Messsystemen basierend auf der Rayleigh und Brillouin-Streuung als auch mit quasi-verteilten Faser-Bragg-Gittern umgesetzt.

Die Eignung der entwickelten Designs wird anhand verschiedener Laborexperimente untersucht, in welchen die faseroptischen Ergebnisse mit punktweisen Wegaufnehmern, geodätischen Messungen und bildbasierten Methoden verifiziert werden. Dabei können, je nach faseroptischem Systemdesign und Messprinzip, relative Fehler zwischen den unabhängigen Messmethoden im Sub-Millimeter erreicht werden. Die praktischen Realisierungen sowie die Durchführung autonomer Messkampagnen beweisen die Einsatzfähigkeiten unter Baustellenbedingungen.

Acknowledgments

Writing this dissertation has been a special journey, a journey that would not have been possible without the support of many people to whom I would like to express my gratitude.

Special thanks to my wife Yvonne, not only for your moral support throughout this time, but also for numerous valuable discussions on different constructional aspects. Questions like "Was bringt das dem Auftraggeber?" (engl.: Where is the benefit for the client?) made me rethink different sensing concepts, and brought the practical feasibility and usability into this scientific work. Thank you for standing by my side, for motivating me, especially in the final phase. I would not have made it without you.

I would like to thank my supervisor Prof. Werner Lienhart for inspiring me to pursue structural health monitoring and fiber optic sensing over the last years and for the opportunity to realize this thesis at his institute. He made me responsible for multiple research

projects and gave me the freedom to design and develop individual concepts for different structures in my own way. I also acknowledge his useful advice and input on the scientific publications this thesis is based on.

Thanks to Prof. Branko Glišić from Princeton University, certainly a pioneer in the field of fiber optic strain sensors for civil infrastructure. Beside others, his implemented research and corresponding papers motivated me to realize distributed fiber optic shape sensing concepts. He has also agreed to review this thesis as an external expert and provided me with valuable comments.

Last, but not least, thanks to my former IGMS colleagues for numerous joyful hours in mostly stressful times and their efforts during sensor installations. I particularly would like to acknowledge the contribution of Ing. Dietmar Denkmaier, who accompanied me to various Austrian and international construction sites and always provided useful input to different designs with his experienced knowledge for mechanical manufacturing. Finally, I appreciate the work of Mag. Cordelia Gehrer, who proofread the thesis and brought my technical English up to scratch.

Contents

Symbols

C_ε	strain sensitivity coefficient
C_T	temperature sensitivity coefficient
d	distance
dx	segment length
Δz	spatial resolution
E	modulus of elasticity
ε	strain
h	distance between sensors
I_y	moment of inertia
κ	curvature
Λ	periodic change of refractive index
λ	wavelength

M	bending moment
N	normal equation matrix
n	refractive index
ν	frequency
φ	orientation angle
R	bending radius
σ	stress or standard deviation
T	temperature
w	deflection or displacement
x	position or segment

Acronyms

1D	one-dimensional
2D	two-dimensional
3D	three-dimensional
ANDRA	French national radioactive waste management agency
BOFDA	Brillouin Optical Frequency Domain Analyzer
BOFDR	Brillouin Optical Frequency Domain Reflectometry
BOTDA	Brillouin Optical Time Domain Analyzer
BOTDR	Brillouin Optical Time Domain Reflectometry
CSHM	Civil Structural Health Monitoring
DAS	Distributed Acoustic Sensing
DFOS	Distributed Fiber Optic Sensing

DIC	Digital Image Correlation
DTG	Draw Tower Grating
EFPI	Extrinsic Fabry-Perot Interferometry
FBG	Fiber Bragg Grating
FDM	Finite Difference Methods
FEM	Finite Element Method
FiMT	Fiber in Metal Tube
GNSS	Global Navigation Satellite System
IGMS	Institute of Engineering Geodesy and Measurement Systems, Graz University of Technology
LPG	Long Period Grating
LVDT	Linear Variable Differential Transducers
MAV	Moving AVerage
MCF	Multi-Core Optical Fibers
MUL	Montanuniversität Leoben
NATM	New Austrian Tunneling Method
OBR	Optical Backscatter Reflectometer
OFDR	Optical Frequency Domain Reflectometry
OTDR	Optical Time Domain Reflectometry
SBT	Semmering Base Tunnel
SMF	Single Mode Fiber
SOFO	Surveillance d'Ouvrages par Fibre Optique (engl. Structural Monitoring with Fiber Optic)
TB	Tight Buffered
TBM	Tunnel Boring Machine
TS	Total Station
TSS	Total Sum of Squares
TW-COTDR	Tunable Wavelength Coherent Optical Time Domain Reflectometry

UV	Ultra Violet
VWS	Vibrating Wire Sensors

List of Relevant Publications

Publications relevant for this thesis in chronological order.

C. M. Monsberger et al. (2016). "Deformation measurement of a driven pile using distributed fibre-optic sensing." *Journal of Applied Geodesy* 10(1): 61–69

C. M. Monsberger and W. Lienhart (2019). "Design, Testing, and Realization of a Distributed Fiber Optic Monitoring System to Assess Bending Characteristics Along Grouted Anchors." *Journal of Lightwave Technology* 37(16): 4603–4609

F. Buchmayer et al. (2021). "Advantages of tunnel monitoring using distributed fibre optic sensing." *Journal of Applied Geodesy* 15(1): 1–12

C. M. Monsberger and W. Lienhart (2021a). "Distributed fiber optic shape sensing along shotcrete tunnel linings: Methodology, field applications, and monitoring results." *Journal of Civil Structural Health Monitoring* 11(2): 337–350

C. M. Monsberger and W. Lienhart (2021b). "Distributed Fiber Optic Shape Sensing of Concrete Structures." *Sensors* 21(18): 6098

C. M. Monsberger et al. (2022). "Large-scale distributed fiber optic sensing network for short and long-term integrity monitoring of tunnel linings." *Journal of Civil Structural Health Monitoring*

1 Introduction

Aging infrastructure in combination with rapidly growing construction volume worldwide involves challenging conditions for civil engineering structures. Appropriate designs as well as suitable construction processes are therefore indispensable to ensure safe structures and reliable operations. Civil structural health monitoring (CSHM) has become a powerful procedure to assess the structural integrity. While a number of parameters can be monitored for that purpose, deformation is particularly important as it directly reflects structural performance and health condition. An adequate sensor selection and placement as well as the combination of different sensing technologies with respect to the deformation behavior represent the key factors to develop a cost-efficient and finally, successful CSHM approach.

1.1 DEFORMATION MONITORING AND SENSING TECHNIQUES

Displacement can be generally classified into rigid body movement and deformation of civil infrastructure (DIN 2010). While the first one expects a rigid motion of the entire object (i.e. translation and rotation), which does not change the inner geometry, deformation like strain, shear strain, bending or torsion do alter geometric relationships between object points (c.f. Figure 1.1). Conversions between the different components of displacement or deflection are feasible by differentiation or integration, respectively. This however either essentially increases the signal to noise ratio (differentiation) or requires well-known boundary conditions (integration), where the resulting accuracy strongly depends on the stability of supporting points.

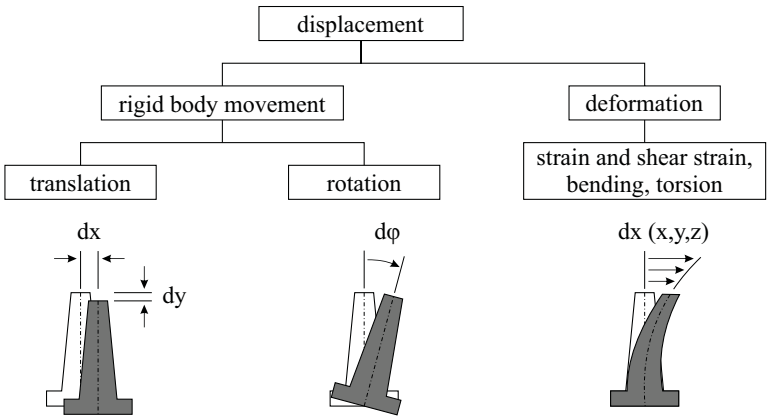

Figure 1.1: Classification of displacement of civil infrastructure (based on DIN 2010; Heunecke et al. 2013)

CSHM techniques to monitor the structural behavior range from electro-optical and electro-mechanical sensors to acoustic emission, fiber optics, remote sensing and imaging techniques as well as vibration measurements (Karbhari and Ansari 2009). A comprehensive

review of methodologies for civil engineering applications and their respective sensing principle is given in DGGT (2021).

At this point, the variety of sensing techniques is subsequently restricted to sensors capturing geometrical quantities, which may be further classified and split into internal and external sensors. The latter ones are usually associated with traditional geodetic techniques, i.e. total stations, leveling systems, laser scanning, satellite-based GNSS (Global Navigation Satellite System) or even with image-based sensing techniques and displacement sensors. These allow an assessment of rigid body motions and deliver absolute displacements along the structure. Internal sensors can be placed either along the surface or directly embedded inside structure and enable monitoring of inner structural distortions like strains or local tilts changes, which can be further related to stress, bending or rotation of the structure itself.

Both sensor types provide advantages but also have limitations, depending on the monitoring design and the required output. Integrated sensor systems with combination of various individual sensors and conversion between different deformation events can therefore be beneficial to gain more sophisticated knowledge about the deformation behavior or to supply additional observations for further derivations within data analysis.

1.2 MOTIVATION AND OBJECTIVE

Curvature and bending characteristics along civil infrastructure can supply valuable information to compare the actual condition, including, for instance, damages and fatigue, to the construction and design state. Absolute external sensors like geodetic or image-based techniques are however often limited for in-situ monitoring due to the fact that they always require a direct line of sight between the measured object and the instrument. Even if conventional internal sensors can provide information without visual contact, the number of sensing points and the sensing range is usually restricted.

Distributed fiber optic sensing (DFOS) has significantly evolved in recent years to monitor large scale civil infrastructure. Applications range from monitoring of bridges (Matta et al. 2008; Minardo et al. 2012; Regier and Hoult 2014; Webb et al. 2017) to high-rise buildings (De Battista et al. 2019), reinforced earth structures (Moser et al. 2016), pipelines (Klais et al. 2017; Feng et al. 2018) and tunnels (Li et al. 2018; Lienhart et al. 2019; Wagner et al. 2020; Buchmayer et al. 2021). The technology can provide distributed, continuous strain and temperature measurements with high accuracy and high spatial resolution over kilometers, where the sensing fiber is directly embedded inside or attached along the structure. This not only allows the detection of in-situ damages and failures like cracks or leakages, but also an assessment of the deformation behavior over time for condition-based maintenance.

The distributed strain sensing feature in combination with the high spatial resolution also provides new and optimized capabilities for in-situ shape sensing by integrating the DFOS strain-based information. Shape deformation can be interpreted in this context as the three-dimensional (3D) geometric change of the relationship between object coordinates due to strain, bending or torsion (c.f. Figure 1.1). An appropriate combination of the shape information with external point-wise sensors capturing rigid body movement can further enable fully-distributed displacement sensing.

The objective of this thesis is therefore to design, evaluate and realize suitable shape sensing concepts for structural and geotechnical applications, including beam-like structures as occurring in bridges, tube/pillar objects like piles or grouted anchors as well as curved structures such as tunnel linings. For this purpose, distributed fiber optic strain sensing is combined with geodetic techniques and one-dimensional (1D) displacement sensors. The suitability of different designs is validated within laboratory experiments, where the results are proven using, inter alia, pointwise displacement readings, total station measurements and distributed image-based monitoring, and compared to theoretical beam models. The field appli-

cation capabilities are demonstrated by various autonomous monitoring campaigns of real-scale structures.

1.3 OUTLINE OF THE THESIS

The thesis is written in a cumulative manner and based on six publications. Figures, texts and contents of these manuscripts have been incorporated into the main text and supplemented with additional theoretical background information, laboratory experiments as well as further studies on the field applications. The related publications are listed in the disclaimer before each chapter.

Chapter 2 introduces the curvature sensing principle based on the Euler-Bernoulli bending theory and discusses different numerical integration methods. Limitations of quasi and fully-distributed strain sensors are theoretically analyzed with respect to the number of sensing points and the spatial distribution of the curvature.

Chapter 3 addresses basic characteristics of different fiber optic sensing techniques for monitoring in civil engineering, including quasi-distributed fiber Bragg gratings (FBGs) as well as fully-distributed fiber optic systems. Sensor calibration results and laboratory investigations on the spatial resolution impact demonstrate general DFOS capabilities in practical applications.

Chapter 4 to 6 present the design and practical realization of shape sensing approaches in different structural and geotechnical applications. Bending characteristics along grouted steel anchors are analyzed in Chapter 4. The study covers detailed laboratory tests with independent image-based and geodetic verification measurements as well as an autonomous monitoring campaign in practical environment on-site.

Chapter 5 introduces a distributed fiber optic shape sensing and evaluation concept, which utilizes DFOS strain measurements in combination with point-wise geodetic displacement readings for fully distributed shape assessment along curved structures, such as tunnels. The capabilities of the designed algorithm are discussed

by means of stochastic analysis. Results of realized installations at shotcrete tunnel cross-sections as well as shaft linings at a railway tunnel currently under construction demonstrate the field application suitability.

Chapter 6 discusses a comprehensive analysis of distributed fiber optic shape sensing of concrete structures, including numerous beams with different sensor types and installation techniques as well as pre-cast tunnel lining segments in real-scale. Results of FBG sensors and fully-distributed interrogation units are verified using, inter alia, pointwise displacement readings and distributed image-based measurements.

Chapter 7 summarizes the findings of the thesis, presents a general workflow to realize successful distributed fiber optic shape sensing approaches along civil infrastructure and provides an outlook on potential future applications.

2

Strain-based Shape Sensing Principles

Disclaimer

This chapter is based on the publications listed below. Figures, texts and contents are therefore already partly or fully published.

C. M. Monsberger and W. Lienhart (2021a). "Distributed fiber optic shape sensing along shotcrete tunnel linings: Methodology, field applications, and monitoring results." *Journal of Civil Structural Health Monitoring* 11(2): 337–350

C. M. Monsberger and W. Lienhart (2021b). "Distributed Fiber Optic Shape Sensing of Concrete Structures." *Sensors* 21(18): 6098

2.1 INTRODUCTION

Strain transducers like strain gauges or fiber optic sensors are widely used in civil structural health monitoring to assess structural characteristics on the surface or inside objects. The measurements basically deliver one-dimensional strains ε in the axis of the sensor, but can be directly related to longitudinal stresses σ along the object using the modulus of elasticity E:

$$\sigma = E \cdot \varepsilon \tag{2.1}$$

This linear strain-stress relation is solely applicable under assumption of elastic material behavior based on Hooke's law. The 1D sensor information can be further utilized to prove assumed parameters of structural models like the Finite Element Method (FEM).

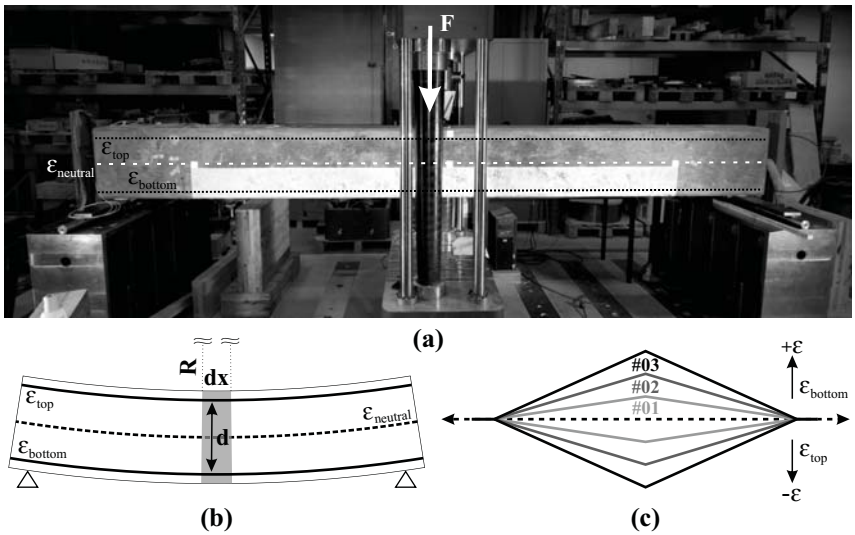

Figure 2.1: Concrete beam under vertical loading: **(a)** Laboratory test setup. **(b)** Schematic representation of curved beam. **(c)** Theoretical strain profiles along top and bottom layer for different loading steps #01 to #03.

If two or more strain sensors are appropriately arranged along the structure, information orthogonal to the sensor axis, i.e. curvature characteristics due to bending of the object and thus two-dimensional (2D) information, can also be determined from the measured strain values. As an example, Figure 2.1 depicts the laboratory test setup of a simply supported concrete beam structure, which is exposed to vertical, transverse loading. The floating bearing system shall result in non-bending-related strain $\varepsilon_{neutral}$ along the neutral axis of the beam. However, sensors in two different planes of the beam, e.g. equidistantly spaced to the neutral axis as depicted in Figure 2.1b, are expected to present negative strain along the top layer ε_{top} and positive strain along the bottom layer ε_{bottom} as a result of the beam's bending. These different strain characteristics form the basis for strain-based shape sensing approaches.

This chapter introduces the curvature sensing principle based on the Euler-Bernoulli bending theory and presents shape sensing algorithms using quasi or fully distributed strain measurements along objects. Their restrictions in the curvature determination with respect to limitations in the number of sensing points as well as the spatial resolution in conjunction with the spatial distribution of the curvature are discussed to provide a general assessment of the shape sensing capabilities.

2.2 EULER-BERNOULLI BENDING THEORY

It is known from elastic bending theory (e.g. Megson 2005) that the deflection w at one specific sensing location x along an object can be described by

$$w(x) = \int\int \frac{M(x)}{E \cdot I_y}\, dx^2 = \int\int \kappa(x)\, dx^2 \tag{2.2}$$

where M is the bending moment and I_y the moment of inertia at the observed position. The deflection w can also be expressed by the local curvature value κ and, therefore, by the bending ra-

dius R. At this point, the relation between the bending radius and the measured strains along the different layers in combination with the distance between the sensors d can be used to directly assess the curvature characteristics at position x:

$$\kappa(x) = \frac{1}{R(x)} = \frac{\varepsilon_{top}(x) - \varepsilon_{bottom}(x)}{d(x)} \tag{2.3}$$

Beside influencing shear stresses, the civil infrastructure object might also be affected by longitudinal stresses, exemplary due to fatigue, shrinkage, creepage or temperature-induced expansion. These effects are taken into account by the longitudinal strain in the centroid of the cross-section $\varepsilon_{neutral}$:

$$\kappa(x) = \frac{\varepsilon_{top}(x) - \varepsilon_{bottom}(x)}{d(x) \cdot (1 + \varepsilon_{neutral}(x))} \tag{2.4}$$

The centroid strain can be equal to the mean strain $\overline{\varepsilon}$ of both sensing layers, if these are equidistantly spaced to the neutral axis:

$$\varepsilon_{neutral}(x) = \overline{\varepsilon} = \frac{1}{2} \cdot (\varepsilon_{top} + \varepsilon_{bottom}) \tag{2.5}$$

The curvature determination can be basically carried out without any knowledge of the object's material properties. However, it is assumed that the individual shape of the cross-section within one sensing element dx remains constant based on the Bernoulli hypothesis, see e.g. Mang and Hofstetter (2018). This might especially be crucial for aging infrastructure or concrete structures with high degree of damage, where systematic deviations can arise in the curvature derivation since the assumption can only be partially fulfilled.

2.3 INTEGRATION METHODS

The measured strains enable the direct curvature assessment at specific locations along the object, but do not deliver an instant relation to displacements orthogonal to the sensing direction. For this, the derived curvature values can be numerically double-integrated to determine the deformed shape of the object. Different numerical integration methods are known in literature, which range from techniques based on difference equation to rectangle and trapezoidal rule integration (Nassif and Fayyad 2013).

Finite Difference Methods (FDM) utilize numerical finite differences to approximate derivatives of functions and are commonly used in numerical analysis to solve difference equations. As already introduced by Pei et al. (2013), the relation between the curvature κ at the i-th sensor position along an object and the displacement value w can be described by

$$\kappa_i = \frac{1}{h^2} \cdot (w_{i+1} - 2 \cdot w_i + w_{i-1}) \tag{2.6}$$

where h is the spatial distance between the sensors, which is assumed to be consistent along the object. In other words, the distance between point-wise sensors must be constant or distributed strain sensing techniques must be used. Based on Equation 2.6, the linear model is given by

$$\overbrace{\begin{bmatrix} \kappa_1 \\ \kappa_2 \\ \vdots \\ \kappa_{n-1} \\ \kappa_n \end{bmatrix}}^{\boldsymbol{\kappa}} = \overbrace{\begin{bmatrix} \frac{1}{h^2} & \frac{-2}{h^2} & \frac{1}{h^2} & 0 & \cdots & \cdots & \cdots & \cdots & 0 \\ 0 & \frac{1}{h^2} & \frac{-2}{h^2} & \frac{1}{h^2} & 0 & \ddots & \ddots & \ddots & 0 \\ \vdots & \ddots & \ddots & \ddots & \ddots & \ddots & \ddots & \ddots & \vdots \\ \vdots & \ddots & \ddots & \ddots & \ddots & \frac{1}{h^2} & \frac{-2}{h^2} & \frac{1}{h^2} & 0 \\ 0 & \cdots & \cdots & \cdots & \cdots & 0 & \frac{1}{h^2} & \frac{-2}{h^2} & \frac{1}{h^2} \end{bmatrix}}^{\boldsymbol{A}} \cdot \overbrace{\begin{bmatrix} w_0 \\ w_1 \\ \vdots \\ w_n \\ w_{n+1} \end{bmatrix}}^{\boldsymbol{w}} \tag{2.7}$$

$$\Sigma_{\kappa\kappa} = \begin{bmatrix} \sigma^2_{\kappa_1} & 0 & \cdots & 0 & 0 \\ 0 & \sigma^2_{\kappa_2} & \cdots & 0 & 0 \\ \vdots & \vdots & \ddots & \vdots & \vdots \\ 0 & 0 & \cdots & \sigma^2_{\kappa_{n-1}} & 0 \\ 0 & 0 & \cdots & 0 & \sigma^2_{\kappa_n} \end{bmatrix} \tag{2.8}$$

where $\Sigma_{\kappa\kappa}$ describes the stochastic of the observations with $\sigma_{\kappa i}$ being the variance of the i-th curvature value. A least-square adjustment based on the Gauß-Markov model can be finally used to derive the object's deformed shape, represented by the estimated displacements $\hat{w}$:

$$\hat{w} = \overbrace{(A^T \cdot \Sigma^{-1}_{\kappa\kappa} \cdot A)}^{\boldsymbol{N}}{}^{-1} \cdot A^T \cdot \Sigma^{-1}_{\kappa\kappa} \cdot \kappa \tag{2.9}$$

The absolute position and orientation of the object is however unknown. The normal equation matrix N has therefore a rank deficiency of 2 and cannot be inverted without further information. For linear structures in structural and geotechnical engineering, this problem is commonly solved using either the cantilever beam approximation, where the starting point and its orientation is assumed to be fixed, or the simply beam support approximation, where the displacement at either end of the object is constant.

This definition can be seen in analogy to the geodetic datum within a geodetic network. Geodetic observations between network points can provide relative information with high repeatability, but absolute benchmarks remain unknown. Free network adjustments are usually set up with constraints, where their minimum number is equal to the rank deficiency of the normal equation matrix (cf. Niemeier 2008). A special case of the geodetic datum in free network adjustment is represented by the so-called zero-variance base, which exactly fixes the number of point coordinates that are required to solve the rank deficiency analogous to the cantilever or simply beam support (cf. Section 4.3.1). Using more support-

ing points than required provides an estimation with redundancy, which allows an assessment of the correctness of the functional and stochastical model (cf. Section 6.2).

Geodetic adjustment methods may be therefore beneficial to overcome limitations in the integration process. At this point, different sensing technologies can be combined to support the approximations with metrological observations, i.e. displacement readings w^{ref} at specific points j arbitrarily distributed along the structure. These are taken into account by extending the functional model with observations. The equation system is, thus, expanded by additional lines, where i represents the sensor position along the object.

$$\begin{bmatrix} \kappa_1 \\ \vdots \\ \kappa_n \\ w_j^{ref} \\ \vdots \end{bmatrix} = \begin{bmatrix} \frac{1}{h^2} & \frac{-2}{h^2} & \frac{1}{h^2} & 0 & \cdots & \cdots & \cdots & 0 \\ \vdots & \ddots & \ddots & \ddots & \ddots & \ddots & \ddots & \vdots \\ 0 & \cdots & \cdots & \cdots & \cdots & \frac{1}{h^2} & \frac{-2}{h^2} & \frac{1}{h^2} \\ a_0 & a_1 & \cdots & \cdots & \cdots & \cdots & a_n & a_{n+1} \\ \vdots & \vdots & \vdots & \vdots & \vdots & \vdots & \vdots & \vdots \end{bmatrix} \cdot \begin{bmatrix} w_0 \\ w_1 \\ \vdots \\ w_{n+1} \end{bmatrix} \tag{2.10}$$

$$\Sigma_{\kappa\kappa} = \begin{bmatrix} \sigma^2_{\kappa_1} & \cdots & 0 & 0 & \cdots \\ \vdots & \ddots & \vdots & \vdots & \ddots \\ 0 & \cdots & \sigma^2_{\kappa_n} & 0 & \cdots \\ 0 & \cdots & 0 & \sigma^2_{w_1} & \cdots \\ 0 & \cdots & 0 & 0 & \ddots \end{bmatrix} \tag{2.11}$$

$$a_i = \begin{cases} 1 & i = j \\ 0 & i \neq j \end{cases} \tag{2.12}$$

The number of supporting points is basically variable, but must be at least 2 to solve the boundary value problem for 2D shape sensing along linear structures. Using more than two provides an estimation with redundancy, which enables an assessment of the

correctness of the functional and the stochastical model as well as the handling of potential erroneous data in practical applications.

For the sake of completeness, it must be noted that continuative concepts for three-dimensional shape sensing based on differential equations are used in medical science (Pauer 2017) as well as the in automotive and aerospace industry (Froggatt et al. 2011). These mainly utilize FBG sensors and DFOS to determine the shape of tubular-like structures, which can either be realized by integrating at least three individual strain sensing layers along the object (Moore and Rogge 2012), by applying special multicore fibers (Zhao et al. 2016) or by using one single fiber in helical winding (Pauer and Ledermann 2020). In civil engineering, three-dimensional sensor arrangements are known in literature, especially for curvature sensing along pipelines (Inaudi and Glišić 2010; Klais et al. 2017) or bending monitoring of rock bolts (Forbes et al. 2017), but are beyond the scope of this cumulative thesis.

Other numerical integration methods are based on the Newton–Cotes quadrature and commonly used for point-wise strain sensor setups, where the number of sensing locations is limited along the structure. Sigurdardottir (2015) discusses the trapezoidal and rectangle rule integration for beam-like structures, analyzes the error terms of the double integration process and presents validation results for cantilever as well as simply supported beams for different load cases. Geotechnical studies introduce the utilization of Newton-Cotes formulas for lateral displacement monitoring along slope inclinometers (Sun et al. 2016; Zheng et al. 2019). The integration methods are basically independent of the load case (Sigurdardottir 2015), but require exact boundary conditions.

The data analysis of the presented applications in this thesis is based on differential equations, which enable a more flexible definition of supporting points along the structure. The author however emphasizes that numerical integration methods based on the Newton–Cotes quadrature might supply higher reliability for well-defined setups, especially when using point-wise strain sensors in

cantilever manner (cf. Zheng et al. 2020).

2.4 CURVATURE PROGRESS AND SPATIAL RESOLUTION IMPACT

The error in the numerical integration process does not only depend on the reliability of the curvature determination itself, but also on the curvature progress (i.e. the shape of the curvature curve), the number of sensors (Vurpillot et al. 1998) and the sensor spacing (Sigurdardottir 2015). In other words, an appropriate acquisition of the curvature distribution along the structure with an adequate spatial resolution is essential for the derivation procedure. To point out limitations of different spatial capabilities, Figure 2.2 presents a graphical analysis of three different point-loading scenarios of a beam structure. Discrete, point-wise strain measurements as well as distributed strain profiles with different spatial resolutions Δz (cf. Section 3.3) are compared to theoretical models.

The curvature distribution resulting from point-wise, short-gauge strain sensors (Figure 2.2, middle) strongly depends on the number of sensing points as well as their location along the structure. The loading scenario can be sufficiently depicted, if the sensing point design is adequately fitted to the load case, cf. 7-point-setup in Figure 2.2b. Other setups as exemplarily shown in Figure 2.2c may provide distorted signals, from which the load case is interpreted incorrectly. Beside this fact, it must be noted that short-gauge sensors only represent the strain behavior at local points, which may be sufficient for short-range applications along objects with homogeneous material parameters like steel (cf. Brunner and Wieser 2006). Material discontinuities along the structure however essentially affect the locally measured strain values, especially inside concrete as discussed further in Chapter 6. Long-gauge strain sensors, typically with sensitive lengths of up to 10 m (Smartec 2018), can overcome this limitation for curvature monitoring (Glišić and Inaudi 2007), but also restrict the spatial capabilities for shape sensing.

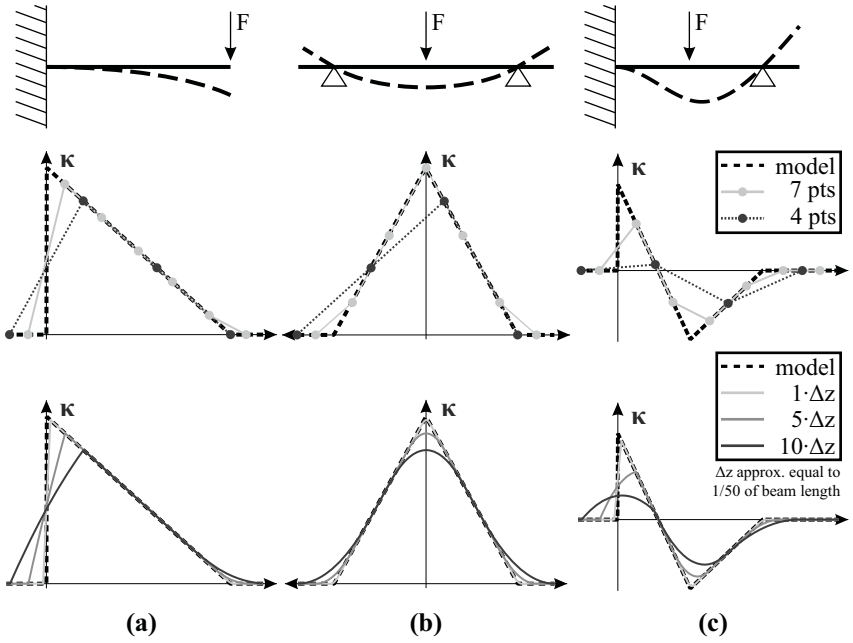

Figure 2.2: Analysis of spatial resolution impact on curvature determination (based on Monsberger and Lienhart 2021b) with theoretical model (top), pointwise sensing (middle) and distributed sensing (bottom): **(a)** Cantilever - single load (linear distribution). **(b)** Simply supported - single load (bi-linear distribution). **(c)** Cantilever in combination with floating bearing.

Distributed sensing (i.e. DFOS) basically enables both, the comprehensive, gapless acquisition of the strain behavior and the localization of local defects. The distributed profiles (Figure 2.2, bottom) present smoothing effects and increasing deviations to the theoretical distribution with decreasing spatial resolution. This particularly becomes visible at abrupt changes in the curvature profiles, which are observable for cantilever setups at the fixed bearing location. The principal loading scenarios can however be captured in all curves despite spatial limitations.

2.5 CONCLUSIONS

This chapter leads to the conclusion that 1D strain sensors are capable to obtain 2D or even multidimensional shape information even though sensing is originally carried out in longitudinal direction of the object. The strain sensing elements must be however appropriately arranged along the structure to ensure a reliable determination of the curvature value at the observed location. The boundary value problem of the double integration process can be either solved by common approximations (cantilever or simply beam support) or by involving additional metrological observations. This further allows an assessment of the model correctness as well as handling of potential erroneous data in practical applications.

The derived curvature distribution itself strongly depends on the curvature progress and the spacing of the sensitive elements. DFOS can provide continuous, gapless information along the entire structure and therefore, enable an adequate, distributed acquisition of the curvature shape with high spatial resolution. Other DFOS characteristics like measurement repeatability, sensing range or installation methods might be however insufficient compared to conventional point-wise sensors for specific shape sensing applications.

The following chapters discuss the utilization of distributed fiber optic sensing techniques, with corresponding benefits as well as limitations. Their suitability for strain-based shape sensing along civil infrastructure is analyzed based on laboratory tests as well as various practical applications.

3

Distributed Fiber Optic Sensing

Disclaimer

This chapter is based on the publications listed below. Figures, texts and contents are therefore already partly or fully published.

C. M. Monsberger et al. (2016). "Deformation measurement of a driven pile using distributed fibre-optic sensing." *Journal of Applied Geodesy* 10(1): 61–69

F. Buchmayer et al. (2021). "Advantages of tunnel monitoring using distributed fibre optic sensing." *Journal of Applied Geodesy* 15(1): 1–12

C. M. Monsberger and W. Lienhart (2021b). "Distributed Fiber Optic Shape Sensing of Concrete Structures." *Sensors* 21(18): 6098

C. M. Monsberger et al. (2022). "Large-scale distributed fiber optic sensing network for short and long-term integrity monitoring of tunnel linings." *Journal of Civil Structural Health Monitoring*

3.1 INTRODUCTION

Fiber optic strain sensors have already been used over the past decades in several scientific fields (Glišić 2022). Figure 3.1 shows commonly utilized sensor types in civil engineering, which can be divided into (i) point-wise sensors, (ii) quasi-distributed sensors (i.e. discrete number of point-wise sensors in-line) and (iii) fully-distributed sensors.

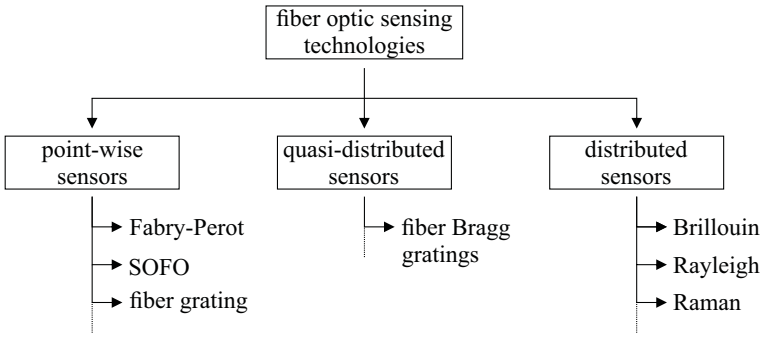

Figure 3.1: Classification of fiber optic sensing technologies.

The first category ranges from Extrinsic Fabry-Perot Interferometry (EFPI) to fiber gratings, i.e. the long period grating (LPG) and the fiber Bragg grating (FBG). The most prominent point-wise representative, however, might be the SOFO (fr. Surveillance d'Ouvrages par Fibre Optique, engl. structural monitoring with fiber optic) sensor based on the Michelson and Mach-Zehnder Interferometry (Inaudi 1997; Inaudi and Vurpillot 1999), which enables strain monitoring with gauge lengths from 0.25 to 20 m. Disregarding the optical measurement principle, its setup can be compared to conventional electrical strain gauges with only one sensitive element in-line. This finally led to complex SHM networks with more than 100 individual point-wise sensors (Inaudi et al. 1999).

Quasi-distributed and distributed fiber optic sensors have therefore become significantly more popular in structural and geotechnical applications as they can provide distributed measurements profiles with high resolution from the inside of the structure. For this, however, the fiber optic interrogation unit, the sensing cables, or the FBG sensors respectively, and the installation technique must be appropriately adjusted to ensure the monitoring results' quality.

This chapter discusses the sensing principle of various sensing technologies and reviews different setups of FBG sensors and DFOS cables. Sensor calibration results and investigations on the spatial resolution impact of DFOS are presented to point out general capabilities for civil infrastructure monitoring.

3.2 QUASI-DISTRIBUTED SENSORS

FBGs are part of the so-called quasi-distributed sensor category, where only one or several discrete sensing elements can be placed along one optical fiber. The sensing principle is based on a physical modification through a periodic change (Λ) of the refractive index (n_G) of the glass fiber core mode at specific locations, so-called FBG sensors (Othonos and Kalli 1999).

When a broadband light spectrum is coupled into the sensing fiber, light with the corresponding Bragg wavelength ($\lambda_G = 2{\cdot}n_G{\cdot}\Lambda$) is reflected back to the FBG interrogation unit (cf. Figure 3.2a). The wavelength of the reflected signal (λ_G) changes with varying strain ε and temperature ΔT at the discrete location of the grating, which can be determined from the wavelength change $\Delta\lambda$ by

$$\frac{\Delta\lambda_{\varepsilon,\Delta T}}{\lambda_G} = C_{\varepsilon}^{FBG}\varepsilon + C_T^{FBG}\Delta T \tag{3.1}$$

using the linear strain (C_{ε}^{FBG}) and temperature (C_T^{FBG}) sensitivity coefficients. Other parts of the optical spectrum propagate forward along the fiber path and are sensitive to other FBGs with different wavelengths. The wavelength changes of the individual gratings

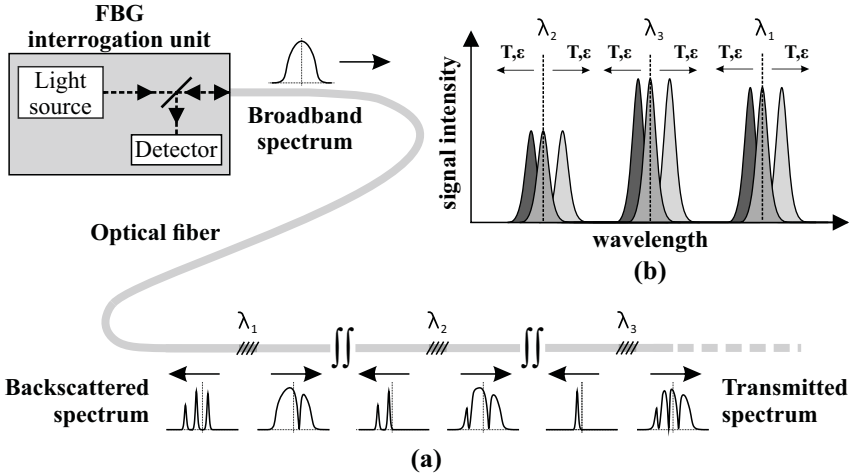

Figure 3.2: Sensing principle of quasi-distributed FBG sensors (based on Othonos and Kalli 1999): **(a)** Sensing setup. **(b)** Resulting wavelength spectrum.

recorded at the interrogation unit can be either negative (dark gray) or positive (light gray) as shown in Figure 3.2b, corresponding to the physical behavior at the FBG location.

A single FBG sensing chain may include tens of sensors depending on the applications with respect to the expected strain and temperature range along the object. Although the distributed sensing feature can only be partially fulfilled and gaps in-between the sensing points can not be captured, this significantly reduces the number of required sensing cables and measurement channels compared to conventional point sensors. FBG sensing systems can provide high frequency measurements with a sampling interval of up to 5 kHz and a high repeatability, usually <0.6 µm/m at 1 Hz (Luna 2021). Their quasi-distributed sensing feature is specially beneficial for structures with high frequent loading, where the location of interest is exactly known before the installation, see e.g. Woschitz et al. (2015). Other applications might utilize DFOS sys-

tems instead to localize the exact sensing position and, finally, to enable an overall deformation assessment of the structure.

Contrary to distributed fiber optic sensors, which typically utilize standard telecommunication fibers for sensing purposes, FBGs represent deliberate modifications along the optical fiber. These must be applied to the glass fiber core at selected locations in advance to the sensor installation. The gratings can be either written with ultra violet (UV) light during the production process of the fiber at the draw tower (so-called draw tower gratings, DTGs) or a posteriori after production. The latter one enables longer exposure times resulting in higher reflectivity of the gratings and, therefore, longer sensing ranges. DTGs are however advantageous regarding robustness, since the fiber coating must not be removed after production and thus, the maximum strain range is not substantially reduced by the grating.

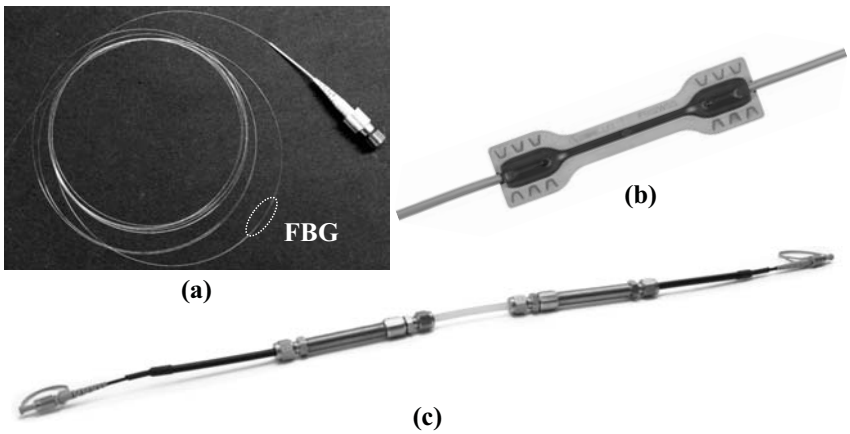

Figure 3.3: FBG sensors for civil infrastructure monitoring: (**a**) Bare fiber. (**b**) HBM K-FS62WSS (HBM 2021).(**c**) Sylex SC-01 (Sylex 2021).

Numerous FBG strain transducers with different designs and setups are commercially available. These range from bare fiber sensors for surface or embodiment applications (Figure 3.3a) to prepacked

sensors, which can be, for instance, directly welded to steel surface objects (Figure 3.3b) or stretched between anchoring points (Figure 3.3c). Pre-fabricated FBG sensors often provide an additional FBG for temperature sensing, which is encapsulated from strain and can be used for temperature compensation of the strain measurements in practical applications.

3.3 FULLY-DISTRIBUTED SENSORS

Fully-distributed fiber optic sensing utilizes the natural scattering of optical signals during the forward propagation along the optical fiber as schematically shown in Figure 3.4. Small parts of these intensity losses are backscattering effects, whose spectral characteristics carry information about geometrical, physical or chemical quantities. Backscattering basically arises at all locations of the optical fiber and therefore, information can be retrieved along the entire sensing line with a certain spatial resolution Δz depending on the sensitivity of the interrogation unit.

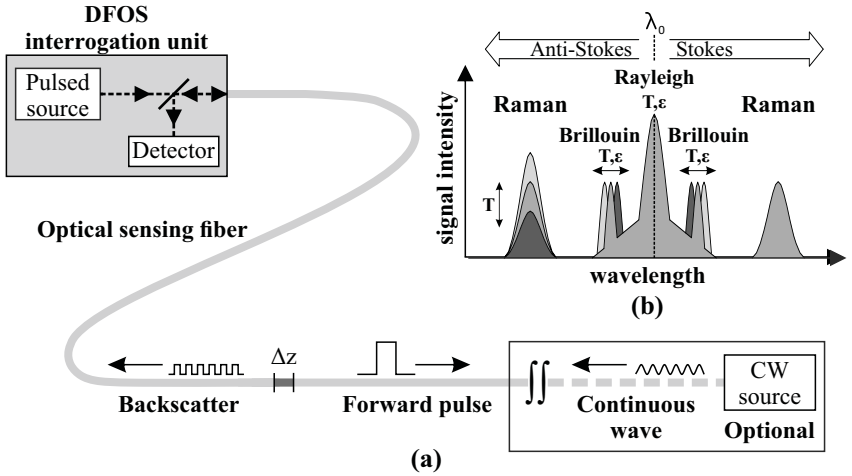

Figure 3.4: Distributed fiber optic sensing techniques (Monsberger et al. 2020): **(a)** Sensing setup. **(b)** Different scattering components in optical glass fibers.

Table 3.1: Characteristics of different distributed fiber optic static strain sensing systems obtained from corresponding product datasheets (Omnisens 2016; Neubrex 2018; OZ 2018; Luna 2019; fibrisTerre 2020; Febus 2021; Sensuron 2021) and laboratory tests (e.g. Buchmayer et al. 2021).

Scattering	***Rayleigh***		***Brillouin***	
Sensing technique	OFDR	TW COTDR	BOTDA/ BOFDA	BOTDR/ BOFDR
Configuration	Single ended		Loop	Single ended
Commercial manufacturers	Luna, Sensuron	Neubrex	fibrisTerre, Omnisens, Febus, OZ Optics, Neubrex	
Sensing range	≤70 m (2 km)	20 km	≤80 km	≤100 km
Spatial resolution	≤10 mm	2–20 cm	≥20 cm	≥100 cm
Typ. strain repeatability	≤1 µm/m	≤0.5 µm/m	≥2 µm/m	≥20 µm/m
Typ. sensing duration	<10 s	≤10 min	3–60 min	

The backscattered spectrum can be split into linear (Rayleigh) and non-linear (Brillouin and Raman) scattering, see Figure 3.4b. Raman systems are mainly sensitive to temperature, whereas Rayleigh and Brillouin instruments are sensitive to both, strain and temperature changes. Their capabilities regarding spatial resolution, repeatability and measurement duration are however significantly different as listed in Table 3.1. It is noted that the listing is limited to static strain sensing techniques and dynamic interrogation units or DAS (distributed acoustic sensing) systems are not addressed. The indicated specifications are general values and vary depending on the manufacturer, the sensing parameters or the sensing cable. The appropriate selection of the DFOS technology therefore always involves a trade-off between sensing range, spatial

resolution or strain repeatability and must be suitably adjusted with respect to the monitoring requirements.

The following sections present data processing techniques for Rayleigh and Brillouin spectrums and their correlation to strain and temperature information along the sensing line. This basic introduction shall provide general knowledge about the DFOS capabilities for civil infrastructure monitoring. Reference is given to Hartog (2017) for more detailed information on different DFOS techniques.

3.3.1 Rayleigh-based Sensing Systems

Rayleigh scattering is one of the major effects of intensity loss in optical fibers. It is mainly caused by variations of the refractive index profile along the fiber core and effects about 85% of the natural attenuations (Wuilpart 2011). In general, the Rayleigh scatter amplitude has a random but static behavior along the fiber. External influences, like changes in strain or temperature, cause a spectral shift in the locally reflected Rayleigh pattern. Therefore, a small, local segment of the fiber, which is transformed to the frequency domain, can be interpreted as a weak reflecting fiber Bragg grating with a random period. The modeling of the distributed measurement system may be realized by splitting the fiber in equidistant segments and calibrating the local Rayleigh shift in reference to changes in strain or temperature.

Rayleigh strain sensing systems are typically known for distributed sensing with high resolution, i.e. high spatial resolution and measurement repeatability, but with limitations in the sensing range (cf. Table 3.1). The Rayleigh setups further described in this thesis were interrogated by an optical backscatter reflectometer (OBR) from Luna Innovations Inc. (Luna 2019). Its sensing principle is based on the optical frequency domain reflectometry (OFDR) technique, where the Rayleigh backscatter amplitudes and phases are recorded in the frequency domain. The signal as a function of the fiber length (equivalent to the classical optical time domain

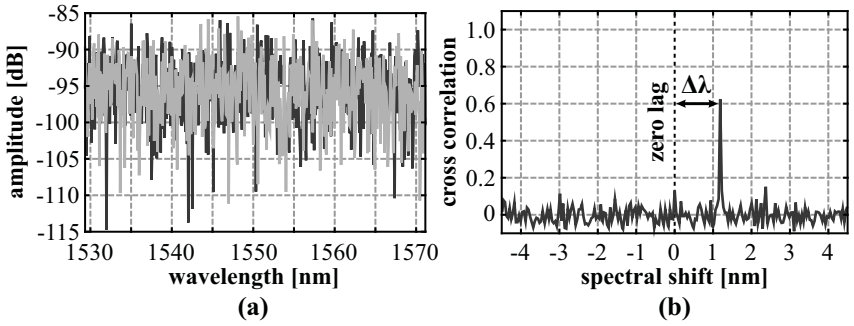

Figure 3.5: OFDR sensing technique (Monsberger et al. 2016): **(a)** Wavelength spectrum for an unstrained (black) and a strained (gray) fiber segment (Δz = 10 mm). **(b)** Corresponding cross correlation function.

reflectometry, OTDR) can be obtained through a Fourier transformation. For details on the optical network and the measurement principle see Soller et al. (2005) or Kreger et al. (2006).

The distributed sensing system is set up by recording the Rayleigh backscatter along the sensing fiber in a known strain and temperature state. This initial measurement can be interpreted as a reference scan of the optical network. Later, the fiber is scanned again, when the strain and/or the temperature state has changed. The signal of both measurements can now be divided into equidistant segments, where the segment length Δz corresponds to the spatial resolution of the OBR, and observed in the frequency domain (Figure 3.5a). Variations in the strain and temperature behavior cause a spectral shift between the spectrums of both scans, whose size is directly proportional to changes in strain and temperature and can be determined by a cross-correlation between both spectrums (Figure 3.5b). The distributed approach is finally realized by determining the shift for each segment along the sensing network.

The transfer from the derived wavelength shift $\Delta\lambda$ [nm], or the frequency shift $\Delta\nu$ [GHz] respectively, to strain ε and/or tempera-

ture change ΔT can be approximated by the linear function

$$\frac{\Delta\lambda}{\lambda} = -\frac{\Delta\nu}{\nu} = C_\varepsilon^R \varepsilon + C_T^R \Delta T \tag{3.2}$$

with the sensitivity coefficients C_ε^R and C_T^R and the center wavelength λ or center frequency ν of the scan. This relation is basically identical to the FBG response (cf. Equation 3.1).

3.3.2 Brillouin-based Sensing Systems

The Brillouin scattering effect in single-mode optical fibers occurs when light is reflected by the refractive index modulations produced by acoustic waves (Horiguchi et al. 1989). The velocity of the acoustic wave depends on the temperature and the density of the medium, i.e. of the optical fiber. The relation between these physical quantities and the Brillouin scattering effect can be used for distributed sensing.

Brillouin systems are generally known in civil infrastructure monitoring for sensing over long distances, which however results in spatial limitations and typically, longer measurement times of several minutes (cf. Table 3.1). The technology can be classified into two types: Analyzer systems use a closed loop setup as schematically shown in Figure 3.4. The signal of the pump laser is stimulated by a continuous wave from the other fiber end, so-called stimulated Brillouin scattering. Sensing is either performed in the time domain (Brillouin Optical Time Domain Analyzer, BOTDA) or in the frequency domain (Brillouin Optical Frequency Domain Analyzer, BOFDA). In practical applications, the loop configuration is often realized by a strain (and temperature) sensing forward path and a return path, which is stress-free and sensitive to temperature only. Hence, the pump laser and the continuous wave laser are typically located within the same enclosure for commercially available interrogation units.

If the sensing loop is interrupted at any location and the sens-

ing fiber is impaired by mechanical impacts or similar, Brillouin Optical Time Domain Reflectometry (BOTDR) or Brillouin Optical Frequency Domain Reflectometry (BOFDR) can be carried out alternatively. This so-called spontaneous Brillouin scattering effect utilizes single-ended configuration without stimulation, even though with significant degradation in both, the signal to noise ratio as well as the spatial resolution.

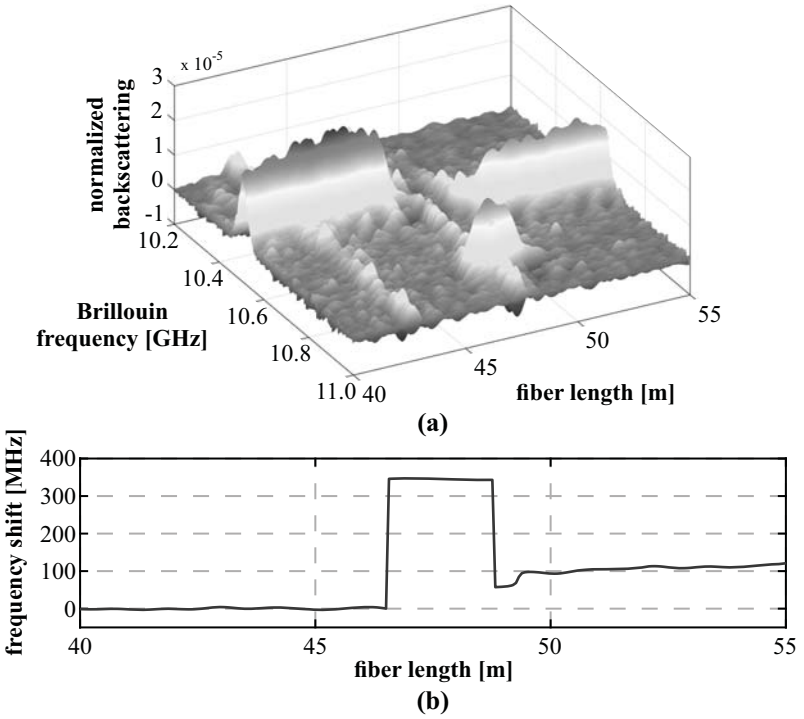

Figure 3.6: Brillouin sensing result (Monsberger et al. 2022): **(a)** Frequency spectrum acquired for one specific measurement epoch. **(b)** Derived frequency shift profile along the sensing fiber relative to Brillouin baseline frequency.

The typical backscattering result delivers the Brillouin frequency spectrum (Figure 3.6a). This optical fiber under test depicts a Bril-

louin baseline frequency of about 10.4 GHz, but is affected by strain and/or temperature starting at a position of about 47 m, resulting in a significant Brillouin frequency increase at this location. Using fitting techniques, e.g. the Lorentzian function (Nöther 2010), the intrinsic Brillouin frequency ν at each position along the optical network can be determined.

The further analysis of the Brillouin frequency shift $\Delta\nu$ can be either performed with respect to a corresponding reference measurement or relative to the Brillouin baseline frequency (as shown in Figure 3.6b). Contrary to OFDR strain sensing methods, where relative changes between measurements can be evaluated only, Brillouin sensing therefore allows an analysis of the absolute strain if the fiber's baseline frequency is appropriately known. Variations of $\Delta\nu$ depend on the longitudinal strain ε and/or temperature changes ΔT. The sensor characteristic can be expressed by

$$\frac{\Delta\nu}{\nu} = C_{\varepsilon}^{B}\varepsilon + C_{T}^{B}\Delta T \tag{3.3}$$

where C_{ε}^{B} and C_{T}^{B} are the linear Brillouin sensitivity coefficients.

3.4 SENSING CABLES FOR CIVIL ENGINEERING APPLICATIONS

Sensing along or inside civil infrastructure implies harsh environment for sensors. Therefore, an appropriate protection of the sensitive element combined with a reliable stress transfer from the structure to the sensor is essential to realize successful monitoring approaches. Optical fibers are generally advantageous for sensing as they are lightweight, flexible and can be easily attached to the structure. The glass material itself is however fragile and might be more susceptible to potential damages, which is why the sensing fibers must be protected using additional protection layers depending on the civil engineering application.

Commercial manufacturers offer a wide range of DFOS cables

with different setups, well designed for specific applications in different fields – to name a few: Corning Inc. (USA), Neubrex Co. Ltd. (Japan), Nanjing Hecho Technology Co. Ltd. (China), Smartec SA or Solifos AG (both Switzerland). Figure 3.7a–d depicts a selection of strain sensing cables from the latter named supplier, especially developed for sensing in structural and geotechnical engineering. The cables protect the optical sensing fiber through a metal tube (Fiber in Metal Tube, FiMT), a polyamide sheath or even a special steel armoring to ensure the sensor's integrity during installation and monitoring. All cable layers are interlocking for a reliable transfer of mechanical strains to the sensitive glass fiber core. The outer sheath of the cables can be structured, which may be beneficial for enveloping materials like grout or concrete to guarantee a solid bond. Further information on the cable designs may be gathered from the datasheets, see e.g. Solifos (2019a) and Solifos (2019b).

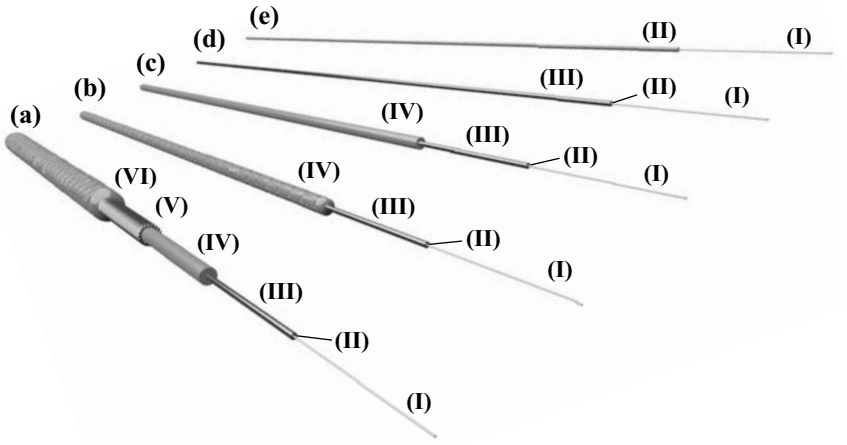

Figure 3.7: Distributed fiber optic strain sensing cables for civil engineering applications with (I) sensing single mode fiber (⌀ 250 µm), (II) tight buffer, (III) metal tube, (IV) polyamide protection layer, (V) special steel armoring and (VI) polyamide outer sheath (Monsberger and Lienhart 2021b): **(a)** BRUsens V3 (⌀ 7.2 mm). **(b)** BRUsens V9 (⌀ 3.2 mm). **(c)** BRUsens V4 (⌀ 3.2 mm). **(d)** BRUsens FiMT (⌀ 0.9 mm). **(e)** Tight-buffered fiber (⌀ 0.9 mm).

DFOS cables with protection layers might not be flexible enough for surface applications or gluing in grooves, especially in case of a tight cable routing. Tight buffered (TB) fibers (Figure 3.7e), normally used in telecommunication industries (see e.g. TLC 2020), can overcome this restriction, but are limited in harsh environment due to their fragility.

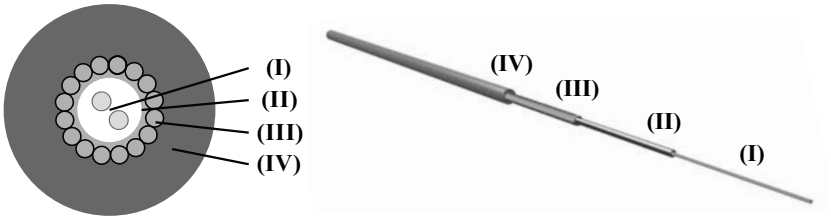

Figure 3.8: Temperature sensing cable BRUsens Temp (⌀ 3.4 to 4.8 mm) with (I) single mode sensing fiber (⌀ 250 µm), (II) loose metal tube, (III) special steel armoring and (IV) polyamide sheath.

As discussed in Section 3.3, external temperature changes do not only result in thermal variations of the structure, but also alter the fiber optic strain readings. Monitoring along civil infrastructure therefore always requires an appropriate compensation of arising temperature variations to ensure the strain sensing quality. An additional sensing fiber, which is not influenced by mechanically induced strain, shall be therefore installed next to the strain sensing cable in practical applications.

The setup can be either realized by a temperature fiber installed embedded within the same cable structure (Smartec 2017) or loosely installed within a separate cable nearby (Solifos 2019c). The latter one, shown in Figure 3.8, contains one or more temperature sensing fibers (I), which are embedded into gel inside a metal tube (II). The tube has, however, a larger diameter compared to strain sensing cables from Solifos to ensure that no strain (up to a certain amount) is transferred to the fiber and, hence, it is sensitive to temperature

only. At the outside, a steel armoring (III) as well as a polyamide outer sheath (IV) protects the fiber against mechanical impacts.

Strain-based shape sensing basically requires two or more sensor layers appropriately arranged along the structure. Special multi-core optical fibers (MCF) contain various sensing cores within the same optical fiber and can supply 3D curvature values in the cross section of the fiber itself (Zhao et al. 2016). Nevertheless, the fiber structure usually has only a diameter of 125 µm (Fibercore 2021) and thus, the curvature sensitivity is limited due to the minimal distance between the fiber core, especially for long-wave bending.

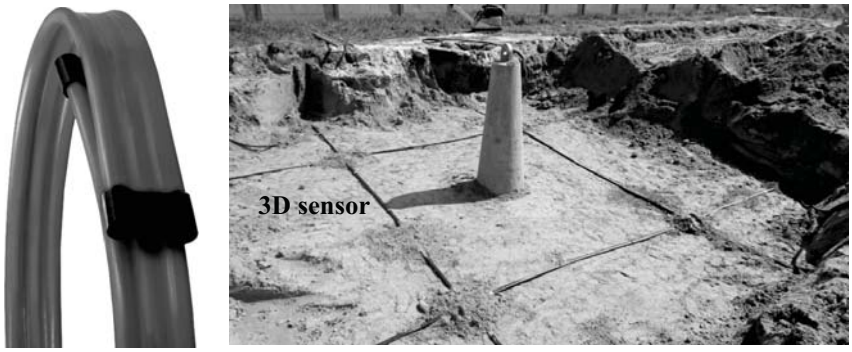

Figure 3.9: Composite 3D shape sensor from SHM systems: **(a)** Practical realization (Bednarski et al. 2021). **(b)** Geotechnical installation for displacement monitoring around concrete foundations (Sieńko et al. 2021).

Latest developments provide a composite sensor with multiple optical fibers for 3D displacement sensing (SHM 2021). Its enveloping protection layer allows an embodiment into soil or concrete and makes it feasible for civil engineering applications. The rectangular shape of the sensor (Figure 3.9) also ensures the consistent orientation of the individual fiber layers along the structure, which is indispensable for shape sensing algorithms. The standard sensor has a dimension of 50 mm x 15 mm and consists of four individual fibers.

Even if the spatial separation of the sensors is significantly larger in comparison to MCF, the curvature sensitivity for small sensor spacing is limited when using Brillouin interrogation systems (cf. Section 4.2 and 4.3). The author emphasizes that this sensor can definitely offer a practical shape sensing solution for engineering structures, but is not further considered within this thesis.

3.5 LONGEVITY OF FIBER OPTIC SENSORS

Newly constructed civil infrastructure is often designed for service lifetimes of up to 150 years (Moritz et al. 2021). The longevity of the distributed fiber optic sensor inside or along the concrete structure is therefore essential since replacements after the installation entail large efforts or are even not possible. Nevertheless, any durability assessment of DFOS cables is challenging due to lacking knowledge on the long-term stability and missing standards.

Investigations on the optical fiber itself demonstrated that the failure probability is always related to the applied tensile stress as well as the bending radius. Installation lengths shorter than 1 km are designed to enable a success rate of about 99% for tensile stresses of up to 800 MPa (= approx. 1% of strain) over 25 years (Corning 2017). This timeframe might be significantly extended in case of lower mechanical strains. For instance, Corning Inc. underlines that there is no "theoretical lifetime" for optical fibers (Corning 2016).

The fiber's lifespan, however, not only depends on the mechanical properties, but also on external influencing factors, e.g. extreme temperatures or presence of hydrogen. The latter one may cause major attenuations along the fiber over time, which restrict the lifetime within long-term monitoring. Here, sensing cable layers (cf. Figure 3.7a–c) can provide a certain degree of protection for a wide range of applications, especially for transportation infrastructure like bridges or tunnels. For harsher environment, extensive aging tests by the French national radioactive waste management agency (ANDRA) showed that specially carbon-coated fibers are able to

withstand high hydrogen and even radiation exposure (Delepine-Lesoille et al. 2017).

Existing literature points out that no general guidelines on the long-term durability of fiber optic sensors can be provided. These must be appropriately selected within the monitoring design depending on the requirements on flexibility, mechanical protection and prevalent monitoring environment.

3.6 SENSOR CALIBRATION

Numerous manufacturers of FBGs and distributed fiber optic sensors do not specify individual calibration parameters, but refer to "typical" literature values without further information. The sensitivity coefficients C_ε and C_T usually vary depending on the composition of the optical fiber itself as well as the sensor packing. For instance, literature values for FBG sensors ranges from 0.61 to 0.79 for K_ε and $6.3 \cdot 10^{-6}/K$ to $8.2 \cdot 10^{-6}/K$ for K_T (Kashyap and López-Higuera 2002), equal to variations of 20% or even more. The knowledge of reliable calibration parameters is therefore crucial to avoid systematic errors essentially higher than the measurement repeatability of the interrogation unit itself (c.f. Section 3.2 and 3.3) and finally, to ensure accurate measurements.

This section exemplarily discusses strain and temperature calibration results of selected DFOS cables, which were utilized within the applications presented in this thesis. Reference is given to Klug and Woschitz (2015), Monsberger et al. (2016), Moser et al. (2016), Monsberger et al. (2017), and Buchmayer et al. (2021) for numerical results of FBG and DFOS calibrations conducted at the IGMS (Institute of Engineering Geodesy and Measurement Systems, Graz University of Technology) laboratory.

3.6.1 Strain Calibration

For calibrations and investigations of strain sensors, IGMS developed a unique testing facility (Presl 2009) for sensor lengths of up to 30 m without folding. As shown in Figure 3.10, its key components are the linear translation stage, which allows a maximum sensor elongation of 300 mm, the laser interferometer used for precise reference measurements and the tiltmeters at each sensor mounting point. The test device enables fully automatic calibrations of prepacked FBG strain transducers, DFOS sensing cables or even bare fibers. More detailed information can be found in Woschitz et al. (2015).

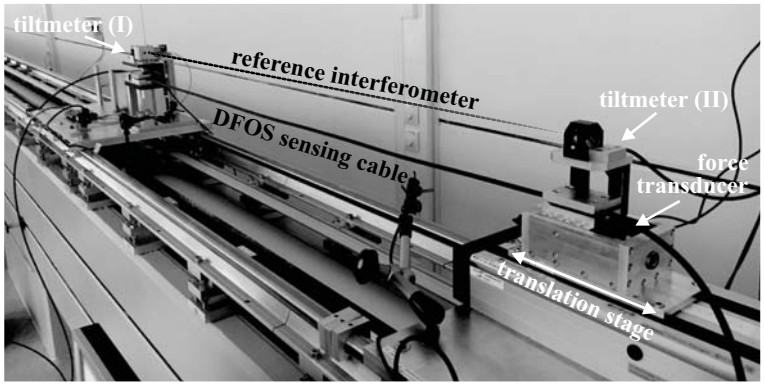

Figure 3.10: IGMS calibration facility for strain transducers (Monsberger and Lienhart 2017).

The raw measurement quantity of Rayleigh and Brillouin sensing $\Delta\nu$ usually depends on strain ε and temperature changes ΔT. Since the calibration facility is set up in the temperature-controlled IGMS laboratory(20°C $\pm$ 0.5°C), meteorology-dependent length changes during the testing period can be therefore excluded and the linear function can be expressed by

$$\frac{\Delta\nu}{\nu} = C_\varepsilon \varepsilon \Big|_{T=const.} \tag{3.4}$$

This relation is valid for all discussed fiber optic sensing techniques, but with variations in the sensitivity coefficients.

Calibrations are typically performed in loading cycles to analyze potential hysteresis effects as presented in Figure 3.11. This cable specimen with a length of approx. 2 m was tested in three full cycles up to 3500 µm/m and alternately interrogated by Brillouin and Rayleigh sensing units. The frequency shift values averaged over the testing length (Figure 3.11, top) depict a linear behavior at all loading steps, which permits an estimation of the strain sensitivity coefficient C_ε. The residuals between the linear fitting curve and the individual measurements (Figure 3.11, bottom) are within -15 µm/m and +10 µm/m, equal to a non-linearity of 0.5% or lower. The results also show a good agreement for loading and unloading with no essential hysteresis effect and similar shape for both technologies.

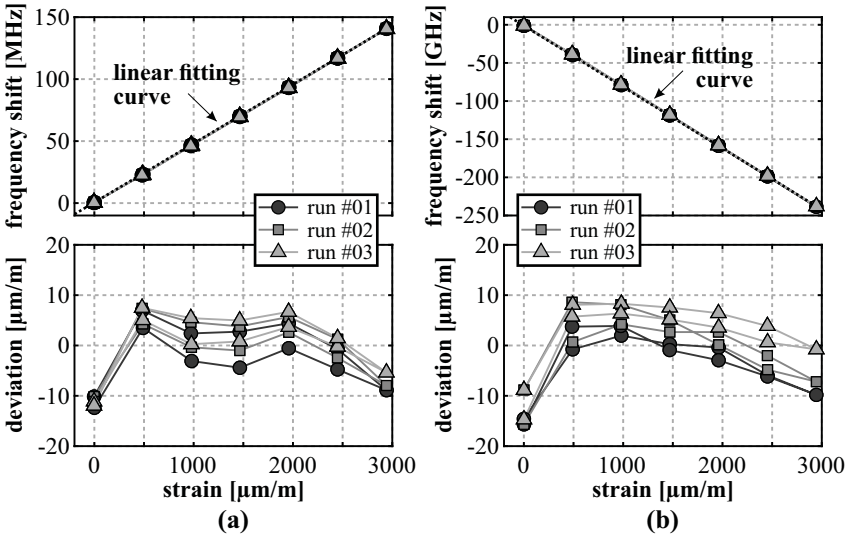

Figure 3.11: Strain calibration results of BRUsens V9 with linear fitting curve (top) and residuals to linear fitting curve (bottom): **(a)** BOFDA sensing unit. **(b)** OFDR sensing unit.

Even if the presented investigations highlight the excellent DFOS capabilities, the estimated sensitivity coefficients numerically differ in the range of some percent, not only to specifications, but also between different cable types or even cable patches of the same manufacturer (Monsberger et al. 2017; Buchmayer et al. 2021). The fiber optic strain sensing accuracy therefore not only depends on the measurement repeatability itself, but also on the reliability of the strain sensitivity coefficient, which must be well considered within data analysis.

3.6.2 Temperature Calibration

Reliable strain sensing requires an appropriate temperature compensation of the measured frequency shifts and therefore, also suitable temperature sensitivity coefficients of both, the strain as well as the temperature sensing cable. These can be evaluated by placing the DFOS cables inside a climate chamber as shown in Figure 3.12a. The loose installation without mechanical stress acting on the cable initiates that the linear relation is only temperature-dependent and can be written as

$$\frac{\Delta\nu}{\nu} = C_T \Delta T \Big|_{\varepsilon=const.} \tag{3.5}$$

In the presented calibration study, the cable behavior was investigated within temperature cycles between 0 and 60°C, where the absolute temperature was recorded by PT100 sensors to enable reliable reference values. Similar to the strain behavior, the results in Figure 3.12b depict a linear relation between the applied temperature and the measured frequency shift for all cables. The sensitivity, however, significantly varies depending on the cable type, where the BRUsens V9 is approximately twice as sensitive to temperature as the BRUsens V3 or the BRUsens Temp.

In general, the temperature dependency of the frequency shift can be considered as a combination of the optical bare fiber temperature sensitivity and thermal expansion of the surrounding layers

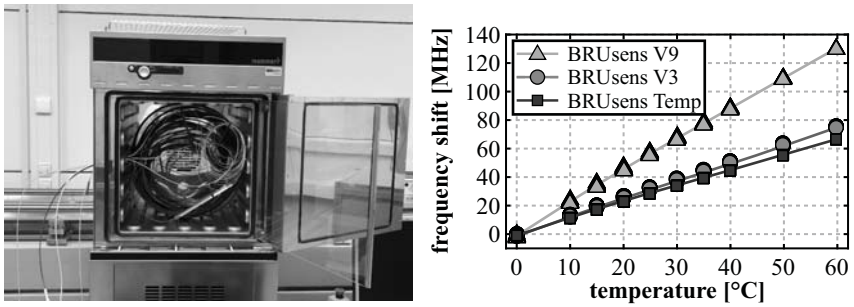

Figure 3.12: Temperature calibration (Buchmayer et al. 2021): **(a)** Climate chamber. **(b)** BOFDA calibration results of different sensing cables.

(Kurashima et al. 1990). Different enveloping layers and their connection to each other therefore affect the temperature coefficients. This can produce systematic errors in the temperature determination and finally, in the compensation of the strain values, if the sensitivity is not known appropriately and standard values are used.

3.7 SPATIAL RESOLUTION AND ALLOCATION

Using point-wise or quasi-distributed sensing techniques, the sensor positions can be well related to specific locations along the object, where the measurement values are captured with a defined gauge length. DFOS allows the distributed and continuous assessment of the structure's overall behavior without any gaps. Nevertheless, the resulting strain profiles represent an integrative response within the spatial resolution of the DFOS system and local stress events, e.g. due to structural damages or abrupt changes of the bending moment, might get smoothed. The system's capabilities with respect to the spatial resolution must therefore be well considered, especially for shape sensing approaches, where an appropriate relation between different sensing layers is essential to provide accurate curvature values (cf. Equation 2.3).

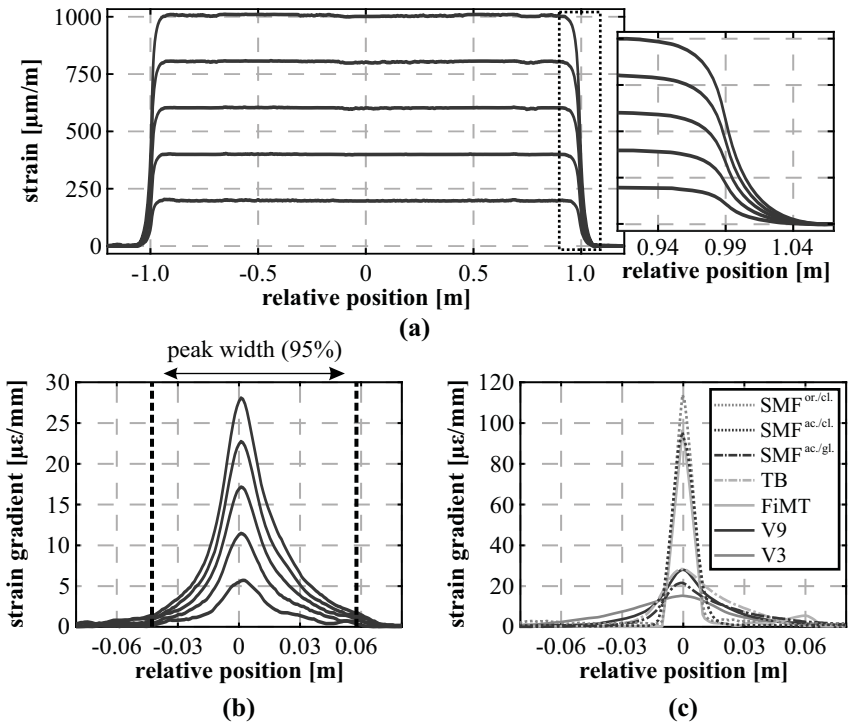

Figure 3.13: Analysis of spatial resolution impact (Monsberger and Lienhart 2021b): **(a)** Distributed strain profiles along strained section of sensing cable BRUsens V9. **(b)** Strain gradient at different load levels. **(c)** Strain gradient for different cable types at 1000 $\mu\varepsilon$.

The spatial resolution of the DFOS signal varies depending not only on the characteristics of the interrogation unit (cf. Table 3.1) itself, but also on the used sensing cable setup. Various enveloping layers result in different strain transfers from the sensing cable's outside to the sensitive glass fiber core and thus, the spatial recording of abrupt strain changes along the fiber is affected. To analyze this impact for different sensing fibers and cables, numerous samples with lengths of ~2 m were investigated at different load levels at

the IGMS strain calibration facility and interrogated using the high-resolution OBR with a spatial resolution of 10 mm (Figure 3.13a).

The strain application theoretically causes a discontinuous function at the sample edges, which is smoothed depending on the fiber packing. The influencing area can be evaluated by e.g. determining the strain gradient along the edge section (Figure 3.13b), which delivers the differential strain change over length. Figure 3.13c depicts the strain gradient profiles for all investigated cable types at a load level 1000 µm/m (= µε), equal to the highest load level displayed in Figure 3.13b. As expected, bare single mode fibers (SMF) with standard acrylate (ac.) and ormocer (or.) coating present the most feasible response to the applied strain with a total impact length lower than 3 cm when clamped. It is remarkable that the fiber in metal tube (FiMT) shows comparable results, which indicates a reliable bond between the sensing fiber and the surrounding metal sheet. Sensing cables (V3 and V9) as well as the tight buffered (TB) fiber deliver much longer impact areas of up to 10 cm or even more.

Table 3.2: Derived spatial resolution impact lengths for different sensors and load levels.

Sensor type	**95% strain gradient peak width [cm]** at ~ 500 µε	at ~ 1000 µε	at ~ 1500 µε
SMF (Ormocer, clamp)[(1)]	—	2.0	—
SMF 28e (Acrylat, clamp)[(1)]	—	2.6	—
SMF 28e (Acrylat, glued)	11.2	11.3	12.0
Tight-buffered	8.5	8.1	8.3
BRUsens FiMT	1.8	1.9	1.9
BRUsens V9	10.2	10.0	10.3
BRUsens V3	15.4	15.5	15.6

[(1)] only analyzed at ~ 1000 µε

The resulting strain gradient peak may also be classified to find the numerical peak width at a specific significance level (here it is

95%, cf. Figure 3.13b). This finally enables the determination of comparable spatial resolution impact lengths for different samples at different load levels as shown in Table 3.2. It is notable that the strain level itself does not significantly influence the derived impact length, which seems to be almost independent from the applied load. Nevertheless, the attaching method majorly affect the strain response. Whereas the first SMF (SMF 28e, clamp) was clamped at both edges of the testing facility, another sample of the same fiber (SMF 28e, glued) was fixed using an appropriate adhesive. The reduced strain transfer, obviously resulting from the elastic behavior of the glue, causes major differences in the strain gradient behavior (see Figure 3.13c) as well as in the numerical peak width. Beside the interrogation unit's capabilities and cable structure itself, the characteristics of the attaching method must therefore be also well considered within the DFOS design and data interpretation.

3.8 CONCLUSIONS

The previous sections reviewed the characteristics of quasi and fully-distributed fiber optic sensors. It could be demonstrated that the technology can be beneficial for civil infrastructure monitoring. While capturing distributed information along the entire sensing cable or, at least, at numerous points along the structure, the achievable repeatability is still in the με-range using quasi-distributed FBG and short-range Rayleigh sensing and therefore, comparable to traditional strain gauges. This definitely enables new capabilities for strain-based shape sensing. Additionally, Brillouin sensors are capable to continuously monitor over very long distances, but with limitations in the spatial resolution and the strain repeatability. Resulting effects on the curvature and bending derivation are further discussed in this thesis by means of practical applications.

Analogous to conventional sensors, DFOS strain values can not be directly measured and appropriate transfer functions are required to convert the raw measurement quantity. The absolute

strain sensing accuracy, therefore, not only depends on the measurement repeatability of the interrogation unit itself, but also on the knowledge of reliable conversion coefficients. As shown in this chapter, individual sensor calibrations can be a valuable measure to avoid systematic errors and finally, to ensure the measurement quality.

Even if the distributed sensing feature enables the gapless acquisition of strain profiles along the entire cable, the resulting signal represents an integrative response and corresponding smoothing within the spatial capabilities of the DFOS system. Here, the impact length basically depends on the spatial resolution of the sensing unit, the cable structure as well as the attaching method. It must be taken into account that this limitation also affects the shape sensing performance, especially at abrupt curvature changes.

4

Application I: Grouted Anchors

Disclaimer and Acknowledgement

This chapter is based on the publications listed below. Figures, texts and contents are therefore already partly or fully published.

C. M. Monsberger and W. Lienhart (2019). "Design, Testing, and Realization of a Distributed Fiber Optic Monitoring System to Assess Bending Characteristics Along Grouted Anchors." *Journal of Lightwave Technology* 37(16): 4603–4609

C. M. Monsberger and W. Lienhart (2021b). "Distributed Fiber Optic Shape Sensing of Concrete Structures." *Sensors* 21(18): 6098

I would like to acknowledge Sebastian Hirschmüller (University of Applied Sciences Rosenheim, Germany) and the company Keller Grundbau GesmbH (Austria) for their efforts during the practical anchor installation.

4.1 MOTIVATION

Construction projects in civil engineering require not only solid, but also economic and efficient foundations. Slopes and construction pits are usually stabilized using grouted steel anchors combined with shotcrete layers at the surface. The design of these so-called "soil nailing systems" is based on mechanical equilibrium considerations of a rigid body motion. This implies that only tensile stresses are considered and accompanying forces (i.e. shear forces near the slip surface) are neglected due to the simple design model, which is why the conventional anchor dimensioning is often over-sized.

In general, their utilization is only temporary within the stabilization phase and the anchors have no more structural utility after completion of the construction. Using smaller anchor diameters or other materials instead of steel, e.g. bamboo (Lim and Yang 2007) or laminated veneer lumber (Hirschmüller et al. 2016), induce lower bending capabilities, which must be taken into account to design the optimal anchoring system. At this point, strain-based fiber optic shape sensing approaches may provide information on the distributed bending behavior along embedded anchors, which can not be captured using other sensing techniques (cf. Section 1.1). An adequate, reliable design is however required, not only to ensure the shape sensing quality, but also to protect the optical fiber during installation and monitoring in harsh environment on-site. Practical concepts for measuring shear stresses along embedded geotechnical objects therefore rarely exist in literature and mainly focus on applications in rock mechanics, see e.g. Forbes et al. (2017).

This chapter introduces the design and realization of a distributed fiber optic shape sensing approach to assess distributed curvature and bending characteristics along grouted soil anchors. The system design and its installation is discussed and results of comprehensive laboratory tests are presented, in which the system was verified using independent image-based and geodetic total station measurements at the surface as well as by comparisons to theo-

retical beam models. The field application suitability is proven by means of an autonomous monitoring campaign over several weeks.

4.2 DESIGN AND SENSOR INSTALLATION

The objective of the presented study is to design and implement a reliable approach, which can be utilized in harsh environment on-site. Robust sensing cables are therefore required to protect the optical fiber under field conditions. As already discussed in Section 3.4, Solifos AG (Switzerland) offers ready-to-use DFOS cables specially developed for monitoring in structural and geotechnical engineering. The designed system utilizes the BRUsens V9 (cf. Figure 3.7) for strain and the BRUsens Temp (cf. Figure 3.8) for temperature sensing along the grouted anchors. These cable types provide an effective trade-off between protection and flexibility, which practically relevant at the anchor's head and bottom point (cf. Figure 4.1a).

To derive reliable bending curves from DFOS measurements, individual sensing fibers in different layers along the object are required. The quality of the shape sensing methodology not only depends on the accuracy of the DFOS system, but also on the exact relative alignment of the individual fiber layers and the distance d between them. For that reason, the monitoring anchors are modified with high-precise, machine-made milling grooves (depth of 7 mm) along the top and bottom layer of the object, which ensure distance deviations in the sub-millimeter range. The design is optimized to determine vertical bending only. A layout with three strain sensing cables in an appropriate arrangement (e.g. 8, 12, 4 o'clock) would also enable the derivation of 3D bending curves, which is not the focus of this investigation.

As illustrated in Figure 4.1, the strain sensing cable may be directly glued into the grooves along both layers of the anchor using a two-component epoxy specially fabricated for metal adhesion (Innotec 2017). This ensures a constant distance between the layers and also an equidistant gap of both fibers to the neutral axis within

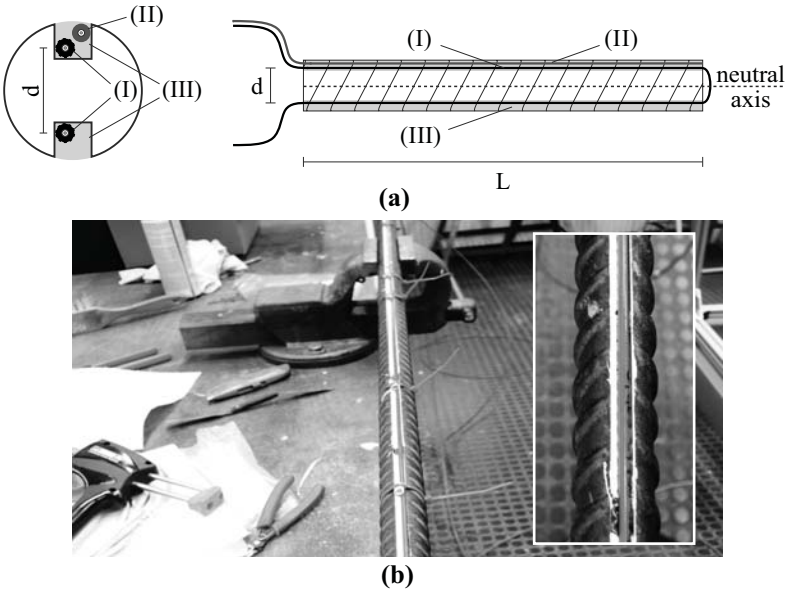

Figure 4.1: Steel anchor instrumentation concept (Monsberger et al. 2018a): (**a**) Scheme of sensing cable installation with (I) strain sensing cable, (II) temperature sensing cable and (III) gluing groove. (**b**) Practical realization.

the manufacturing accuracy of the groove. Temperature effects are expected to be analogous at both sides due to the short distance between the fiber layers. One temperature cable installed along the upper layer is therefore sufficient to provide a suitable temperature compensation of the measured strain profiles.

4.3 LABORATORY TESTING

To verify the reliability of the installation methodology, the DFOS system was installed along a real-scale anchor test specimen (length of 6.0 m, diameter of 30 mm) and investigated within different load scenarios at the IGMS laboratory, see Figure 4.2. As already mentioned in Section 3.6.1, the laboratory is fully air-conditioned and

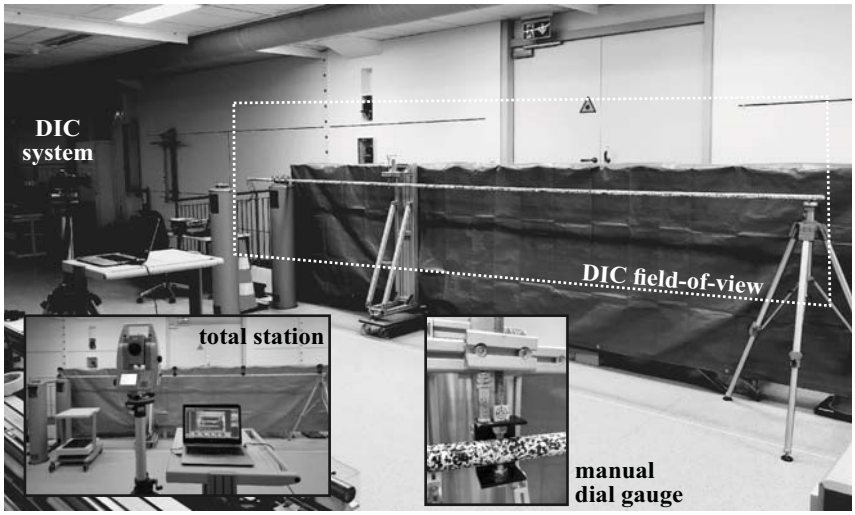

Figure 4.2: Laboratory test setup.

therefore, meteorology-dependent length changes during the testing period can be excluded.

4.3.1 Setup

The test specimen was one-ended fixed on a survey pillar for all setups to ensure that the starting point (i.e. bottom point of the anchor in practical application) as well as its orientation is fixed. Based on this common assumption in soil mechanics, the boundary value problem of the double integration can be solved model-free without other supporting points or knowledge about the further curvature and bending progress.

With respect to Equation 2.10, this procedure can be realized by eliminating the corresponding parameters (here: w_0 and w_1) from the functional model and the estimation:

$$\begin{bmatrix} \kappa_1 \\ \kappa_2 \\ \vdots \\ \kappa_n \end{bmatrix} = \begin{bmatrix} \frac{1}{h^2} & 0 & \cdots & \cdots & \cdots & \cdots & 0 \\ \frac{-2}{h^2} & \frac{1}{h^2} & 0 & \cdots & \cdots & \cdots & 0 \\ \frac{1}{h^2} & \frac{-2}{h^2} & \frac{1}{h^2} & 0 & \cdots & \cdots & 0 \\ \vdots & \ddots & \ddots & \ddots & \ddots & \ddots & \vdots \\ 0 & \cdots & \cdots & \cdots & \frac{1}{h^2} & \frac{-2}{h^2} & \frac{1}{h^2} \end{bmatrix} \cdot \begin{bmatrix} w_2 \\ w_3 \\ \vdots \\ w_{n+1} \end{bmatrix} \tag{4.1}$$

Loading was performed by a distance-based screw threads apparatus, where the deflection value at the respective loading point was recorded using a manual dial gauge with a resolution of 0.01 mm. Considering the manual readings, the achievable measurement precision of the applied loading is assumed to be in the range of some 1/100 mm. In addition, total station measurements to reflective tape targets and geodetic prisms were carried out to independently capture resulting displacements at specific locations. This procedure however does not allow the distributed verification of the derived displacement curves along the entire anchor.

Digital Image Correlation (DIC), a contactless image-based remote sensing technique, enables deformation monitoring of any kind of objects without the installation of sensors on the surface. The deformation computation and processing is carried out through a comparison of co-registered digital images of the object before and after the deformation event. A random speckle pattern was sprayed onto the surface of the anchor sample before the laboratory tests to provide a better contrast for the DIC principle. For data acquisition, a Nikon D5300 with a 11 mm lens was placed about 3.1 m from the mounted specimen, which ensures a pixel size of approximately 1 mm. The final sub-pixel resolution however depends on the quality of the image (e.g. contrast, background noise, etc.). Reference is given to Caporossi et al. (2018) and GOM (2018) for further information on the DIC methodology.

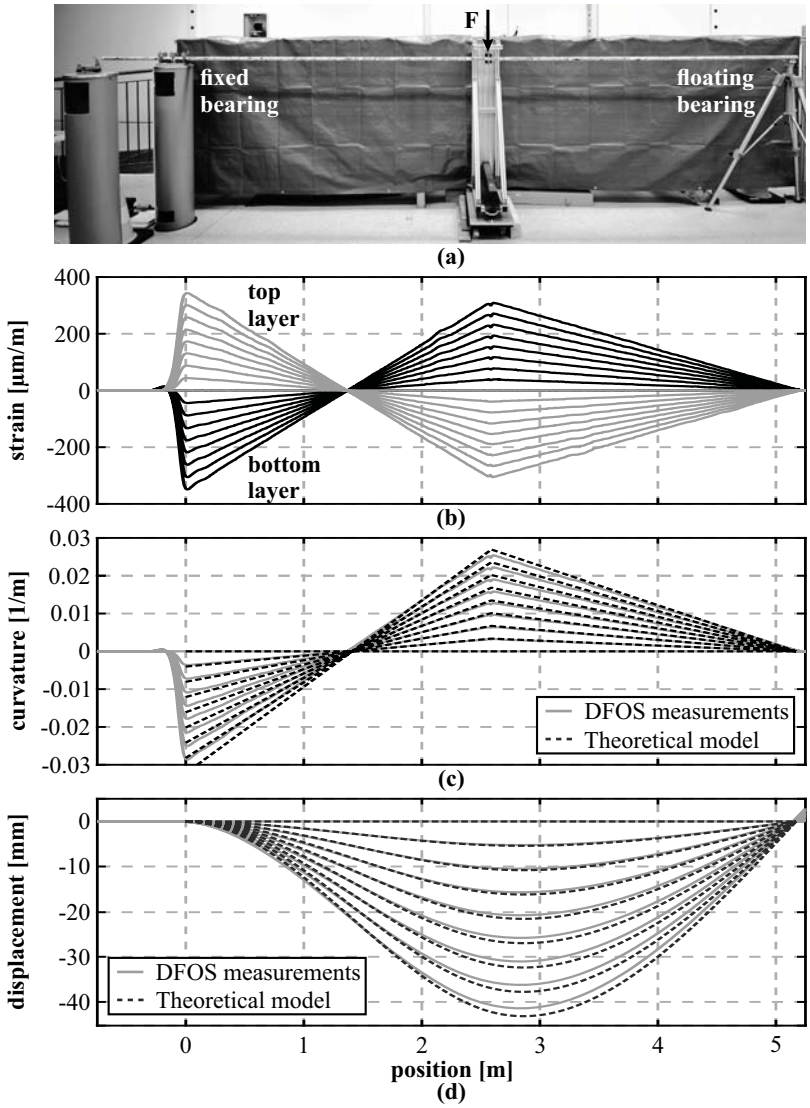

Figure 4.3: Laboratory load testing with one fixed and one floating bearing (Monsberger and Lienhart 2019): (**a**) Test setup overview. (**b**) Measured strain profiles along both layers. (**c**) Curvature values. (**d**) Displacement curves calculated from fiber optic strain values and derived from theoretical model.

4.3.2 Results

In a first test setup shown in Figure 4.3a, the one-ended fixed anchor specimen was supported by a floating bearing at the other side and loaded in the middle of the specimen in eight load steps of about 3 mm up to a maximum deflection of 42 mm. DFOS measurements were performed using the OBR, enabling a spatial resolution of 5 mm and a strain repeatability of 1 μm/m.

As a result of the equidistant arrangement of both fiber layers to the neutral axis, the non-filtered strain profiles in Figure 4.3b depict an almost perfectly mirrored behavior at each load step. This proves the exact alignment of the optical fiber in the vertical plane, which is highly relevant for the shape sensing quality. The strain increase is also linearly related to the applied load. The calculated curvature values (Figure 4.3c) as well as the derived bending curves resulting from the double integration of the curvature (Figure 4.3d) show a good agreement with the theoretical beam model derived from assumed material properties and the known loading scenario. Remaining deviations are mainly expected to result from uncertainties in the material properties (e.g. modulus of elasticity) of the specimen or even slight errors in the fiber arrangement. Systematic effects of the DFOS system itself can be excluded due to reliable calibrations as discussed in Section 3.6.

In order to provide statistical information on the capabilities of the designed shape sensing approach, fifty consecutive measurements were carried out at the same load step. Their respective deviations to the mean displacement curve in Figure 4.4a are within a range of ±0.02 mm and are also significantly lower than theoretical standard deviation, based on an uncertainty of 1 μm/m for the strain measurement and 0.5 mm for the distance between the sensing layers. These results lead to the conclusion that either the precision of the OBR strain measurements or the groove manufacturing, or even both, are too pessimistic, but are not further investigated at this point. The shape sensing repeatability can be

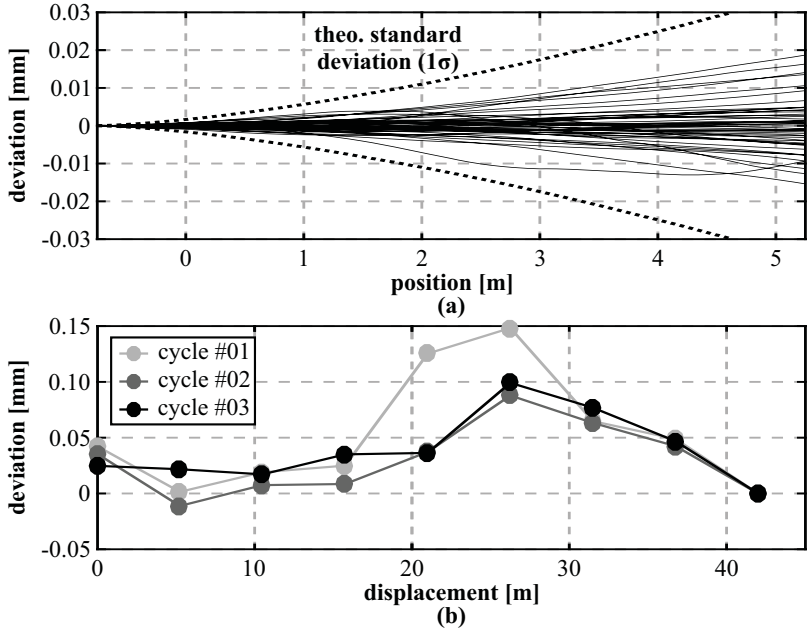

Figure 4.4: DFOS system analysis: (**a**) Deviations of 50 consecutive measurements from mean displacement curve at constant loading. (**b**) Deviations between loading and unloading derived at loading point F (Monsberger and Lienhart 2019).

analyzed in a more independent manner by comparing results of full loading cycles. Figure 4.4b displays the displacement differences between loading and unloading at each step of three conducted cycles, derived from the DFOS system at the loading point F. Numerical deviations are within a range between -0.01 and 0.15 mm, equivalent to a maximum non-linearity of the sensor of about 0.3%.

An absolute verification of the DFOS system's accuracy is possible through the independent image-based observations covering the entire specimen. The vertical displacement map resulting from corresponding DIC evaluations at the maximum loading step of 42 mm is shown in Figure 4.5a. The anchor's shape and its vertical bend-

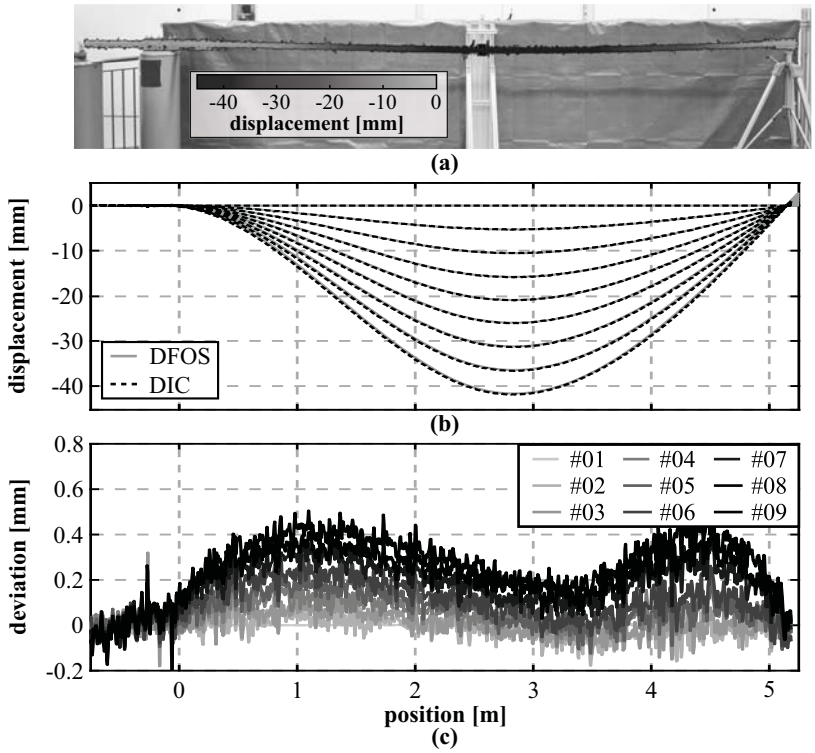

Figure 4.5: Comparison between DIC and DFOS measurements (Monsberger and Lienhart 2019): (**a**) DIC vertical displacement map at maximum load step. (**b**) Displacement curves derived from DIC and DFOS. (**c**) Deviations between sensing technologies (different curves correspond to different load steps).

ing can be clearly identified in the data and also the displacement magnitude is basically in the range of the values derived from the DFOS measurements. To compare the different sensing technologies, the profile along the neutral axis of the object is determined from the displacement map at each load step. The resulting DIC bending curves depict an excellent agreement to the DFOS system, see Figure 4.5b. Considering the differences between the derived technologies in Figure 4.5c, it can be seen that the maximum de-

viations are less than 0.5 mm, which is equivalent to an error of approximately 1%. Small remaining systematic effects, in particular drifts as well as periodic defects, are however still visible in the data. Linear deviations between the different technologies can be related to slight uncertainties in the camera setup and its calibration or even to small errors in the arrangement of the fiber layers. To eliminate these linear effects, the data of both technologies could be calibrated using the applied deflection at the loading point F or any other positions along the object, which is observed by an additional reference system (e.g. linear variable transducer or total station). Periodic effects in the range of about 0.2 mm might be a result of slight remaining errors in the camera calibration or effects of the DIC processing algorithm (Lava et al. 2009).

In addition to the high-resolution OBR measurements, the test specimen was also interrogated using Brillouin sensing techniques (BOTDA/BOTDR) at selected load steps to analyze their suitability despite the limited spatial resolution of 20 or 100 cm, respectively. The curvature profiles derived from the DFOS strain measurements (Figure 4.6a) point out these corresponding limitations. While the abrupt curvature change at the fixed bearing can be well depicted by the OBR data, the Brillouin techniques present smoothing effects, which increase with higher spatial resolution. This degradation coincides well with general assumptions (cf. Figure 2.2) and can also be theoretically modeled (Monsberger and Lienhart 2021b). The displacement curves, independently determined for each sensing technology, in Figure 4.6b show that the actual deformation behavior is displayed by all sensing technologies and the equidistant load increase is well represented. Nevertheless, the Brillouin sensing techniques display essentially higher systematic deviations to the DIC reference measurements, likely resulting from the lower spatial resolution and limited measurement precision. These discrepancies arise at locations with significant curvature changes, especially at the fixed bearing, and finally result in differences of more than 3 mm ($\simeq$ 7.5%) as shown in Figure 4.6c.

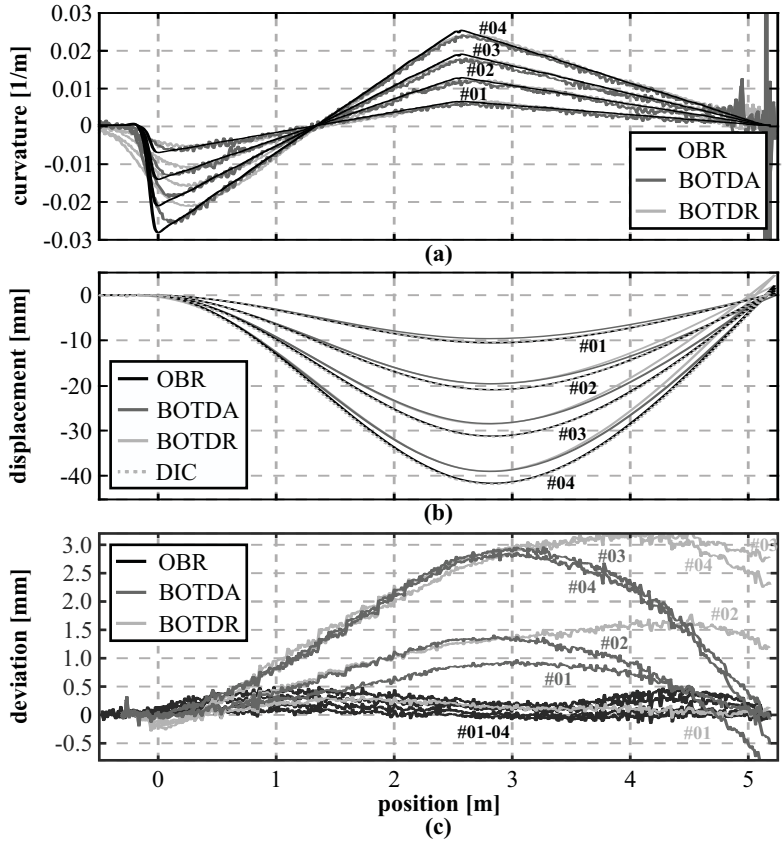

Figure 4.6: Comparison between different DFOS technologies (Monsberger and Lienhart 2021b): (**a**) Curvature profiles derived from DFOS strain measurements. (**b**) Displacement curves calculated from DFOS strains and DIC. (**c**) Deviations between DFOS and DIC.

Supporting elements in geotechnical applications are usually embedded into stable soil layers. This is why the bottom point is assumed to be stable, where the other end can deform due to arising loads. To realize these potential loading conditions in the laboratory, the instrumented specimen was set up as a cantilever beam in

a second test scenario. As illustrated in Figure 4.7a, an additional floating bearing was placed in the center to prevent sagging because of the tare weight of the sample. Testing was performed in one full cycle with equidistant steps of about 35 mm and a maximum deflection of 175 mm. The resulting OBR bending curves displayed in Figure 4.7b depict positive vertical deflections at the front part of the specimen, induced by the supporting bearing in the middle. Afterwards, negative displacements are observable due to vertical loading of the specimen and the derived deflections at loading point F can be linearly related to the uniform load increase. Remarkable is the fact that almost no differences are visible between the loading and unloading steps along the entire specimen, which also confirms the outcomes of Figure 4.4b.

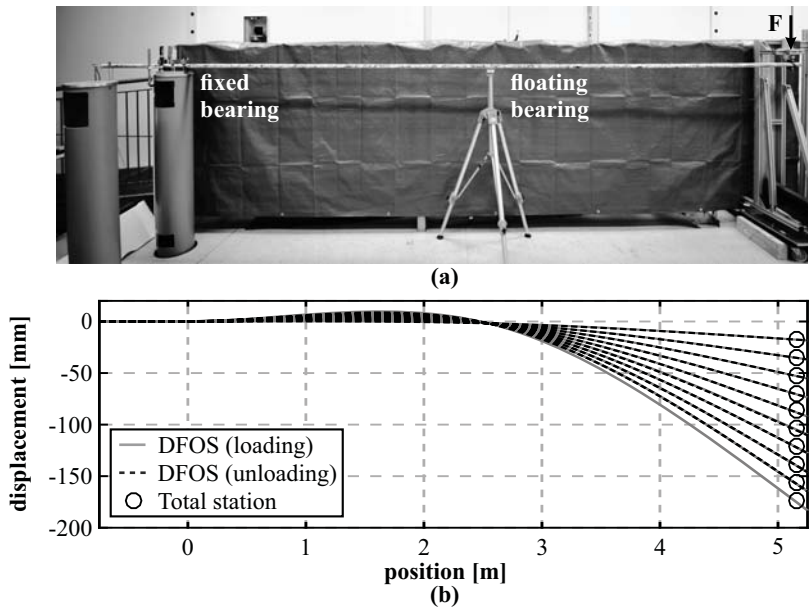

Figure 4.7: Laboratory load testing with cantilever beam setup (Monsberger and Lienhart 2019): (**a**) Test setup overview. (**b**) Displacement curves derived from DFOS and pointwise displacements from total station measurements.

The DFOS results are verified by geodetic total station measurements to a reflective tape target mounted at the loading point. Analogous to the comparisons using DIC, these absolute measurements of the vertical deflection coincide well with the derived DFOS displacements, where numerical deviations range from 0.3 to 1.2 mm, corresponding to a maximum error of less than 0.7%. It must however be emphasized again that potential systematic effects from both technologies could be further minimized by an individual calibration of the instrumented test sample.

4.4 FIELD APPLICATION

The designed DFOS system was utilized at a highway construction site to evaluate the feasibility for practical applications in a harsh field environment. This section discusses the anchor installation, fully integrated into the normal construction process on-site and presents selected results of the continuous monitoring campaign.

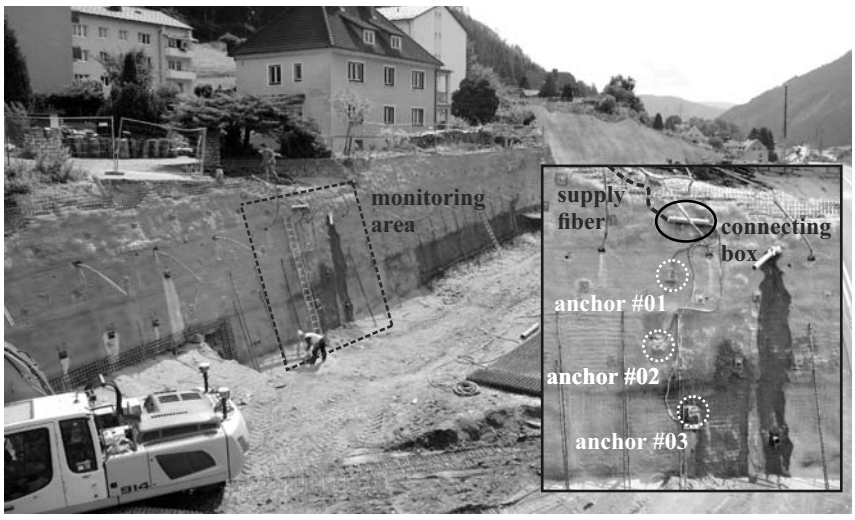

Figure 4.8: Construction site overview and monitoring area after excavation of level 03 (Monsberger et al. 2018b).

4.4.1 On-Site Installation and Monitoring Setup

Three monitoring anchors with a length of 5.0 m each were subsequently installed at different excavation levels of a slope stabilization. The excavation process itself was executed over several weeks, where the anchor monitoring of the corresponding level was started immediately after its installation. This enables an analysis of the vertical deformation progress over time resulting from the progressive further excavation of the construction pit. The final setup of the monitoring area after excavation of the last level is shown in Figure 4.8. Monsberger et al. (2018b) gives further information on the anchor installation procedure.

As a result of the laboratory test performance and the short total sensing range, measurements on-site were carried out only by the high-resolution OBR. The sensing unit was placed in a measurement container at the top of the slope, from which supply fibers were used to connect the device with the individual anchors. Autonomous, continuous monitoring was performed over several weeks with sampling frequency of 5 minutes to capture the anchors' bending characteristics while the slope construction pit was further excavated.

4.4.2 Results

The selection of field monitoring results presented in this thesis is focused on the shape sensing capabilities and corresponding visualizations. Detailed geotechnical studies of the data with comparisons to inclinometer measurements nearby and back-calculations are discussed in Hirschmüller (2019).

Figure 4.9a depicts the strain profiles measured along both fiber layers of anchor #01 at selected times over the entire monitoring campaign. The progressive utilization of the anchor's grout material can be observed starting from a depth of approx. 2.0 m due to the further excavation of the slope over time. Slight deviations between the sensing layers suggest bending of the anchor, where the point

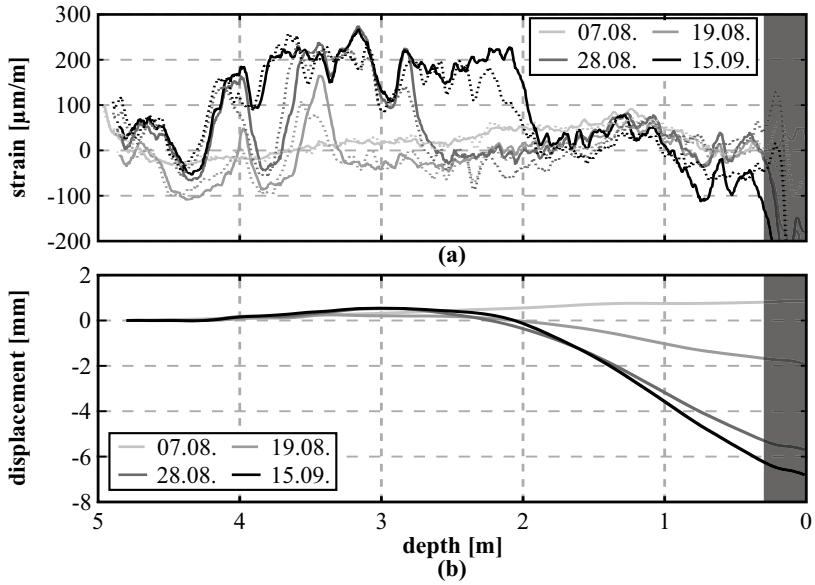

Figure 4.9: Field monitoring results along anchor #01: (**a**) Strain profiles along top (solid line) and bottom (dotted line) strain sensing fiber. (**b**) Derived displacement curves from DFOS measurements.

of curvature moves to the ground surface over time. It must also be considered that the displayed strain profiles represent a combination of soil deformations, temperature induced length changes of the steel anchor and impacts of concrete shrinkage, which is why compression strains are partially visible. Strain variations at the anchor head (gray areas in Figure 4.9) are most likely related to lacking grouting material in this area.

The displacement curves of anchor #01 derived from the fiber optic strain profiles are shown in Figure 4.9b. Progressive changes in the bending curves could be observed over time, which result in a maximum total displacement of about 6.8 mm at the surface point. The shape of the captured bending curves is similar to the laboratory test results of the cantilever beam setup with one supporting

bearing (Figure 4.7b). This suggests that the soil is stable from the bottom up to a depth of about 2 m and slight slipping arises in the area next to the surface. The shape of the derived bending curves in combination with the low magnitude of the derived deflections along the anchor however verifies the assumption that stresses perpendicular to the nail axis are negligible at this low service level for steel anchors with conventional dimensions.

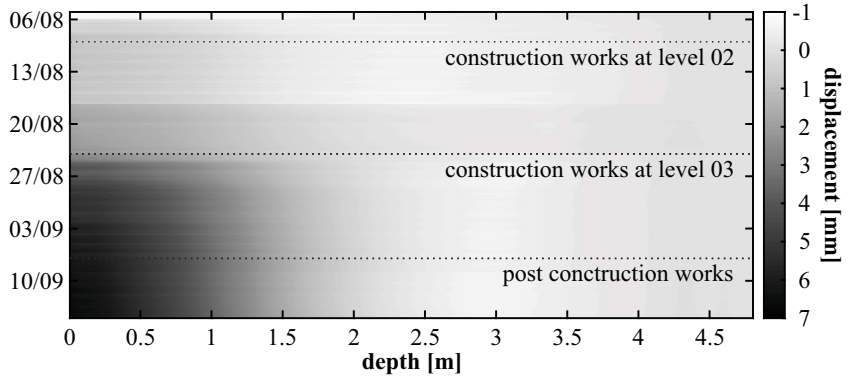

Figure 4.10: Progressive displacement changes along anchor #01 over entire monitoring period.

The continuous DFOS recording on-site with a sampling interval of 5 minutes also allows the progressive analysis of the displacement behavior along the entire anchor and its correlation to construction works as displayed in the colormap in Figure 4.10. Significant displacement changes only become visible in the timeline on August, 17th and 24th, which are assumed to be related to excavation works next or nearby the monitoring area. Except for these abrupt alterations, the bending behavior seems to be stable with variations lower than ±0.1 mm in depths greater than 2 m. Contrary, the slipping area next to the surface depicts a continuous further deformation progress of about 1 mm after the second excavation, which can be solidly captured by the designed sensing approach despite the low deformation magnitude.

4.5 CONCLUSIONS

The application presented in this section demonstrates the capabilities of distributed fiber optic shape sensing to monitor bending and curvature characteristics along grouted soil anchors. Appropriate installation techniques were designed and practically realized to ensure not only the integrity of the fiber optic sensors in harsh environment on-site, but also to guarantee the shape sensing quality.

The performance of the designed system was investigated in comprehensive laboratory tests of a real-scale specimen. The resulting DFOS bending curves correspond to theoretical beam models and also coincide well between loading and unloading of the specimen, where the deviations are typically smaller than 0.15 mm, equivalent to a sensor non-linearity of 0.3%. Verification measurements using a camera system based on DIC and pointwise total stations measurements show good agreement, even though slight remaining differences of up to 1% of the applied deflection become visible. These deviations can be related either to uncertainties in the test setup, the camera calibration or even to very tiny errors in the DFOS sensor arrangement. Linear effects could however be calibrated using the applied deflection pointwise observed at a single position along the object.

The laboratory setup was not only measured using the high-resolution OBR, but also interrogated by Brillouin techniques. The outcomes suggest that all sensing principles are capable to reproduce the deformation behavior based on the model-free shape sensing algorithm, but present limitations depending on the spatial resolution and measurement precision. The sensing technique must therefore be well selected with respect to requirements and the corresponding range of potential deviations must be taken into account within data interpretation, especially for longer sensing ranges.

Continuous monitoring of a slope stabilization at a highway construction site showed that the system is also feasible for practical applications in field environment on-site. Although the results de-

pict only small total displacements in the range of some millimeters, the progressive bending changes and similarities to the laboratory studies were solidly captured. In case of using minimized anchor diameters or other materials with lower shear strength capabilities, the DFOS approach could lead to a better understanding of the structural behavior and support the design of the optimal anchoring system.

5

Application II: Tunnel Linings

Disclaimer and Acknowledgement

This chapter is based on the publication listed below. Figures, texts and contents are therefore already partly or fully published.

C. M. Monsberger and W. Lienhart (2021a). "Distributed fiber optic shape sensing along shotcrete tunnel linings: Methodology, field applications, and monitoring results." *Journal of Civil Structural Health Monitoring* 11(2): 337–350

The practical applications presented in this chapter are the result of collaborative efforts of the tunnel owner, on-site engineers and research institutes. Representing all of those who contributed, I want to acknowledge the Austrian Federal Railway for the opportunity to realize different DFOS installations at the Semmering Base Tunnel project and the Institute of Rock Mechanics and Tunnelling at Graz University of Technology (namely Alexander Kluckner and Lukas Wagner) for numerous valuable discussions on the topic.

5.1 MOTIVATION

The design of excavation and supporting methods in modern tunneling is usually based on geotechnical monitoring and reliable data interpretation to enable an assessment of the structural integrity and finally, to guarantee a safe construction and operation. State-of-the-art monitoring approaches utilize displacement measurements of geodetic targets at the inner surface of the tunnel using total stations (Rabensteiner 1996; Schubert and Moritz, B. (eds) 2014; Schubert et al. 2002), which are however time consuming and always require a line of sight between the instrument and the measured object. Therefore, the measurements might interfere with the regular tunnel construction work, involve risks for the surveying team and can cause construction delays every time they are performed.

Electrical sensors, e.g. vibrating wire sensors (Rastogi 2008) or extensometers (Barla 2009), may be installed in addition to 3D monitoring targets inside the shotcrete lining to provide continuous in-situ measurements. The number of sensors inside the lining is limited due to practical reasons as each electrical sensor needs its own connecting cable to the data logger and hence, information can only be obtained at particular locations of the lining.

DFOS can be advantageous for in-situ tunnel monitoring since the distributed sensing feature delivers a complete picture of the linings' deformation behavior without blind spots. This can deliver hundreds or even thousands of measurement points inside the lining and significantly reduces the installation effort to gather strain values in the tunnel lining with a high spatial resolution compared to conventional sensors. Although the sensing cable installation procedure is critical due to the harsh tunnel environment, DFOS have already been successfully implemented inside shotcrete tunnel linings. These existing installations are mainly focused on investigations of mechanical stress as a result of creepage, shrinkage and/or rock pressure (Henzinger et al. 2018; Monsberger et al. 2018c; Wagner et al. 2020) as well as convergence analysis (De Battista et al.

2015; Kechavarzi et al. 2016), but do not deliver concepts for fully distributed shape analysis along the lining.

This chapter introduces a distributed fiber optic shape sensing concept, which utilizes DFOS strain measurements along different layers in combination with pointwise displacement readings for fully distributed shape assessment along curved structures, such as tunnels. The capabilities of the shape sensing algorithm are discussed by means of stochastic analysis. Different realizations along conventional tunnel cross-sections as well as shaft linings at a railway tunnel currently under construction also demonstrate the suitability for practical installations on-site.

5.2 SHAPE SENSING ALGORITHM FOR CURVED STRUCTURES

The practical applications presented in the previous chapters of this thesis assume that shape of the structure is initially linear. The shape sensing approach is however also applicable for curved structures like tunnel linings, if the initial curvature is appropriately considered within the sensing algorithm.

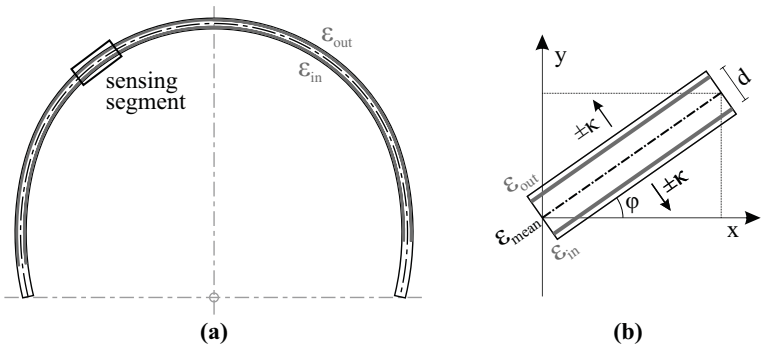

Figure 5.1: Shape sensing principle (Monsberger and Lienhart 2021a): **(a)** Schematic representation of cross-section profile. **(b)** Detail of one single sensing segment along the lining.

Similar to beam-like structures, two sensing cables may be installed parallel in circumferential direction, but with different distances to the center, see Figure 5.1a. This results in slightly different sensing segment lengths dx along the outer and inner layer, which can be taken into account by the installation radii of the different layers (Monsberger et al. 2019). The values resulting from applying the Euler-Bernoulli bending theory (cf. Equation 2.4) however only represent the curvature change due to shear stresses acting on the single sensing segment, i.e. stresses orthogonal to the tangent to the lining. Considering the curved initial geometry, the curvature impact within the two-dimensional coordinate system can be rewritten and expressed by

$$\begin{bmatrix} \kappa_i^x \\ \kappa_i^y \end{bmatrix} = \begin{bmatrix} \sin\varphi_i \\ \cos\varphi_i \end{bmatrix} \cdot \kappa_i \tag{5.1}$$

where φ is the orientation of the sensing segment relative to horizontal coordinate axis x (Figure 5.1b). This geometry parameter can be initially retrieved from the tunnel's planning model.

The numerical integration process is performed individually for each coordinate direction using finite difference methods. In contrast to the cantilever approximation, the boundary value problem can be solved by extending the functional model with additional observations, e.g. pointwise displacements of geodetic targets $\left(\Delta x^{TS},\ \Delta y^{TS}\right)$ recorded by total stations (TS) at th j-th position of the fiber optic installation along the lining:

$$\begin{bmatrix} \kappa_1^x \\ \vdots \\ \kappa_n^x \\ \Delta x_j^{TS} \\ \vdots \end{bmatrix} = \begin{bmatrix} \frac{1}{h^2} & \frac{-2}{h^2} & \frac{1}{h^2} & 0 & \cdots & \cdots & \cdots & 0 \\ \vdots & \ddots & \ddots & \ddots & \ddots & \ddots & \ddots & \vdots \\ 0 & \cdots & \cdots & \cdots & \cdots & \frac{1}{h^2} & \frac{-2}{h^2} & \frac{1}{h^2} \\ a_0 & a_1 & \cdots & \cdots & \cdots & \cdots & a_n & a_{n+1} \\ \vdots & \vdots & \vdots & \vdots & \vdots & \vdots & \vdots & \vdots \end{bmatrix} \cdot \begin{bmatrix} \Delta x_0 \\ \Delta x_1 \\ \vdots \\ \Delta x_{n+1} \end{bmatrix} \tag{5.2}$$

$$\begin{bmatrix} \kappa_1^y \\ \vdots \\ \kappa_n^y \\ \Delta y_j^{TS} \\ \vdots \end{bmatrix} = \begin{bmatrix} \frac{1}{h^2} & \frac{-2}{h^2} & \frac{1}{h^2} & 0 & \cdots & \cdots & \cdots & 0 \\ \vdots & \ddots & \ddots & \ddots & \ddots & \ddots & \ddots & \vdots \\ 0 & \cdots & \cdots & \cdots & \cdots & \frac{1}{h^2} & \frac{-2}{h^2} & \frac{1}{h^2} \\ a_0 & a_1 & \cdots & \cdots & \cdots & \cdots & a_n & a_{n+1} \\ \vdots & \vdots & \vdots & \vdots & \vdots & \vdots & \vdots & \vdots \end{bmatrix} \cdot \begin{bmatrix} \Delta y_0 \\ \Delta y_1 \\ \vdots \\ \Delta y_{n+1} \end{bmatrix} \tag{5.3}$$

$$\Sigma_{\kappa\kappa}^x = \begin{bmatrix} \sigma_{\kappa_1}^2 & \cdots & 0 & 0 & \cdots \\ \vdots & \ddots & \vdots & \vdots & \ddots \\ 0 & \cdots & \sigma_{\kappa_n}^2 & 0 & \cdots \\ 0 & \cdots & 0 & \sigma_{x_1}^2 & \cdots \\ 0 & \cdots & 0 & 0 & \ddots \end{bmatrix} \tag{5.4}$$

$$\Sigma_{\kappa\kappa}^y = \begin{bmatrix} \sigma_{\kappa_1}^2 & \cdots & 0 & 0 & \cdots \\ \vdots & \ddots & \vdots & \vdots & \ddots \\ 0 & \cdots & \sigma_{\kappa_n}^2 & 0 & \cdots \\ 0 & \cdots & 0 & \sigma_{y_1}^2 & \cdots \\ 0 & \cdots & 0 & 0 & \ddots \end{bmatrix} \tag{5.5}$$

$$a_i = \begin{cases} 1 & i = j \\ 0 & i \neq j \end{cases} \tag{5.6}$$

The number of geodetic points is basically variable, but must be at least 2 to solve the boundary value problem. Using more than two supporting points provides an estimation with redundancy, which enables an assessment of the correctness of the functional and the stochastical model.

The derived curvature values κ_i^x and κ_i^y are always related to the geometry of the lining. The workflow can hence be understood as an iterative approach, see Figure 5.2, where the lining's geometry (φ) is continuously updated. This evaluation procedure is performed as long as the total sum of squares (TSS) of the coordinate differences

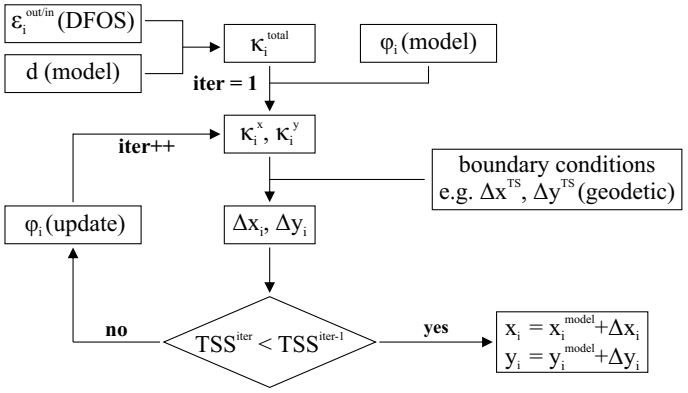

Figure 5.2: Basic determination workflow of the designed DFOS shape sensing approach (Monsberger and Lienhart 2021a).

between the current and the previous iteration is decreasing. The coordinates in both directions can be finally determined by adding the estimated differential supplements Δx_i and Δy_i to the initial model shape.

5.3 STOCHASTIC ANALYSIS

It is obvious that measurements from different sensing technologies are recorded with different stochastics. Appropriate weighting of the different observation types is therefore essential to guarantee the suitability of the estimation model.

Geodetic measurements in tunneling are usually performed with modern total stations with a distance measurement precision of 1 mm for prisms or 3 mm for bi-reflex targets and a standard deviation of 1" (= 0.3 mgon) for angle readings (Leica 2015). These specifications typically result in standard deviations between 1 and 5 mm for displacements in both coordinate directions depending on the target type as well as the measurement configuration.

The curvature values are represented by a combination of dif-

ferent measurement quantities, i.e. the measured DFOS strains ε, the distance between the fibers d and the orientation of the sensing segment φ (cf. Equation 2.4 and 5.1). Their standard deviation in both coordinate directions can be derived using corresponding variance propagation:

$$\sigma^2_{\kappa^x} = \left(\frac{\partial \kappa^x}{\partial \varepsilon}\right)^2 \cdot \sigma^2_\varepsilon + \left(\frac{\partial \kappa^x}{\partial d}\right)^2 \cdot \sigma^2_d + \left(\frac{\partial \kappa^x}{\partial \varphi}\right)^2 \cdot \sigma^2_\varphi \tag{5.7}$$

$$\sigma^2_{\kappa^y} = \left(\frac{\partial \kappa^y}{\partial \varepsilon}\right)^2 \cdot \sigma^2_\varepsilon + \left(\frac{\partial \kappa^y}{\partial d}\right)^2 \cdot \sigma^2_d + \left(\frac{\partial \kappa^y}{\partial \varphi}\right)^2 \cdot \sigma^2_\varphi \tag{5.8}$$

According to specifications of DFOS manufacturers, strain readings can be performed with a standard deviation between 1 and 20 µm/m (cf. Table 3.1). The distance between the fibers is basically determined by the planning model, which, however, does not exactly represent the actual installation in most cases due to practical reasons on-site. To analyze typical variations between model and realization, the positions of the DFOS cables at one selected construction site were captured by reflectorless total station measurements, see Figure 5.3a. The cable routes can be interpolated from the measured coordinates along both installation using cubic splines to continuously derive the DFOS cable spacing in circumferential direction. The resulting profile (Figure 5.3b) along the lining depicts deviations to the mean value of up to 10 cm. Although the mean value itself is basically in accordance with the planning model ($\overline{d}_{model} = 17$ cm), these variations with a standard deviation of 4.1 cm are an essential part of the combined curvature's measurement uncertainty.

Analogous to the cable spacing, the initial geometry of the lining is also retrieved from the planning model. Laser scans may be carried out after the shotcrete lining is constructed to investigate the excavation accuracy (Figure 5.3c). The orientation angles of the differential sensing segments in circumferential direction derived from

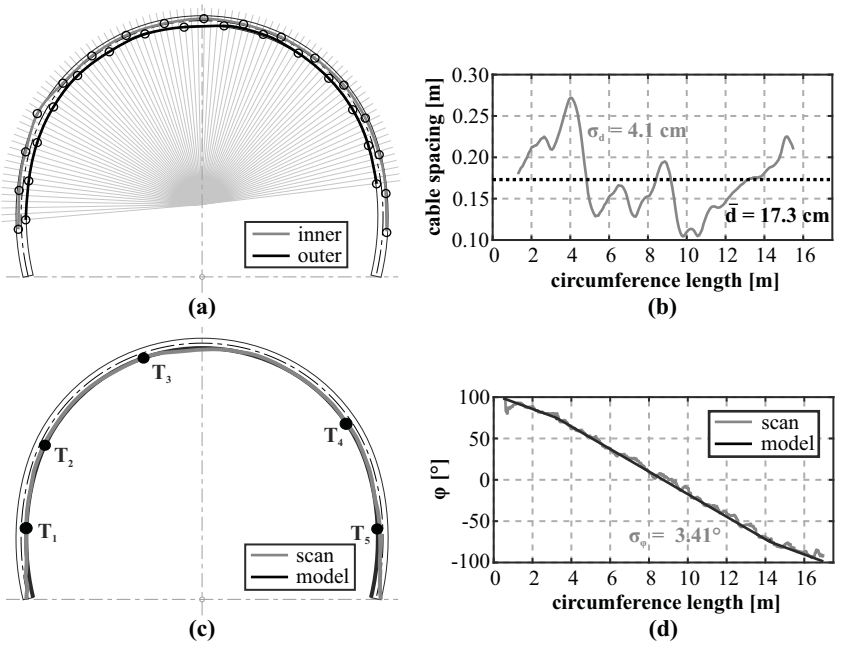

Figure 5.3: Stochastic analysis of constructed cross-section (Monsberger and Lienhart 2021a): **(a)** DFOS cables along inner and outer shotcrete layer from total station measurements. **(b)** Derived distance between installed sensing cable layers in circumferential direction. **(c)** Laser scan of excavation compared to planning model. **(d)** Orientation of single segments in circumferential direction derived from laser scan and planning model.

the model and the laser scan of the observed cross-section are shown in Figure 5.3d. This comparison delivers variations with a standard deviation of 3.41°, which should also be incorporated for thorough variance propagation.

The appropriate combination of all affecting measurement quantities enables a simulation of the achievable standard deviation of the resulting displacement profiles in x-direction (= lateral) and y-direction (= height) as shown in Figure 5.4. The analysis was done using different measurement uncertainties for the geodetic displace-

ment observations as well as different specifications for the DFOS strain readings according to manufacturer datasheets and empirical laboratory tests. The results show that the standard deviation basically increases from the tunnel crown (= 8.75 m) to the side walls. This seems logical since the integration process is less well-controlled at the outside due to the setup of supporting points (cf. locations of total station targets in Figure 5.3).

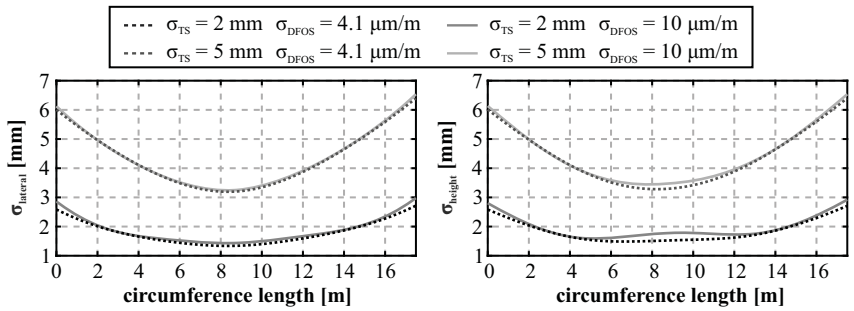

Figure 5.4: Standard deviation of resulting displacement profiles (Monsberger and Lienhart 2021a).

While the geodetic readings have major influence, different DFOS instrument capabilities depict only a small effect on the precision of the resulting displacement profiles. This is why strain profiles measured by Brillouin sensing units, typically with lower measurement precision, but significantly longer sensing range, may be also appropriate to determine capable displacement distributions. The standard deviation is similar for both coordinate directions with small deviations in the central area. It is obvious that particular orientations tend the curvature value to 0 (e.g. approx. 90° for κ_x). The curvature uncertainties of these positions have significantly lower influence on the estimation, which, therefore, provides a better result in lateral direction at the tunnel crown area.

5.4 FIELD APPLICATIONS AND MONITORING RESULTS

As part of the European TEN-T Network Corridor, the Semmering Base Tunnel (SBT) is one of the main railway infrastructure projects currently under construction in Europe. The original 150-year-old railway track crosses the mountain ridge with small curvature radii and large height gradients and, therefore, the train speed is low. The two tunnel tubes, with a total length of 27.3 km each, will be part of a high speed rail connection, which will reduce the traveling time between Austria's capital Vienna and the second largest city Graz by about 30% in the future. The optimized track routing through the tunnel additionally enables significantly better capabilities for rail goods traffic.

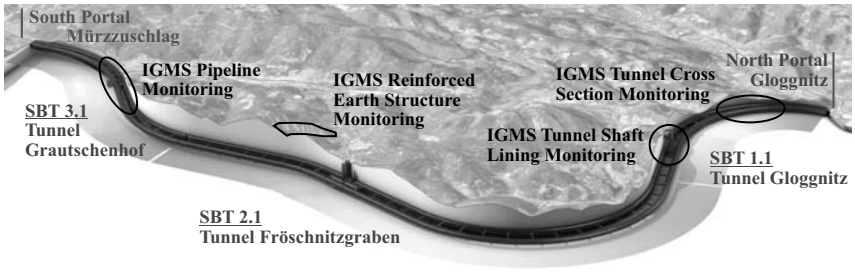

Figure 5.5: Semmering Base Tunnel (Monsberger and Lienhart 2021a): Project overview (based on Gobiet et al. 2017) and IGMS monitoring sites.

As discussed in Gobiet et al. (2017), the geological conditions along the tunnel track are challenging and most parts are being excavated by conventional tunneling based on the New Austrian Tunneling Method (NATM). This requires extended monitoring of the tunnel construction itself as well as of critical infrastructure nearby. DFOS monitoring systems were installed by IGMS at each construction lot (SBT 1.1 to SBT 3.1, cf. Figure 5.5 and Lienhart et al. 2019) to assess the structural integrity of individual construction parts and, finally, to increase the work safety on-site. These in-

stallations include monitoring of conventional tunnel cross-sections (Monsberger et al. 2018c; Wagner et al. 2020; Buchmayer et al. 2021) and shaft linings (Lienhart et al. 2019), reinforced earth structures (Moser et al. 2016) as well as pipelines (Klais et al. 2017).

5.4.1 Conventional Tunnel Cross-Sections

The outbreak in conventional tunneling based on the NATM is performed in different, well defined sequences, which enables the rock to support itself. Both instrumented cross-sections presented in this thesis were constructed in two steps: First, the upper part of the tunnel (so-called top-heading) was excavated and supported with two shotcrete layers. DFOS sensing cables were installed in different configurations along the supporting wire meshes of both layers. Their routing was retrieved by reflectorless total station measurements, which guarantees an exact spatial allocation of the cables within the cross-section for data analysis (Figure 5.6a). About five days later, the lower part (so-called invert) was removed and the lining ring was closed. Wagner et al. (2020) and Buchmayer et al. (2021) give detailed information on the DFOS design of the two monitoring cross-sections and the sensor installation inside the tunnel.

Rayleigh Sensing Results (Cross-Section 01)

DFOS monitoring was started immediately after the installation and was continuously performed over several weeks while the further tunnel excavation continued. The first instrumented cross-section was interrogated by a Rayleigh sensing unit, which can provide a spatial resolution of 3 cm over measurement ranges up to 2 km (Luna 2019). Figure 5.6b shows the strain profiles along both sensing cable layers about 5 days after the installation. These basically depict negative strains due to the interacting rock pressure as well as shrinkage and creepage effects of the applied shotcrete. Differ-

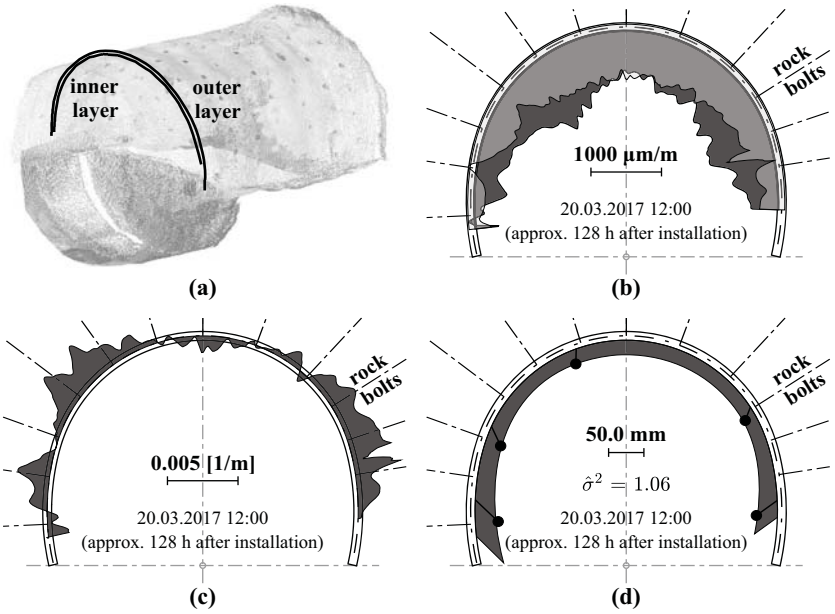

Figure 5.6: Distributed displacement sensing along the instrumented shotcrete tunnel cross-section (Monsberger and Lienhart 2021a): **(a)** Installation overview captured by laser scan. **(b)** Measured strain profiles along inner (dark gray) and outer (light gray) shotcrete layer. **(c)** Derived curvature values. **(d)** Displacement curves derived from DFOS profiles and pointwise geodetic measurements.

ences between the layers at the tunnel shoulders and the side walls indicate bending along the lining, which is confirmed by the derived curvature changes (Figure 5.6c). The observed behavior seems logical since the invert section was excavated and supported about five days after the installation of the top-heading. The entire top-heading section therefore moves downwards before the support and the lining is bent due to the resistance of the invert.

Distributed displacements along the cross-section can be determined by combining the DFOS curvature profiles with displacement readings of five geodetic targets using the algorithm presented in

Section 5.2. The derived displacement profile in Figure 5.6d depicts good agreement to the pointwise geodetic observation, even if this behavior is partly implied by the correlation within the sensing algorithm. The correctness of the functional as well as the stochastical model is however additionally confirmed by the estimation's redundancy, which delivers an a-posteriori variance factor $\hat{\sigma}^2$ of about 1.06.

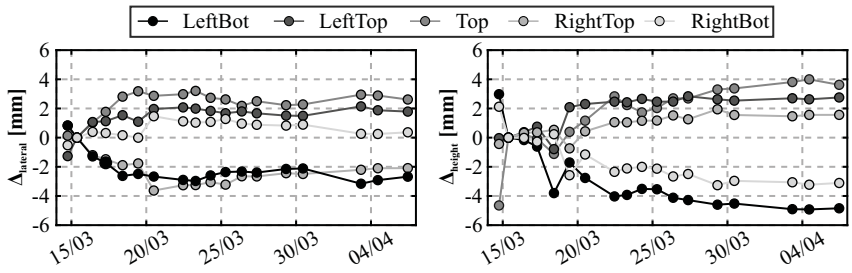

Figure 5.7: Coordinate residuals at supporting point locations over first 24 days of continuous monitoring (Monsberger and Lienhart 2021a).

The DFOS displacement profile can be estimated for each geodetic measurement epoch (usually once a day) in order to analyze typical deviations between the different sensing techniques over time. Figure 5.7 shows the coordinate residuals at the supporting point locations over the first 24 days of continuous monitoring. The first measurement of both sensing techniques exactly at the same time is only available about 12 hours after the initial DFOS measurement, which is why the displayed curves are referenced to this second geodetic epoch after construction. The results present maximum deviations of about 4 mm and the mean errors can be indicated with about 1.2 mm in lateral and about 2.0 mm in height direction. These values are in accordance with the theoretical analysis (cf. Figure 5.4) and confirm the suitability of the designed approach.

The continuous construction process in conventional tunneling requires fixed installation equipment (air ventilation system, electricity supply, etc.) and heavy tunnel machinery, which can restrict

the field of view to geodetic targets. Consequently, some monitoring points of selected cross-sections may be partially unavailable for displacement measurements by total stations. The DFOS-based estimation can be performed using only a selected number of supporting points (min. 2) to overcome these limitations and to provide displacements along the entire top-heading section.

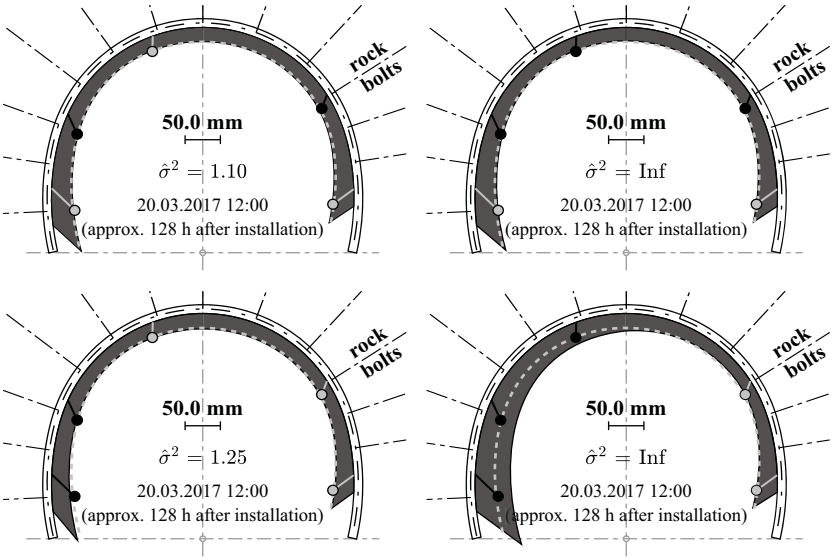

Figure 5.8: Displacement profile estimation (Monsberger and Lienhart 2021a) with different supporting points setups (used supporting points marked in gray).

The estimated displacement profiles of different setups (utilized supporting points respectively marked in gray) are shown in Figure 5.8. Estimations with uniformly distributed supporting points (Figure 5.8, top-left and top-right) depict good agreement with residuals smaller than 3 mm to the reference profile (dotted line), which represent the estimation result with all supporting points (cf. Figure 5.6d). Unilateral configurations with three geodetic points (Figure 5.8, bottom-left) at one side might be the most common

limitation in tunneling. Even with this non-uniform supporting arrangement, the DFOS approach can deliver displacement profiles with maximum deviations of about 3.5 mm to the geodetic readings. This can be advantageous, especially if one side is blocked by tunnel infrastructure over longer periods. Limitations of the DFOS-based estimation become visible, if only two supporting points at one tunnel side are used (Figure 5.8, bottom-right). Using this configuration, uncertainties of the curvature profiles might lead to a progressive error propagation starting from the supporting points, which finally result in larger deviations at the opposite tunnel side.

Geodetic monitoring in conventional tunneling involves significant risks for the surveying team on-site. Since the instrument is often positioned in the middle of the tunnel axis to obtain an optimal measurement setup, surveyors must always be attentive not to be overlooked by workers driving heavy tunnel machinery. Tragically, disastrous working accidents cannot be ruled out completely (APA 2020). For that reason, every monitoring system which reduces the physical human presence inside the tunnel is beneficial.

It is obvious that the DFOS approach also requires displacement readings to solve the boundary value problem of the double integration. If geodetic readings are however not available over longer periods of time, the displacements at the supporting point locations may be estimated from the recorded DFOS strain values. The approximated strain-displacement-relation can be defined, for instance linearly, by a minimum of two arbitrary measurement epochs i and j to predict the displacement values at the geodetic target position for the k-th epoch

$$\begin{bmatrix} \Delta x_k^{predict} \\ \Delta y_k^{predict} \end{bmatrix} = \begin{bmatrix} \Delta x_j^{TS} - \Delta x_i^{TS} \\ \Delta y_j^{TS} - \Delta y_i^{TS} \end{bmatrix} \cdot \frac{\varepsilon_k}{\varepsilon_j - \varepsilon_i} \tag{5.9}$$

where ε represents the corresponding mean strain at the target location. Using more than two measurements might optimize the

prediction, but requires also more presence of the surveyor inside the tunnel.

For concept proofing, the displacement values at the target locations of the instrumented cross-section for one selected measurement epoch (175 h after installation) were predicted from the readings about 12 and 36 hours after the installation and used to support the DFOS-based estimation. The results in Figure 5.9a demonstrate that the prediction method can provide displacement profiles with maximum deviations of about 5 mm to the exact solution.

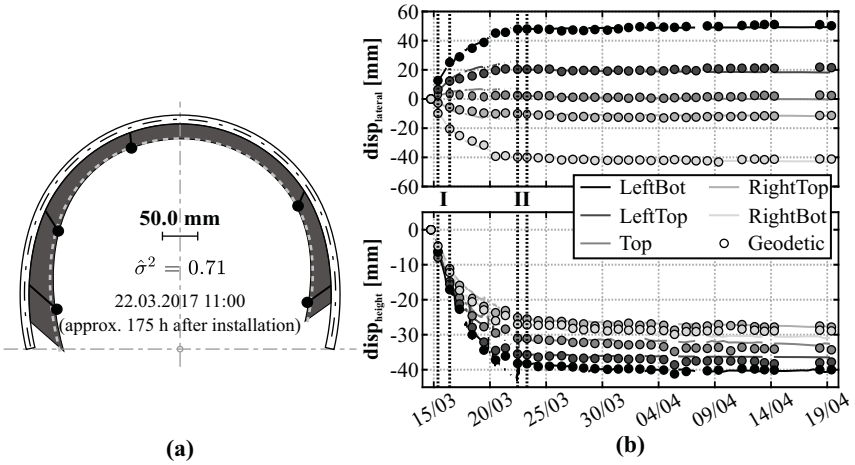

Figure 5.9: Displacement profile estimation based on supporting point prediction (Monsberger and Lienhart 2021a): **(a)** Cross-sectional displacement profile. **(b)** Displacement values at supporting point locations derived from DFOS curvature profiles over 35 days of continuous monitoring compared to pointwise geodetic measurements.

The prediction was subsequently performed for all DFOS epochs of the continuous monitoring campaign (Figure 5.9b) to analyze the method's long-term suitability. Supporting points within the first 175 hours (estimations between **I** and **II**) were predicted using the geodetic readings on the first and second day after construction (indicated with **I**). After this initial phase of about 7 days, the

invert of the cross-section has been excavated, supported as well as refilled, which essentially changes the deformation behavior. The prediction model is therefore updated with two displacement observations (indicated with **II**) to evaluate all subsequent monitoring epochs (estimations after **II**).

The comparison between the DFOS-based estimations and the geodetic readings basically depict good agreement for all target positions with mean errors of about 1.0 mm in lateral and 1.4 mm in height direction over the entire monitoring period. Remarkable is the fact that these statistical deviations are in the range or even slightly lower compared to Figure 5.7. The maximum absolute deviation of about 5 mm can be observed at the left-sided targets shortly before the update of the supporting points about 175 hours after installation. The displacement profile of this epoch is already displayed in Figure 5.9a, which, therefore, represents the estimation with the highest deviations to geodetic observations. Although this displacement accuracy might be insufficient for high-precise geotechnical monitoring applications, the resulting information certainly allows general conclusions on the deformation behavior with significantly lower presence of the surveyor inside the tunnel, in this example, 4 instead of 35 daily monitoring epochs. Moreover, distributed displacement profiles can also be determined for DFOS epochs without simultaneous geodetic measurements, which further extends the capabilities of the DFOS-based approach.

Brillouin Sensing Results (Cross-Section 02)

Even if Rayleigh interrogation units can provide strain profiles with high spatial resolution, the sensing range is restricted. Especially in tunneling applications, sensing over longer distances can be advantageous to monitor numerous cross-sections using only one interrogation unit, which is placed at a protected place, preferably outside the tunnel. Brillouin sensing systems usually enable measurements over tens of kilometers, but are limited in the spatial resolution

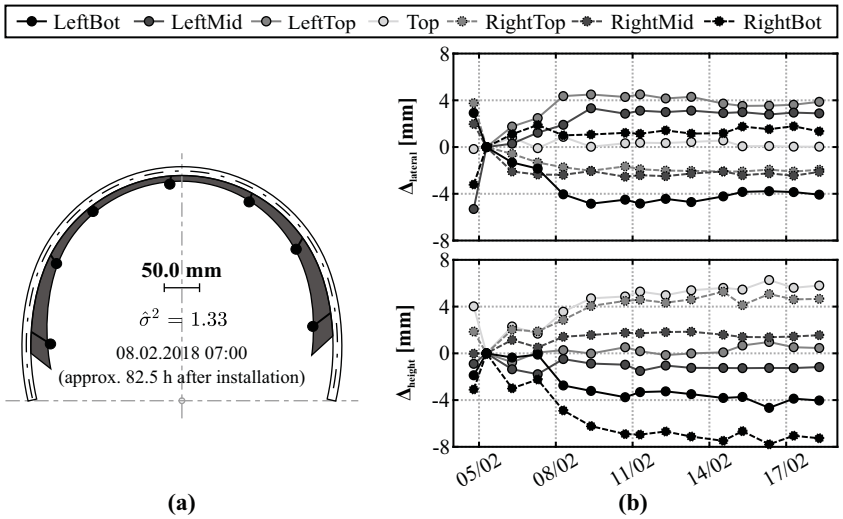

Figure 5.10: Displacement profile estimation from Brillouin measurements (Monsberger and Lienhart 2021a): **(a)** Cross-sectional displacement profile. **(b)** Coordinate residuals at supporting point locations over first 15 days of continuous monitoring.

and the measurement precision. To evaluate potential effects on the cross-sectional strain and subsequently derived displacement profiles, another cross-section was equipped with the DFOS system at the same construction lot and continuous measurements were performed using a BOFDA sensing unit (fibrisTerre 2020). The derived displacement curve of one selected epoch about 82 hours after the installation is shown in Figure 5.10a. The estimation was supported by seven geodetic targets along the entire cross-section. Their displacements are in accordance with the shape derived from the BOFDA measurements, whose estimation redundancy delivers an a-posteriori variance factor $\hat{\sigma}^2$ of about 1.33. This also confirms the correctness of the statistical model at a significance level of 95%.

Analogous to Figure 5.7, the DFOS displacement profiles can be estimated at each geodetic measurement epoch to analyze typical

variations between the different sensing approaches. The coordinate residuals at all seven geodetic target positions over the first 15 days of continuous monitoring are displayed in Figure 5.10b. The different curves were referenced to the second geodetic epoch about 10 hours after installation, where simultaneous results of both technologies are available for the first time. The derived deviations are within a range of about ±5 mm in both coordinate directions, except for the right bottom target, and the mean errors of about 2.2 mm in lateral and 2.7 mm in height direction are comparable to Rayleigh sensing results. The higher number of supporting points could however also be used for data snooping to detect and eliminate potential outliers in the curvature profiles or the supporting point displacements. This would potentially further optimize the estimation results.

5.4.2 Tunnel Shaft Linings

Intermediate headings with shaft constructions are widely used in modern conventional tunneling to shorten construction times. The SBT project includes shafts at three construction lots with depths of up to 400 m (Gobiet et al. 2017). As shown in Figure 5.11a, the Göstritz intermediate access as part of the SBT 1.1 (Figure 5.5) requires a complex construction system. Two horizontal access tunnels with a total length of more than 1 km each were built with a massive cavern at the end, which subsequently enabled the construction of two vertical shafts with a total depth of approximately 240 m to reach the planned altitude of the future railway line.

Exploration drillings revealed very challenging geological conditions for the shaft constructions, which is why an extended monitoring program was set-up to detect any degradation of the structural stability of the linings. Conventional geodetic measurements of shaft walls using total stations are very difficult due to very steep, almost vertical sightings as well as water intrusion at the shaft floor. Furthermore, the shaft construction must always be completely paused

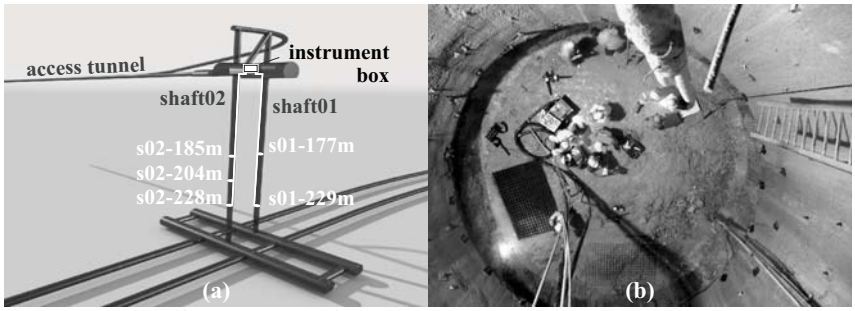

Figure 5.11: Tunnel shaft lining monitoring at Göstritz access point (Monsberger and Lienhart 2021a): **(a)** Schematic representation of construction site (based on Gobiet and Wagner 2013) and DFOS monitoring setup. **(b)** Vertical view down the shaft during sensor installation (Lienhart et al. 2019).

during the time-consuming measurements, which, therefore, delay the construction process as a whole.

To overcome these limitations, DFOS cables were embedded into five selected shaft cross-sections based on the geological conditions to measure distributed strain and temperature profiles in circumferential direction of the shotcrete linings. An instrumentation along both shotcrete layers also enables an assessment of potential curvature changes. The cable routing was recorded by total station measurements before shotcreting to ensure the exact position along the lining. These measurements as well as the installation itself were challenging due to small working space inside the shaft as well as permanent water intrusion (Figure 5.11b). The sensing cables of all cross-sections were guided from water-proof connection boxes at the cross-section locations to an instrument box at the shaft head, from where measurements can be carried out without any interference of the regular construction.

Contrary to partial excavations in conventional NATM tunneling, the continuous construction of tunnel shaft linings enables an installation along the entire cross-section at the same time and can provide a closed ring system along both sensing layers. Based on

this configuration, the boundary value problem of the DFOS-based estimation can be solved by assuming that the displacement value and its gradient at the starting point must be equivalent to the last integration position by extending the functional model with constraints instead of pointwise displacement readings (cf. Equation 5.2 to 5.6). These constraints can be realized in various ways, e.g. by pseudo observations:

$$\begin{bmatrix} \kappa_1^x \\ \vdots \\ \kappa_n^x \\ 0 \\ 0 \end{bmatrix} = \begin{bmatrix} \frac{1}{h^2} & \frac{-2}{h^2} & \frac{1}{h^2} & 0 & \cdots & \cdots & \cdots & 0 \\ \vdots & \ddots & \ddots & \ddots & \ddots & \ddots & \ddots & \vdots \\ 0 & \cdots & \cdots & \cdots & \cdots & \frac{1}{h^2} & \frac{-2}{h^2} & \frac{1}{h^2} \\ 1 & 0 & \cdots & \cdots & \cdots & \cdots & 0 & -1 \\ -2 & 1 & 0 & \cdots & \cdots & \cdots & 0 & 1 \end{bmatrix} \cdot \begin{bmatrix} \Delta x_0 \\ \Delta x_1 \\ \vdots \\ \Delta x_{n+1} \end{bmatrix} \tag{5.10}$$

$$\begin{bmatrix} \kappa_1^y \\ \vdots \\ \kappa_n^y \\ 0 \\ 0 \end{bmatrix} = \begin{bmatrix} \frac{1}{h^2} & \frac{-2}{h^2} & \frac{1}{h^2} & 0 & \cdots & \cdots & \cdots & 0 \\ \vdots & \ddots & \ddots & \ddots & \ddots & \ddots & \ddots & \vdots \\ 0 & \cdots & \cdots & \cdots & \cdots & \frac{1}{h^2} & \frac{-2}{h^2} & \frac{1}{h^2} \\ 1 & 0 & \cdots & \cdots & \cdots & \cdots & 0 & -1 \\ -2 & 1 & 0 & \cdots & \cdots & \cdots & 0 & 1 \end{bmatrix} \cdot \begin{bmatrix} \Delta y_0 \\ \Delta y_1 \\ \vdots \\ \Delta y_{n+1} \end{bmatrix} \tag{5.11}$$

The extension allows an estimation of relative displacement profiles along the shaft lining free of external observations. Although rigid-body motions of the linings remain unknown, this procedure can be very valuable to obtain the shaft's deformation behavior without any interruption of the shaft construction.

Initial measurements of the instrumented shaft linings were taken immediately after the installation using the BOFDA interrogator. Up to now, follow-up monitoring has been conducted epoch-wise on demand of the geotechnical engineer on-site. The setup is however also capable for continuous monitoring with higher temporal resolution if required. This thesis only discusses the application of the shape sensing algorithm to monitoring epochs of one selected cross-

section. Details about the sensing concept and further measurement results are introduced in Lienhart et al. (2019).

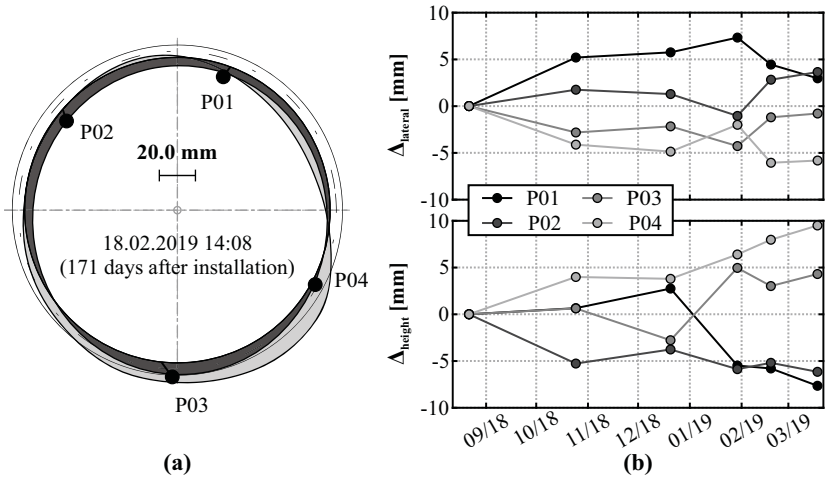

Figure 5.12: Shaft monitoring results at shaft 02-228m (Monsberger and Lienhart 2021a): **(a)** Cross-sectional displacement profiles estimated from fiber optic sensing (light gray) and displacement ellipse derived from geodetic measurements (dark gray). **(b)** Coordinate residuals at geodetic target locations.

The evaluated cross-sectional displacement profile (s02-228 m) about 6 months after the installation is shown in Figure 5.12a. It presents only small displacements within a range of about ±13 mm, where the cross-sectional shape is slightly squeezed and orientated to the right-bottom side. To verify the DFOS-based approach (light gray), the deformation shape can also be approximated by an ellipse based on the geodetic displacements measured by total station (dark gray). The individual profiles of both technologies were reduced by their respective mean value since the DFOS approach depicts only relative deformation within the lining. The orientation of the geodetic ellipse basically represents the deformation progress, although this estimation shows lower deformation magnitudes. Numerical deviations between the sensing techniques at

the geodetic target positions are within a range of some millimeters (Figure 5.12b) and, therefore, only slightly lower than the total deformation amount. The differences increase over time, which might be also related to the increasing sighting steepness due to the further shaft sinking process. This usually results in higher measurement uncertainties for geodetic monitoring.

The DFOS-based approach can be a valuable substitute to capture the relative deformation profiles along shaft linings without physical access of the surveyor or delays of the construction process. The author however emphasizes that the study presented in this thesis is restricted to one monitoring cross-section with five follow-up measurements and minimal deformation magnitudes. Further investigations on shape estimations without supporting points are definitely required beyond the scope of this thesis to provide a more comprehensive analysis of the capabilities.

5.5 CONCLUSIONS

The sensing and evaluation methodology presented in this chapter demonstrates that DFOS can not only capture one-dimensional strain information, but can also enable fully-distributed shape assessment along curved structures, such as tunnel cross-sections. The concept is based on the double integration of distributed curvature values derived from DFOS strain profiles along two layers in well-known arrangement along the structure, which are combined with traditional geodetic displacement readings. Stochastic analysis could show that the curvature's measurement uncertainty is related to the DFOS strain measurements, the distance between the fibers as well as the accuracy of the geotechnical planing model. The standard deviation of the estimated displacement profile also strongly depends on the geodetic measurement precision.

Evaluations of continuous monitoring of tunnel cross-sections present that the distributed displacement shape can be assessed without any gaps along the entire top-heading section under tunnel

site conditions. The comparison between geodetic measurements and DFOS derivations at the target positions over time depicts mean errors in the low millimeter range for high-resolution Rayleigh as well as Brillouin interrogation units, which also confirms the stochastic analysis. The DFOS-based approach is also capable to predict supporting information based on the measured strain values along the lining. It could be shown that displacement profiles with mean errors of about 1 mm in both coordinate directions at the supporting point locations can be determined by using only 4 instead of 35 geodetic measurement epochs. This setup would significantly reduce the surveyor's physical presence inside the tunnel.

The closed ring system along tunnel shaft linings enables an estimation of relative displacement profiles, even without external observations. The resulting shape allows conclusions on the deformation behavior of the instrumented shaft cross-section. Even if the displacement magnitude is minimal, the deformation progress and orientation can be verified by evaluations of an ellipse estimated from geodetic displacement readings. It is however obvious that further studies are required beyond this thesis to analyze the shape estimation capabilities without supporting points in more detail.

6

Application III: Concrete Structures

Disclaimer and Acknowledgement

This chapter is based on the publication listed below. Figures, texts and contents are therefore already partly or fully published.

C. M. Monsberger and W. Lienhart (2021b). "Distributed Fiber Optic Shape Sensing of Concrete Structures." *Sensors* 21(18): 6098

The presented concrete structures were designed, realized and tested within numerous research projects in cooperation with different partners. I want to acknowledge the contribution of the Institute of Structural Concrete (namely Christoph Betschoga) and the Laboratory for Structural Engineering at Graz University of Technology as well as the Chair of Subsurface Engineering (namely Paul Gehwolf) at Montanuniversität Leoben.

6.1 MOTIVATION

The identification and localization of local deficiencies is essential to evaluate the integrity of civil engineering structures. Concrete is usually affected by inclusions or cracks, which result from the construction process itself or loads during operation. The sensor location and its corresponding gauge length is therefore essential when using strain sensors inside concrete, cf. Figure 6.1. Long-gauge sensors are able to capture the overall behavior of the structure, but are limited to identify local homogeneities. FBG sensor chains along the structure or point sensors with smaller gauge length can provide the local strain behavior at selected locations, however, with the drawback that events between the sensitive elements might be overlooked.

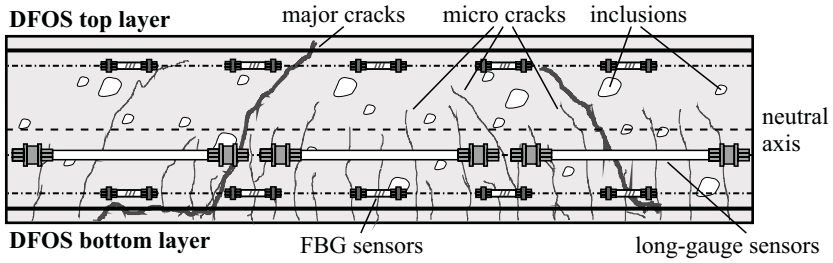

Figure 6.1: Strain sensing of concrete structures (Monsberger and Lienhart 2021b).

The distributed sensing feature of DFOS systems here enables both, the comprehensive, gapless acquisition of the strain behavior and the localization of local defects, and can be advantageous compared to traditional embedded sensors. A wide range of laboratory studies on crack detection and localization using DFOS along concrete beam structures is known in literature. These discuss different sensor installation techniques, such as bonding along the beam's surface using various sensing fibers (Billon et al. 2015) and adhesives (Barrias et al. 2019), mounting cables inside the con-

crete (Bassil et al. 2019), or gluing in grooves along reinforcement bars (Liu et al. 2020). The resulting DFOS strain profiles can either be utilized to calibrate developed strain transfer models (Henault et al. 2012; Bassil et al. 2020), to derive effective crack widths along the structure (Fischer et al. 2019; Zhang et al. 2021) or to establish alert levels for CSHM applications (Zhang et al. 2006).

The evaluation of curvature and bending characteristics along civil infrastructure can supply beneficial information to compare the actual condition, including for instance damages and fatigue, to the construction and planning state. Investigations already demonstrated that long gauge strain sensors are suitable for strain-based shape sensing (Glišić 2011; Sigurdardottir et al. 2017), if the sensors are appropriately arranged along the structure and the loading scenario is known. DFOS, however, enables new capabilities for in-situ shape sensing inside concrete due to the fully-distributed sensing feature in combination with high spatial resolution. Deflection profiles can be derived without detailed knowledge of the loading situation, if two or more boundary conditions are known (Brault et al. 2019).

This chapter presents a comprehensive analysis of distributed fiber optic shape sensing of concrete structures. The study includes detailed investigations on concrete beams using different fiber optic sensors and installation techniques, as well as monitoring of real-scale tunnel lining segments. The results were proven using, inter alia, pointwise displacement readings and distributed image-based measurements.

6.2 SENSOR INSTALLATION TECHNIQUES

The sensor attachment and installation along the monitoring object is critical in general to guarantee the strain transfer from the structure to the sensing cable. The stress behavior inside civil engineering structures usually varies depending on material properties, loading conditions, etc. Therefore, the sensors must be placed not

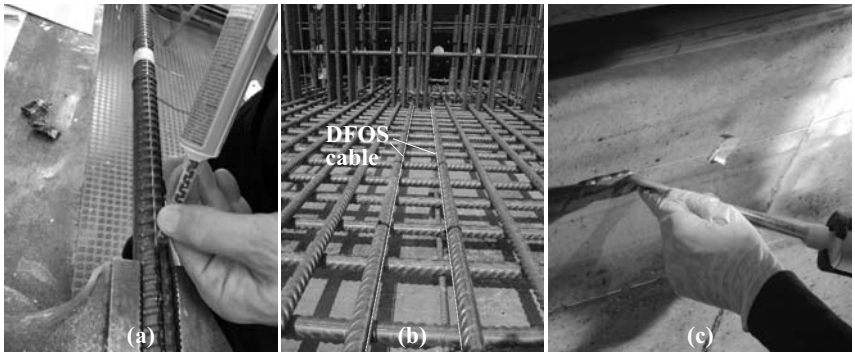

Figure 6.2: Sensor installation techniques (Monsberger and Lienhart 2021b): **(a)** Application along reinforcement. **(b)** Installation inside concrete. **(c)** Application along surface.

only at applicable locations, but also using the suitable installation technique with respect to the project requirements.

For concrete structures, applications inside the structure as well as along the surface are practicable. The monitoring results however significantly vary depending on the installation location and the used DFOS cable type. Reinforced concrete objects enable the direct sensor application inside the structure, where either bare fibers or tiny cable types (cf. Figure 3.7d–e) may be glued with appropriate adhesives (Figure 6.2a) on the steal surface or inside grooves to assess the steel strain behavior. More robust sensing cables (cf. Figure 3.7a–c) can be attached to the reinforcement bars using cable ties (Figure 6.2b) to capture the concrete capacity. The reinforcement itself also involves the advantage that the cable is better protected during the casting process, especially in case of high concrete pumping pressure.

DFOS surface applications in civil engineering are particularly beneficial for subsequent instrumentation and monitoring. Flexible, tight-buffered sensing fibers can be individually guided along the surface for an areal coverage of conspicuous regions like surface crack areas or similar. As depicted in Figure 6.2c, the fiber can be

directly glued onto the surface using adhesive mortars, which also protect the optical fiber against mechanical impacts and provide higher robustness in practical environment.

6.3 LABORATORY BEAM TESTING

The interactive behavior of embedded sensors within the structure must be well understood before the installation to perform an appropriate data acquisition and interpretation. Depending on the sensor application method, the location of the sensor as well as the used sensing technology, divergent findings can be derived from fiber optic strain measurements, especially within an inhomogeneous structure like concrete (cf. Figure 6.1).

To understand the sensor behavior in a suitable manner, numerous concrete beams were instrumented using several sensor types and installation techniques like gluing of FiMT or TB fibers along the beam's reinforcement, installation of sensing cables inside the concrete along the reinforcement, or gluing of TB fibers along the surface. The installations were monitored during vertical and biaxial loading tests using DFOS units based on Rayleigh and Brillouin scattering as well as by quasi-distributed FBG interrogators.

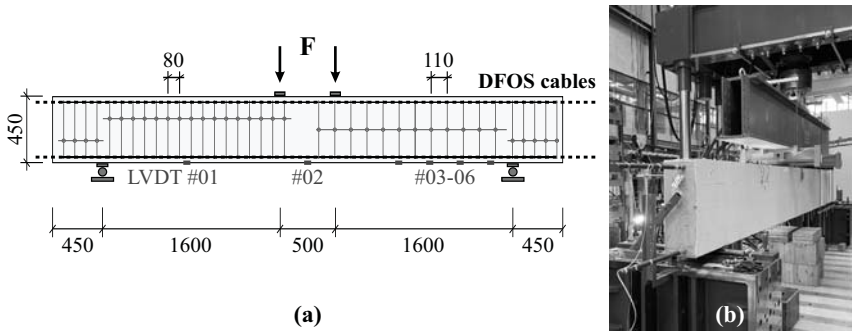

Figure 6.3: Laboratory beam testing (Monsberger and Lienhart 2021b): **(a)** Schematic representation of beam structure (dimensions in mm). **(b)** Instrumented concrete beam mounted at testing facility.

As an example, Figure 6.3 shows the schematic representation of one instrumented beam structure with a total length of 4.6 m and the corresponding setup at the testing facility. This test was carried out as a 4-point loading test, where the loading points are shifted 250 mm from the center, respectively. Besides the fiber optic sensing cables installed in two separate planes along the compression and tension reinforcement, the structure's displacements were captured at six selected locations using Linear Variable Differential Transducers (LVDT).

6.3.1 Assessment of Installation Techniques

Within the first beam load test presented in this thesis, the aim was to evaluate the impact of three different sensor application methods not only on the DFOS measurements, but also on the derived displacement curves. Figure 6.4a–c depicts the strain profiles measured by the OBR interrogation unit along the top and bottom sensing layer with a spatial resolution of 10 mm at four selected load steps from 100 to 400 kN (three load steps only for Figure 6.4c due to a fiber breakage). The strain profiles present an asymmetric behavior along both layers, which can be explained by the different amount of reinforcement with lower degree along the bottom compared to the top side of the beam. Furthermore, the outcomes strongly vary depending on the sensor location as well as the attaching technique. For instance, measurements along the tight-buffered fiber glued along the reinforcement bars (Figure 6.4a) show smoothed strain profiles with almost no irregularities, whereas the same fiber type glued along the surface (Figure 6.4c) depicts a heterogeneous behavior with numerous strain maxima. These strain peaks can be related to cracks, which are arising along the concrete's surface with increasing load.

Nevertheless, by applying appropriate low-pass filtering techniques like Moving AVerage (MAV) filter (here: filter length of 1 m) or polynomial filter (here: fourth-degree polynomial), it can be

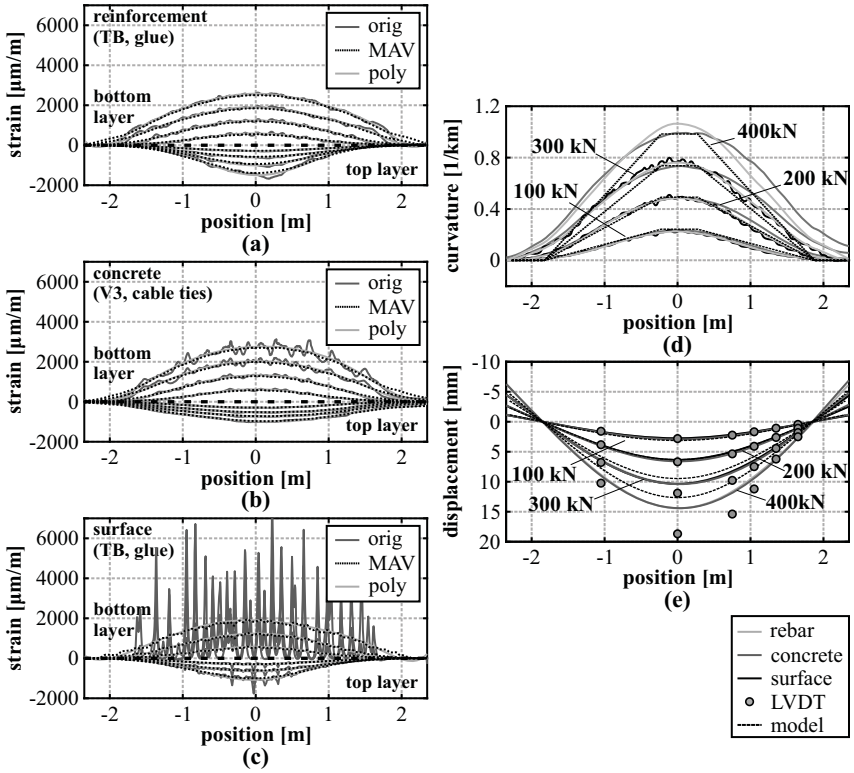

Figure 6.4: Analysis of different installation techniques (Monsberger and Lienhart 2021b): **(a)** Strain profiles along reinforcement (tight-buffered fiber, glue). **(b)** Strain profiles inside concrete (BRUsens V3, cable ties). **(c)** Strain profiles along surface (tight-buffered fiber, glue). **(d)** Curvature values derived from DFOS strains and theoretical model. **(e)** Displacement curves calculated from DFOS strains, measured by LVDT and theoretical model.

shown that the different sensor responses underlie the same structural behavior. This suggests that the strain-based shape sensing approach is applicable, even if the respective sensor output itself is essentially different. This knowledge also enables the possibility for subsequent installations in practical applications, where the sensor could not been installed during the construction.

The curvature profiles along the beam (Figure 6.4d) derived by relating the strain sensing layers of the different installation technique (here: MAV filtered) agree well to each other and also to the theoretical model, especially up to a load of 200 kN, where also the shape of the 4-point load setup can be well identified. Resulting from the test setup, it can be assumed that the beam's supporting points at each side (1850 mm from the center) are stable to evaluate the distributed displacement curves along the beam depicted in Figure 6.4e. The results basically confirm the curvature profiles with good agreement to the LVDT sensors up to a load of 200 kN. At higher load steps, the displacement curves of different installation techniques match themselves, but significant deviations become visible, to the theoretical model, negatively, and to the LVDTs, positively. This leads to the assumption that the concrete beam can not fulfill the Bernoulli hypothesis of the consistent cross-sectional profile, which is why the strain-based shape determination algorithm is not capable to capture the actual displacement behavior after major cracking has arisen along the structure.

Notable is the fact that also the theoretical model depicts essentially smaller displacements compared to the LVDT sensors, even with lower magnitude than the DFOS derivations. To investigate this conspicuous behavior in more detail, two respective sensing fibers were also installed in separate layers along the compression and tension reinforcement of the beam, which enables an analysis of the deformation behavior within the cross-sectional profile of the reinforcement bar without the concrete altering effect. Figure 6.5a shows the measured strain profiles along both instrumented layers of the tension reinforcement before and after the substantial cracking occurred along the beam. At a load step of 200 kN, the strain distributions depict a similar behavior with a slight offset in the middle area due to the vertical loading of the structure. With increasing load, however, not only the strain offset between the layers increases, but also significant bending becomes visible within the

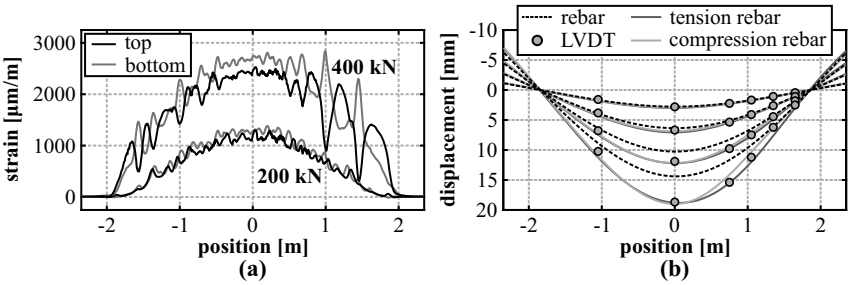

Figure 6.5: Optimized sensing approach along the reinforcement (Monsberger and Lienhart 2021b): **(a)** Strain profiles measured along two layers of tension reinforcement. **(b)** Derived displacement curves.

area between 1.0 and 1.5 m. This bending effect is the result of a major shear crack, which arises due to the applied vertical loading and the lower degree of reinforcement at the right-hand side of the beam (cf. Figure 6.3). The measured data suggest that this crack causes a local buckling of the beam in vertical direction. Neither the theoretical beam model nor the strain-based DFOS derivation in different planes along the beam can cover this effect. Similar conclusions on the shear cracking impact were already drawn in literature (Poldon et al. 2019). The derived displacement curves in Figure 6.5b show that the actual deformation behavior of the beam, represented by the LVDT measurements, can be solidly captured even at higher load steps, when the determination is performed individually for each reinforcement layer.

Between the load steps of 300 and 400 kN, slight deviations between the compression and tension reinforcement become visible along the shear cracked side of the beam. These can further be analyzed by comparing the deformation process for all different DFOS approaches at the selected LVDT locations over time, see Figure 6.6 (displacement axis scale individually adjusted for each sensor position for better visibility). The results demonstrate that the beam basically follows two different states: Along the outside area at the locations of LVDT #05 and #06 (Figure 6.6a–b), the

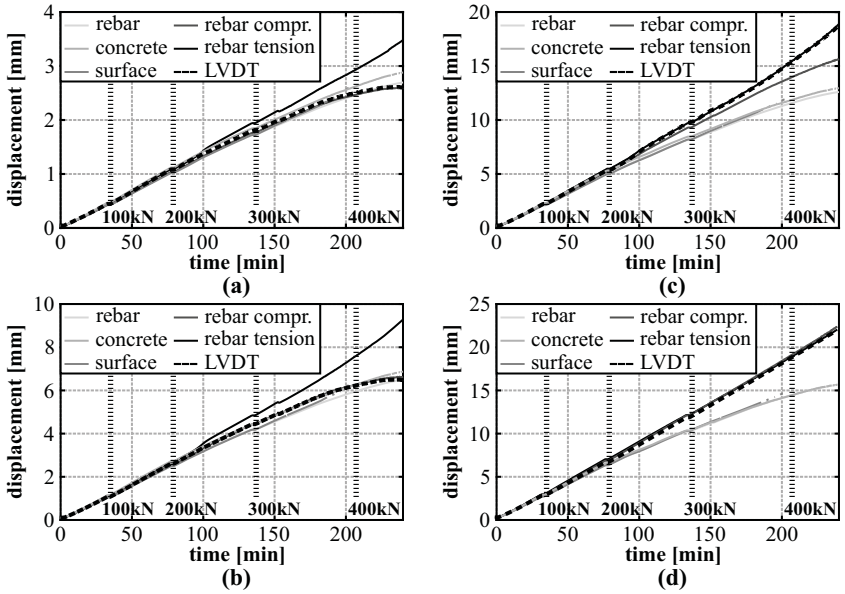

Figure 6.6: Comparison between DFOS and LVDT displacements over time (Monsberger and Lienhart 2021b): **(a)** LVDT #06 (+1.65 m). **(b)** LVDT #05 (+1.35 m). **(c)** LVDT #03 (+0.75 m). **(d)** LVDT #02 (0.00 m).

system depicts a nonlinear behavior at higher loads and reproduces the concrete behavior after cracking. Shape and magnitude of the deformations can also be captured within all DFOS derivations, except for the installation along the tension reinforcement. In contrast, the middle area of the beam at the positions of LVDT #02 and #03 (Figure 6.6c–d) displays an almost linear displacement increase and follows the deformation behavior of the reinforcement bar. This assumption can also be supported by the relative errors of the DFOS displacements with respect to the LVDTs derived at a load level of 300 kN (last load step before fiber breakage along surface installation), which are listed in Table 6.1.

Nonetheless, up to a load of about 220 kN, the DFOS displacements agree well to the LVDT sensors and represent the beam's

Table 6.1: Percentage errors of different installation techniques at the 300 kN load step.

LVDT		**rel. error** [%]				
no.	pos.	rebar	concrete	surface	rebar tension	rebar compr.
#01	−1.05 m	5.0	3.9	3.8	10.4	9.7
#02	0.00 m	13.8	12.7	12.9	2.6	2.2
#03	+0.75 m	16.1	13.2	15.7	0.0	4.3
#04	+1.05 m	14.5	10.5	14.2	1.5	5.8
#05	+1.35 m	5.5	0.1	5.3	9.6	0.2
#06	+1.65 m	3.9	2.7	3.8	8.3	1.8

actual deformation behavior independent from the sensor location and its application. Here, the mean percentage error at the LVDT locations range from 2.9% (concrete) to 5.1% (surface), equal to a maximum absolute deviation of lower than 0.2 mm. All tested installation techniques seem therefore to be practicable to monitor distributed displacements along civil infrastructure objects within the usual working range before major cracking.

6.3.2 Assessment of Sensing Principles

The spatial resolution of the interrogation technique majorly influences the outcome of the strain-based shape-sensing approach. This relation can be further analyzed for practical environments based on another concrete beam sample with a total length of 6 m, which was instrumented with the BRUsens V3 strain sensing cable in two layers. During the 4-point loading test, the sensors were interrogated by the OBR unit ($\Delta z = 10$ mm) as well as using a Brillouin Optical Frequency Domain Analyzer (BOFDA) with a spatial resolution of 50 cm. Additionally to the DFOS cables, two FBG sensor chains (10 FBGs per chain) were attached along the bottom and top reinforcement layer of the beam, which also enables a direct comparison between quasi-distributed sensors and DFOS for model-free

shape-sensing methods.

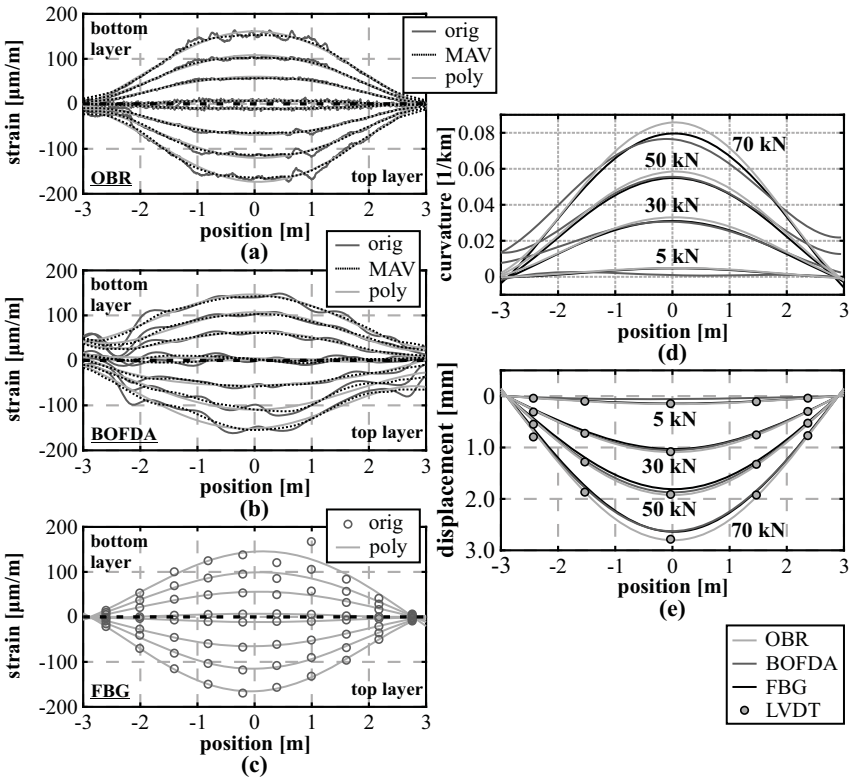

Figure 6.7: Analysis of different sensing units (Monsberger and Lienhart 2021b): **(a)** Distributed strains (OBR). **(b)** Distributed strains (BOFDA). **(c)** Quasi-distributed strains (FBG) **(d)** Derived curvature profiles. **(e)** Displacement curves calculated from DFOS strains and measured by LVDT.

Figure 6.7a–c depicts the strain values measured by the different technologies at four selected load steps (5 kN, 30 kN, 50 kN, 70 kN). For this example, lower load steps within the estimated elastic range of the beam were chosen to avoid major influences due to concrete cracking, which is not within the focus of this investigation. By comparing the strain profiles of the different DFOS technologies

(Figure 6.7a–b), it is obvious that the BOFDA technique can also solidly reproduce the shape and magnitude of the applied load, even if the OBR provides a higher quality with respect to spatial resolution and measurement precision. The installed FBG sensors deliver 10 pointwise strain readings along both layers, which can be distributed along the beam, e.g. by polynomial fitting (here: forth-degree polynomial). The resulting strain curves show a similar behavior compared to the DFOS distributions. While the polynomial fit also agrees well with the individual FBG values along the compression reinforcement, two sensing locations (+0.39 m and +0.99 m) along the tension reinforcement depict divergent readings. Contrary to a strict pointwise analysis, their impact on the strain curves is however limited due to polynomial fitting.

The derived curvature profiles (Figure 6.7d) as well as the distributed displacement curves along the beam (Figure 6.7e) show that the beam's vertical bending behavior can be clearly identified within all sensing approaches and the numerical displacements coincide well with the LVDT values.

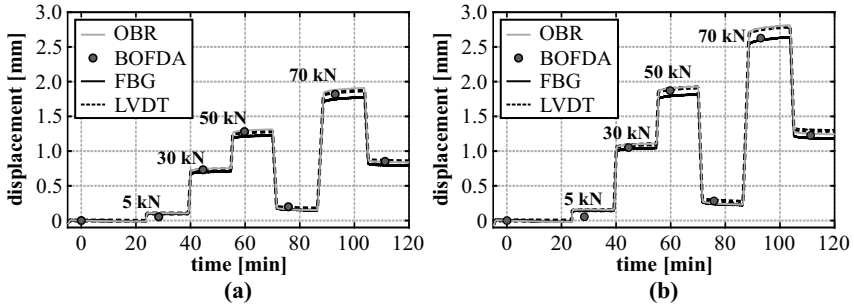

Figure 6.8: Comparison between DFOS and LVDT displacements over time (Monsberger and Lienhart 2021b): **(a)** LVDT left (−1.50 m). **(b)** LVDT center (+0.00 m).

The temporal order of the individual load steps, depicted for two selected LVDT locations over time in Figure 6.8, demonstrates

that the individual loading sequences can be reliably identified, and even the smallest load level of 5 kN with a displacement change of only 0.15 mm can be well separated using the OBR as well as the FBG-based sensing approach. The measurement repeatability (1σ-level) of the different sensing principles, derived from subsequent measurements at a constant load of 30 kN, can be indicated with about 0.04 mm (BOFDA) and lower than 0.01 mm (OBR/FBG).

Table 6.2: Percentage errors of different sensing units at load step of 70 kN.

LVDT		**rel. error [%]**		
no.	pos.	OBR	BOFDA	FBG
#01	−2.40 m	9.4	9.3	15.2
#02	−1.50 m	1.0	1.1	4.9
#03	0.00 m	0.5	3.1	5.4
#04	+1.50 m	1.3	3.2	6.1
#05	+2.40 m	3.9	3.2	8.6

The percentage errors between the LVDT sensors and the strain-based shape sensing approaches at the highest load step of 70 kN in Table 6.2 show deviations ranging from approx. 1% to 6%, except for the LVDTs at the outside locations. The relative errors of the distributed technologies also coincide with the laboratory test results of the steel anchor presented in Section 4.3.2. It is emphasized that the individual shape sensing approaches (especially BOFDA and FBG) might be further optimized by eliminating single sensing points from the strain curve fitting, which is however not further pursued at this point.

Besides the vertical loading, the investigated beam was also exposed to normal forces (see Figure 6.9a) to increase the loading capacity within the non-cracked state for further investigations. This bi-directional loading scenario of the beam sample enables an assessment of the strain-shape sensing method in the event of a force superposition. The resulting displacement curves in Figure 6.9b show that the normal force application (here: 1600 kN) results in a heave of the beam in the middle area, which is stepwise compensated by

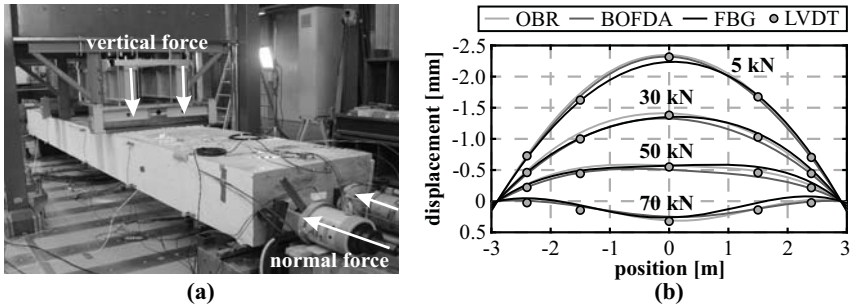

Figure 6.9: Combination of vertical loading and normal force (Monsberger and Lienhart 2021b): **(a)** Test setup. **(b)** Displacement curves derived from DFOS strains and measured by LVDT.

the vertical load introduction. The loading combination can be well reproduced by all sensing technologies and agree again to the LVDT displacements in shape and magnitude within the specified range.

6.4 PRECAST TUNNEL LINING SEGMENTS

When using tunnel boring machines (TBMs) for tunnel excavation works, it is state-of-the-art to apply precast concrete lining segments, which are usually set up in a ring of four to eight elements to support the excavation cavity. The knowledge about the degree of utilization of these segments is crucial to ensure safe tunnel construction works. IGMS in cooperation with the Chair of Subsurface Engineering (Montanuniversität Leoben, MUL) therefore designed a patented DFOS approach (Lienhart and Galler 2016) to assess the fully-distributed strain behavior inside precast tunnel segments.

6.4.1 Sensing Concept and Sensor Installation

The concept is based on one single sensing cable per segment, which is guided along the reinforcement or any supporting structure for steel fiber concrete segments (Soga et al. 2015). This enables the

realization of a sensing grid (Figure 6.10) in two layers along the object (typically inner and outer reinforcement layer) with well-known distance between the cables, especially important for the shape sensing approach.

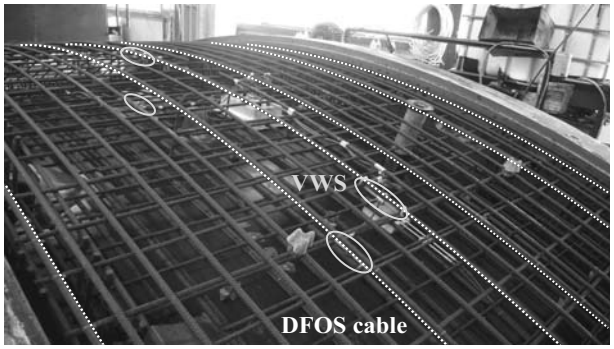

Figure 6.10: Tunnel lining segment manufacturing with installed DFOS cable and vibrating wire sensors (VWS).

The complete coverage of the tunnel segment can produce hundreds or even thousands of strain sensing points depending on the used measurement principle and the cable guiding. Here, practical experiments during the installation on-site showed that the BRUsens V9 cable (cf. Figure 3.7) can provide an appropriate trade-off between sensor protection, strain transfer and guiding flexibility. The fiber optic connectors are stored in connection boxes for protection during the concreting process. Inside the tunnel, the individual concrete segments can be connected to one continuous sensing loop to evaluate the ring's overall behavior (Monsberger et al. 2018c).

6.4.2 Bi-Axial Loading Test Rig

To investigate the load-bearing and deformation behavior of precast tunnel lining segments under well-known loading conditions, the Austrian Federal Railways (OeBB Infrastructure AG) in cooperation with MUL developed and realized a special test rig (Fig-

ure 6.11). The facility enables bi-axial testing of real-scale segments with different geometries and dimensions to optimize the segment design (Gehwolf et al. 2015). The basic measurement equipment of the rig includes wire-rope LVDT sensors to measure the vertical deformations as well as strain gauges and extensometers at the segment's surface. Similar to the laboratory investigations of the steel anchors presented in Section 4.3, DIC measurements along the face side were performed at selected tests to independently verify the DFOS approach over the entire length of the tunnel segment.

Figure 6.11: Test rig for real-scale tunnel lining segments (based on Monsberger and Lienhart 2021b).

6.4.3 Shape Sensing Results

In addition to two completed ring installations inside a railway tunnel in Austria with 13 segments in total, the deployed DFOS approach was also implemented into eight tunnel segments to validate the system under controlled vertical, horizontal and bi-axial loading at the test rig. Reference is given to Gehwolf et al. (2016), Monsberger and Lienhart (2017), and Monsberger et al. (2018c) for information about the practical realization inside the tunnel and general monitoring results.

This section discusses results with focus on the shape sensing capabilities. At this point, it must be noted that the individual sensing layers along the tunnel lining segment are initially curved before loading, contrary to linear beam structures. This bent state must be well considered within the shape-sensing algorithm, whose implementation is introduced in detail in Section 5.2. Moreover, the test rig's supporting points are flexible and change their orientation at the left and right side due to the applied load. The double integration process of all presented segments has therefore been supported by numerous LVDT sensors, which also provide an estimation with redundancy.

Noteworthy is also the fact that the DFOS approach is not capable to capture torsion at the joints between the individual segments of a complete ring system inside the tunnel. At these locations, additional 2D displacement transducers could be used to support the double integration process and, finally, to provide a holistic view of the entire cross section (cf. Jiao and Zhou 2021).

Vertical Loading: Comparison to Conventional Sensors

The first presented tunnel segment specimen was subjected to one-axial loading in vertical direction, where the load was stepwise increased (50 kN to 450 kN in steps of 50 kN). The curvature profiles resulting from the high-resolution OBR measurements displayed for one selected reinforcement layer in Figure 6.12a coincide with the general assumption of vertical bending due to the applied load. The curvature values derived from the original strain data along both layers however depict major irregularities. These can be related to cracks, which arise along the inner (tension) reinforcement of the segment. The curvature can be smoothed by filtering the original strains using a low-pass MAV filter (here: filter length of 1 m) to reduce the impact of local strain effects.

The utilization degree of tunnel lining segments is usually derived based on curvature values from strains measured by pairs

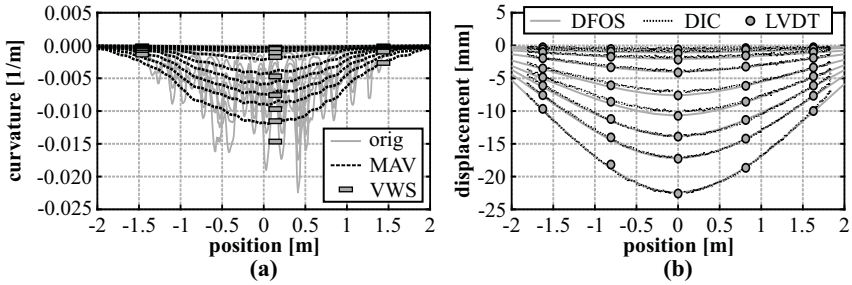

Figure 6.12: Vertical loading from 50 kN to 450 kN in 50 kN steps (Monsberger and Lienhart 2021b): **(a)** Curvature values derived from DFOS strains and VWS readings. **(b)** Displacement curves calculated from DFOS strains and DIC compared to pointwise LVDT readings.

of vibrating wire sensors (VWS) at specific locations along both reinforcement layers (Radončić et al. 2015). These sensors deliver strains within a gauge length of 15 cm and were also installed within the observed segments for verification purposes (Figure 6.10). The resulting curvatures of three pairs of VWS sensors in Figure 6.12a basically agree with the values determined from the original DFOS data, but it seems that the derived value strongly depends on the sensor position itself. Especially in case of major local distortions like cracks, the utilization behavior might hence be evaluated erroneously, although the local strains and curvature values are correctly determined. Here, the DFOS system can provide both, local stress events as well as the overall assessment of the structural behavior by applying appropriate filtering techniques.

Considering the initial shape of the structure, distributed displacement curves along the entire segment can be derived from the DFOS curvature values for each load step, see Figure 6.12. The stepwise loading increase can be clearly identified within the data and the numerical displacements agree well with LVDT sensors in shape and magnitude, even if this is partly implied by the correlation within the sensing algorithm (cf. Section 5.2).

Table 6.3: Percentage errors for each load step during vertical loading at locations of LVDT sensors and mean percentage error with respect to distributed DIC measurements.

	rel. error [%]					
load	#01	#02	#03	#04	#05	DIC
	−1.65 m	−0.85 m	0.00 m	+0.85 m	+1.65 m	—
50 kN	12.0	9.1	2.1	23.2	11.4	39.3
100 kN	9.2	3.0	7.5	47.6	9.4	26.4
150 kN	5.9	0.2	5.5	12.6	9.3	14.7
200 kN	3.1	0.1	2.5	3.0	5.3	5.7
250 kN	2.4	3.4	0.3	0.2	4.1	6.5
300 kN	2.1	3.2	0.8	1.5	3.9	4.8
350 kN	1.3	2.4	0.7	0.2	3.0	1.7
400 kN	0.8	2.2	0.6	0.6	2.5	1.4
450 kN	0.3	2.4	0.8	0.0	2.1	1.3

The percentage errors of the DFOS derivations in relation to the individual LVDT sensor locations basically decrease with increasing load (Table 6.3). Especially at load steps of 150 kN and lower, the behavior can be explained by the small deformation magnitudes, which result in significantly higher relative errors at lower loads. This relation was already demonstrated by DFOS investigations along concrete beams (Berrocal et al. 2021). For higher load steps, the relative errors at the LVDT positions are continuously decreasing with maximum absolute deviations of 0.4 mm at 450 kN.

Similar outcomes can also be captured by DIC reference measurements, which present differences smaller than 0.6 mm over the entire segment length. Especially at load steps starting from 350 kN, the completely independent measurement techniques depict an excellent agreement with a percentage error between 1.3 and 1.7%. These results suggest that the designed DFOS approach is capable for real-scale civil infrastructure monitoring.

The investigated tunnel segment was instrumented with six individual DFOS cable layers along both reinforcements to provide a

Figure 6.13: Areal displacement map of tested tunnel segment derived from DFOS at highest load step (Monsberger and Lienhart 2021b).

complete coverage (cf. Figure 6.10). Displacement curves can therefore be individually derived for each layer to form an areal sensing mesh with more than 2400 evaluation points. The combined areal displacement map in Figure 6.13 depicts a uniform, symmetric deformation behavior along the entire segment. This is reasonable due to the consistent vertical loading, which is why the individual displacement curves depict similar results in shape and magnitude. Any combination of the vertical loading with stresses orthogonal to the segment's cross section (i.e. in direction of the tunnel drive) would however result in torsion. In addition to locally strained sections and irregularities along the structure like cracks, such torsion effects could also be captured using the deployed DFOS approach.

Vertical Loading: Assessment of Sensing Principles

To provide an assessment of the spatial resolution impact of different interrogation techniques, the DFOS installation of another segment under vertical loading was alternately interrogated by the OBR and the BOFDA sensing unit. The results in Figure 6.14a demonstrate that also the Brillouin interrogator can solidly cap-

ture the arising deformation behavior with maximum deviations between the different DFOS technologies of 0.5 mm.

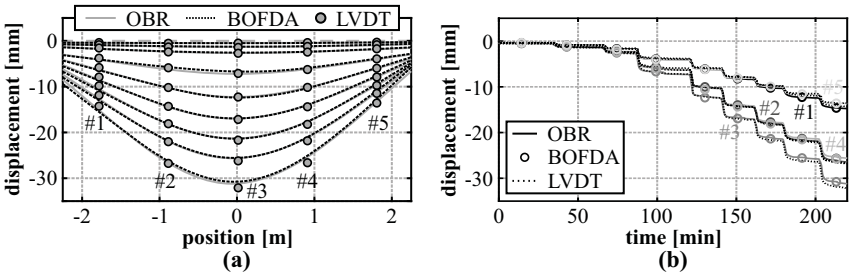

Figure 6.14: Analysis of different sensing techniques during vertical loading from 50 kN to 450 kN in 50 kN steps (Monsberger and Lienhart 2021b): **(a)** Displacement curves calculated from OBR and BOFDA measurements compared to pointwise LVDT readings. **(b)** Displacements at LVDT locations over time.

By comparing the temporal order of the respective displacement values resulting from the DFOS techniques at the LVDT locations (Figure 6.14b), it becomes obvious that the loading process can be well identified and both technologies agree well to the displacements measured by the LVDT sensors over time. At the highest load step of 450 kN, deviations between the LVDTs and both technologies at the LVDT locations range from 0.6% to 3.9% with a mean percentage error of 2.4% (OBR) and 2.7% (BOFDA). The suitability of Brillouin sensing techniques, even with limitations in the spatial resolution, is essential for practical applications inside the tunnel, where the restricted sensing range of the OBR (cf. Table 3.1) can be disadvantageous in many cases.

Horizontal Loading

Another lining segment was also investigated under horizontal loading at the test rig. This setup is assumed to result in vertical bending of the segment in upwards direction and therefore, provides an additional loading scenario for the fiber optic shape sensing approach.

The derived bending curves in Figure 6.15a can reproduce these expectations and the displacements again agree well with the LVDT sensors. The mean percentage error of the DFOS measurements with respect to the LVDTs can be indicated with about 0.9% at the highest load step of 700 kN with a maximum absolute deviation of approx. 0.14 mm. This is even a slight numerical improvement compared to the results of the vertical loading tests.

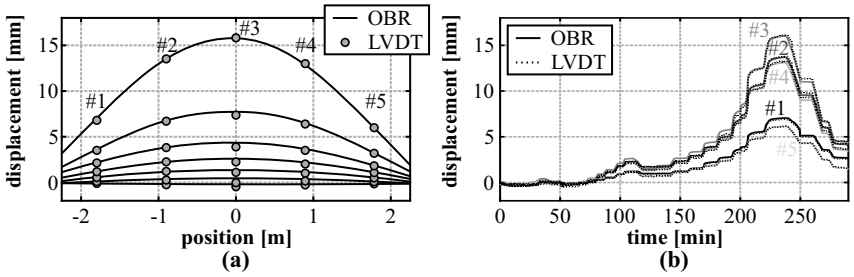

Figure 6.15: Horizontal loading from 100 kN to 700 kN in 50 kN steps (Monsberger and Lienhart 2021b): **(a)** Displacement curves. **(b)** Displacements at LVDT locations over time.

The temporal deformation progress (Figure 6.15b) suggests that the horizontal loading is not performed fully symmetrically since the measured LVDT displacements at the left-hand side (#01 and #02) are slightly higher compared to corresponding ones on the other side (#04 and #05). Although the deviations between both sides are only in the range of 0.7 mm at the maximum load step, the derived DFOS displacements are definitely capable to identify this unsymmetrical loading behavior.

6.5 CONCLUSIONS

This section presented a comprehensive study of strain-based shape sensing along concrete structures. The capabilities of different sensor types, including numerous DFOS cables and FBG sensors, were evaluated within loading tests of concrete beams as well as tunnel

lining segments, where various installation techniques were used to attach the sensors along the reinforcement, inside the concrete or at the structure's surface. The installations were interrogated using different fully-distributed strain sensing systems as well as by quasi-distributed FBG interrogators.

The results demonstrate that shape changes can be reliably determined using all installation techniques and sensing fibers before major cracking of the concrete arises. The strain sensing output may however be extremely different depending on the sensor type, the location as well as the attaching method, which must be taken into account for appropriate data interpretation. Evaluations of different DFOS technologies show that spatial resolution limitations or interpolation between FBG sensing points do indeed restrict the accuracy of the distributed shape sensing approach, but deviations are within the range of 5% or even lower for deformations larger than 1 mm. The suitability of the derived displacement curves was proven not only by pointwise LVDT sensor readings and theoretical model analysis, but also using completely independent verification measurements based on DIC.

The shape sensing concept allows an evaluation of distributed displacement profiles along the entire concrete structure without a visual line-of-sight. Simultaneously, local distortions like cracks can be also identified using the same sensor, which is why the DFOS approach might be useful for numerous applications in civil structural health monitoring.

7

Summary and Outlook

The shape sensing methodology and corresponding monitoring applications of civil infrastructure presented in this thesis demonstrate that distributed fiber optic sensing can enable more than just conventional measurements of strain and temperature profiles along objects. A model-free analysis of distributed bending characteristics along the entire structure is usually not possible without a visual line-of-sight. Within the scope of the thesis, numerous fiber optic shape sensing approaches were designed and practically implemented by integrating in-situ strain information along various linear and curved structures with different material properties, where the rank deficiency of the double integration process has been solved by applying geodetic adjustment methods. The goal of designing, evaluating and realizing fully-distributed shape sensing concepts for structural and geotechnical applications was therefore achieved.

Linear sensing objects with homogeneous material properties along the structure provide the best possible conditions for strain-based shape sensing, as the individual shape of the cross-sectional profile and hence, the neutral axis location remains constant in the event of loading. This implies that the Bernoulli hypothesis can be fulfilled and the curvature derivation is not systemically impeded. DFOS-based shape sensing has been practically realized along a real-scale linear steel anchor specimen with a total length of about 6 m. Comprehensive laboratory tests point out that the designed approach is not only feasible to represent theoretical beam models, but also depicts high repeatability in the range of a few hundredths of a millimeter for consecutive measurements at constant load level as well as low hysteresis between loading and unloading. The absolute accuracy has been verified by independent geodetic measurements and camera-based sensing techniques with maximum errors of approximately 1%. Continuous monitoring of a slope stabilization additionally showed that the designed system is suitable for practical applications in field environment.

Shape sensing approaches along non-linear, curved structures require consideration of the original shape of the object. The shape sensing accuracy therefore not only depends on the measurement uncertainty itself, but also on the knowledge of the initial curvature of the structure. Any combination with point-wise traditional displacement readings like total station measurements can be useful to support the shape sensing algorithm or is even mandatory to solve the boundary value problem of the double integration. An appropriate sensing and evaluation concept has been developed in the scope of this thesis and was also practically implemented into tunnel cross-sections. The data analysis demonstrated that the designed system is capable to asses distributed bending profiles without any geometrical gaps under tunnel site conditions with mean errors in the low millimeter range compared to conventional geodetic measurements.

The presented fiber optic shape sensing studies along concrete structures introduced effects of various DFOS cable setups and dif-

ferent installation techniques on the shape sensing methodology. Variations in the captured curvature distribution depend on the sensor type and location as well as the attaching method, but can be equalized by applying appropriate low-pass filtering or interpolation techniques. The inconsistency within the cross-sectional profile along the structure resulting from structural anomalies or deficiencies like major cracking however essentially affects the shape sensing capabilities. The structural behavior and arising defects must therefore be taken into account within the design and corresponding data interpretation, especially for aging infrastructure or concrete structures with high degree of damage.

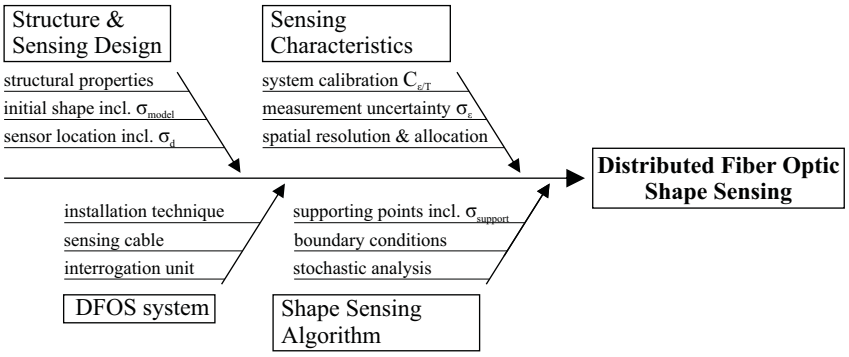

Figure 7.1: Shape sensing design workflow using DFOS along civil infrastructure.

The key factors to design an appropriate and successful fiber optic shape sensing approach based on the realized applications presented in this thesis are depicted within the schematic workflow in Figure 7.1. Firstly, knowledge about the structural behavior under load, the material properties and the initial shape is crucial to determine possible sensor locations within the structure. For instance, shape sensing along the reinforcement of concrete structures can minimize effects of local inhomogeneities, but usually requires mechanical modifications of the reinforcement bar itself. In this con-

text, practical aspects on-site should also be taken into account to fit the sensor installation to the construction process.

Subsequently, the individual components of the DFOS system must be selected with respect to the application. This not only comprises the DFOS interrogation unit with presented benefits and limitations, but also the sensing cable and its suitable installation along the structure. Extensive knowledge about the DFOS system characteristics including the sensitivity coefficients C_ε and C_T, the strain sensing uncertainty and the spatial resolution is essential to provide an adequate shape sensing design.

The shape sensing algorithm should be finally set up with respect to applicable supporting points, their corresponding accuracy as well as boundary conditions or constraints. Stochastic analysis of all affecting measurement quantities, i.e. DFOS strain measurements σ_ε, the sensor location σ_d as well as the initial shape σ_{model} and the supporting points $\sigma_{support}$, enables an estimation of the achievable uncertainty of the resulting bending profiles. Optimizations are still feasible at this point if the design does not meet the project requirements.

This thesis shows that distributed fiber optic shape sensing concepts are suitable for monitoring of structures, especially when no visual line-of-sight can be established. Applications in foundation engineering, e.g. base plates or pile constructions of high-rise buildings, might benefit from an assessment of distributed curvature and bending characteristics along the structure. This will not only allow the verification of the load-bearing capacity from the beginning of the construction, but also the optimization of design parameters, which finally result in savings of environmental and economic resources. In addition, the presented applications only focus on static or quasi-static deformation. New sensor developments may also enable high-frequent measurements that could be utilized to determine mode shapes related to the particular natural frequency of a structure.

Conventional shape monitoring often requires physical access and interferes with the usage of civil infrastructure. The presented shape sensing methodology can provide knowledge about shape deformations without any interference with the regular operation. Apart from that, local distortions like cracks or leakage can still be identified along the structure using the same sensor, which enables enhanced capabilities for applications in civil structural health monitoring.

References

APA (2020). *Unfall beim Bau des Semmering-Basistunnels*. Austria Press Agency. https://www.derstandard.at/story/2000117801971/toedlicher-arbeitsunfall-beim-bau-des-semmering-basistunnels.

Barla G. (2009). "Innovative tunneling construction method to cope with squeezing at the Saint Martin La Porte access adit (Lyon-Turin Base Tunnel)." *Proc., ISRM Regional Symp. - EUROCK 2009 (keynote lecture)*. Dubrovnik, Croatia, 10 p.

Barrias A., Casas J. R., and Villalba S. (2019). "Distributed optical fibre sensors in concrete structures: Performance of bonding adhesives and influence of spatial resolution." *Structural Control and Health Monitoring* 26(3): e2310, 1–16. DOI: 10.1002/stc.2310.

Bassil A., Chapeleau X., Leduc D., and Abraham O. (2020). "Concrete Crack Monitoring Using a Novel Strain Transfer Model for Distributed Fiber Optics Sensors." *Sensors* 20(8). DOI: 10.3390/s20082220.

Bassil A., Wang X., Chapeleau X., Niederleithinger E., Abraham O., and Leduc D. (2019). "Distributed Fiber Optics Sensing and Coda

Wave Interferometry Techniques for Damage Monitoring in Concrete Structures." *Sensors* 19(2). DOI: 10.3390/s19020356.

Bednarski Ł., Sieńko R., Grygierek M., and Howiacki T. (2021). "New Distributed Fibre Optic 3DSensor with Thermal Self-Compensation System: Design, Research and Field Proof Application Inside Geotechnical Structure." *Sensors* 21(15): 5089. DOI: 10.3390/s21155089.

Berrocal C. G., Fernandez I., Bado M. F., Casas J. R., and Rempling R. (2021). "Assessment and visualization of performance indicators of reinforced concrete beams by distributed optical fibre sensing." *Structural Health Monitoring*: 1475921720984431, 1–18. DOI: 10.1177/1475921720984431.

Billon A., Hénault J.-M., Quiertant M., Taillade F., Khadour A., Martin R.-P., and Benzarti K. (2015). "Qualification of a distributed optical fiber sensor bonded to the surface of a concrete structure: a methodology to obtain quantitative strain measurements." *Smart Materials and Structures* 24(11): 115001, 1–13. DOI: 10.1088/0964-1726/24/11/115001.

Brault A., Hoult N. A., Greenough T., and Trudeau I. (2019). "Monitoring of Beams in an RC Building during a Load Test Using Distributed Sensors." *Journal of Performance of Constructed Facilities* 33(1): 04018096, 1–11. DOI: 10.1061/(ASCE)CF.1943-5509.0001250.

Brunner F. K. and Wieser A. (2006). "Ein Vorschlag zur simultanen Geometriebestimmung beim Düsenstrahlverfahren." *Bautechnik* 83(9): 644–648. DOI: 10.1002/bate.200690146.

Buchmayer F., Monsberger C. M., and Lienhart W. (2021). "Advantages of tunnel monitoring using distributed fibre optic sensing." *Journal of Applied Geodesy* 15(1): 1–12. DOI: 10.1515/jag-2019-0065.

Caporossi P., Mazzanti P., and Bozzano F. (2018). "Digital Image Correlation (DIC) Analysis of the 3 December 2013 Montescaglioso Landslide (Basilicata, Southern Italy): Results from a Multi-Dataset Investigation." *ISPRS International Journal of Geo-Information* 7(9). DOI: 10.3390/ijgi7090372.

Corning (2016). *White Paper WP 5082: Frequently Asked Questions on Fiber Reliability*. Corning Inc., New York, United States, 2 p.

Corning (2017). *White Paper WP 8002: Optical Fiber Mechanical Reliability*. Corning Inc., New York, United States, 62 p.

De Battista N., Elshafie M., Soga K., Williamson M., Hazelden G., and Hsu Y. (2015). "Strain monitoring using embedded distributed fibre optic sensors in a sprayed concrete tunnel lining during the excavation of cross-passages." *Proc., 7th Int. Conf. on Structural Health Monitoring of Intelligent Infrastructure (SHMII-7)*. Torino, Italy, 10 p.

De Battista N., Kechavarzi C., Cheal N., Harvey R., and Wong S. (2019). "Monitoring the Axial Shortening of Principal Tower Using Embedded Distributed Fibre Optic Sensors." *Proc., Int. Conf. on Smart Infrastructure and Construction 2019 (ICSIC)*. Cambridge, United Kingdom, pp. 233–240. DOI: 10.1680/icsic.64669.233.

Delepine-Lesoille S., Girard S., Landolt M., Bertrand J., Planes I., Boukenter A., Marin E., Humbert G., Leparmentier S., Auguste J.-L., and Ouerdane Y. (2017). "France's State of the Art Distributed Optical Fibre Sensors Qualified for the Monitoring of the French Underground Repository for High Level and Intermediate Level Long Lived Radioactive Wastes." *Sensors* 17(6): 1–32. DOI: 10.3390/s17061377.

DGGT (2021). *Empfehlungen des Arbeitskreises Geomesstechnik*. 1st ed., Ernst & Sohn, Berlin, Germany.

DIN (2010). *Engineering survey – Part 4: Deformation measurements (English translation of DIN 18710-4:2010-09)*. German Standards (DIN-Normen). Berlin, Germany.

Febus (2021). *Febus Optics - The manufacturer of all your distributed fiber sensing solutions, Brochure*. Febus Optics SAS, Pau, France, 5 p.

Feng X., Han Y., Wang Z., and Liu H. (2018). "Structural performance monitoring of buried pipelines using distributed fiber optic sensors." *Journal of Civil Structural Health Monitoring* 8(3): 509–516. DOI: 10.1007/s13349-018-0286-3.

Fibercore (2021). *MULTICORE FIBER*. Fibercore Ltd., Southampton, United Kingdom, 2 p.

fibrisTerre (2020). *fTB 5020, Fiber-optic sensing system for distributed strain and temperature monitoring*. fibrisTerre Systems GmbH, Berlin, Germany, 4 p.

Fischer O., Thoma S., and Crepaz S. (2019). "Distributed fiber optic sensing for crack detection in concrete structures." *Civil Engineering Design* 1(3-4): 97–105. DOI: 10.1002/cend.201900008.

Forbes B., Vlachopoulos N., Hyett A., and Diederichs M. (2017). "A new optical sensing technique for monitoring shear of rock bolts." *Tunnelling and Underground Space Technology* 66: 34–46. DOI: 10.1016/j.tust.2017.03.007.

Froggatt M. E., Klein J. W., Gifford D. K., and Kreger S. T. (2011). "Optical position and/or shape sensing." US8,773,650 B2. Intuitive Surgical Operations Inc., Sunnyvale, California, United States.

Gehwolf P., Monsberger C., Barwart S., Wenighofer R., Galler R., Lienhart W., Haberler-Weber M., Moritz B., Barwart C., and Lange A. (2016). "Deformation measurements of tunnel segments at a newly developed test rig." *Geomechanics and Tunnelling* 9(3): 180–187. DOI: 10.1002/geot.201600012.

Gehwolf P., Wenighofer R., Barwart S., Galler R., Haberler-Weber M., Moritz B., Barwart C., and Lange A. (2015). "Konzeptionierung, Realisierung und erste Ergebnisse eines neu entwickelten Tübbingprüfstands." *BHM Berg- und Hüttenmännische Monatshefte* 160: 530–534. DOI: 10.1007/s00501-015-0428-4.

Glišić B. (2011). "Influence of the gauge length on the accuracy of long-gauge sensors employed in monitoring of prismatic beams." *Measurement Science and Technology* 22(3): 035206, 1–13. DOI: 10.1088/0957-0233/22/3/035206.

Glišić B. (2022). "Concise Historic Overview of Strain Sensors Used in the Monitoring of Civil Structures: The First One Hundred Years." *Sensors* 22(6). DOI: 10.3390/s22062397.

Glišić B. and Inaudi D. (2007). *Fibre Optic Methods for Structural Health Monitoring*. 1st ed., John Wiley & Sons, Ltd, Hoboken, New Jersey, United States. DOI: 10.1002/9780470517819.

Gobiet G., Nipitsch G., and Wagner O. K. (2017). "The Semmering Base Tunnel – Special challenges in construction." *Geomechanics and Tunnelling* 10(3): 291–297. DOI: 10.1002/geot.201700008.

Gobiet G. and Wagner O. K. (2013). "The New Semmering Base Tunnel project." *Geomechanics and Tunnelling* 6(5): 551–558. DOI: 10.1002/geot.201300041.

GOM (2018). *GOM Testing—Technical Documentation as of V8 SR1, Digital Image Correlation and Strain Computation Basics*. GOM GmbH, Braunschweig, Germany, 127 p.

Hartog A. (2017). *An introduction to distributed optical fibre sensors*. 1st ed., CRC Press, Taylor & Francis Group, Boca Raton, Florida, United States. DOI: 10.1201/9781315119014.

HBM (2021). *FS62WSS Weldable Strain Sensor (Aramid or Armor cable)*. HBM FiberSensing S.A., Maia, Portugal, 2 p.

Henault J.-M., Quiertant M., Delepine-Lesoille S., Salin J., Moreau G., Taillade F., and Benzarti K. (2012). "Quantitative strain measurement and crack detection in RC structures using a truly distributed fiber optic sensing system." *Construction and Building Materials* 37: 916–923. DOI: 10.1016/j.conbuildmat.2012.05.029.

Henzinger M. R., Schachinger T., Lienhart W., Buchmayer F., Weilinger W., Stefaner R., Haberler-Weber M., Haller E.-M., Steiner M., and Schubert W. (2018). "Fibre-optic supported measurement methods for monitoring rock pressure." *Geomechanics and Tunnelling* 11(3): 251–263. DOI: 10.1002/geot.201800015.

Heunecke O., Kuhlmann H., Welsch W., Eichhorn A., and Neuner H. (2013). *Handbuch Ingenieurgeodäsie: Auswertung geodätischer Überwachungsmessungen*. 2nd ed., Wichmann Verlag, Berlin-Charlottenburg, Germany.

Hirschmüller S. (2019). "Beech circular hollow laminated veneer lumber sections for temporary soil nailing applications." PhD thesis, Graz University of Technology, Graz, Austria.

Hirschmüller S., Pravida J., and Marte R. (2016). "Laminated veneer lumber poles for temporary soil nailing - investigation of material properties." *Proc., World Conf. on Timber Engineering (WCTE 2016)*. Vienna, Austria, 8 p.

Horiguchi T., Kurashima T., and Tateda M. (1989). "Tensile strain dependence of Brillouin frequency shift in silica optical fibers." *IEEE Photonics Technology Letters* 1(5): 107–108. DOI: 10.1109/68.34756.

Inaudi D. (1997). "Fiber optic sensor network for the monitoring of civil engineering structures." PhD thesis, Ecole Polytechnique Federale de Lausanne (EPFL), Lausanne, Switzerland.

Inaudi D. and Glišić B. (2010). "Long-range pipeline monitoring by distributed fiber optic sensing." *Pressure Vessel Technology* 132: 01170 1–9. DOI: 10.1115/1.3062942.

Inaudi D. and Vurpillot S. (1999). "Monitoring of Concrete Bridges with Long-Gage Fiber Optic Sensors." *Journal of Intelligent Material*

Systems and Structures 10(4): 280–292. DOI: 10.1177/1045389X9901000404.

Inaudi D., Vurpillot S., Glisic B., Kronenberg P., and LLoret S. (1999). "Long-term monitoring of a concrete bridge with 100+ fiberoptic long-gage sensors." *Proceedings of SPIE - The International Society for Optical Engineering* 3587: 50–59.

Innotec (2017). *TECHNISCHE INFO Metal Weld 50 ml Weiß*. Innotec GmbH, Moers, Germany, 2 p.

Jiao T. and Zhou Z. (2021). "An optical-electrical co-sensing tape for cross-sectional deformation monitoring of shield tunnels." *Tunnelling and Underground Space Technology* 117: 104148. DOI: 10.1016/j.tust.2021.104148.

Karbhari V. M. and Ansari F. (2009). *Structural Health Monitoring of Civil Infrastructure Systems*. 1st ed., Woodhead Publishing Ltd, Cambridge, England. DOI: 10.1533/9781845696825.

Kashyap R. and López-Higuera J. M. (2002). "Fiber Grating Technology: Theory, Photosensitivity, Fabrication and Characterization". In: López-Higuera J. M. (ed.) *Handbook of Optic Fibre Sensing Technology*. John Wiley & Sons Ltd, Hoboken, New Jersey, United States: pp. 349–377.

Kechavarzi C., Soga K., Battista N. de, Pelecanos L., Elshafie M. Z. E. B., and Mair R. J. (2016). *Distributed Fibre Optic Strain Sensing for Monitoring Civil Infrastructure*. 1st ed., ICE Publishing, London, United Kingdom. DOI: 10.1680/dfossmci.60555.

Klais F., Wolf P., and Lienhart W. (2017). "The Grautschenhof contract – Construction of an intermediate access under complex local conditions." *Geomechanics and Tunnelling* 10(6): 686–693. DOI: 10.1002/geot.201700052.

Klug F. and Woschitz H. (2015). "Test and Calibration of 20 FBG based strain transducers." *Proc., 7th Int. Conf. on Structural Health Monitoring of Intelligent Infrastructure (SHMII-7)*. Torino, Italy, 11 p.

Kreger S. T., Gifford D. K., Froggatt M. E., Soller B. J., and Wolfe M. S. (2006). "High resolution distributed strain or temperature measurements in single-and multi-mode fiber using swept-wavelength interferometry." *Proc., Optical Fiber Sensors*. Cancun, Mexico, ThE42, 4 p.

Kurashima T., Horiguchi T., and Tateda M. (1990). "Thermal effects on the Brillouin frequency shift in jacketed optical silica fibers." *Applied Optics* 29(15): 2219–2222. DOI: 10.1364/AO.29.002219.

Lava P., Cooreman S., Coppieters S., De Strycker M., and Debruyne D. (2009). "Assessment of measuring errors in DIC using deformation fields generated by plastic FEA." *Optics and Lasers in Engineering* 47(7): 747–753. DOI: 10.1016/j.optlaseng.2009.03.007.

Leica (2015). *Leica TS15 User Manual*. Leica Geosystems AG, Heerbrugg, Switzerland, 4 p.

Li Z., Soga K., and Kechavarzi C. (2018). "Distributed fibre optic sensing of a deep excavation adjacent to pre-existing tunnels." *Géotechnique Letters* 8(3): 171–177. DOI: 10.1680/jgele.18.00031.

Lienhart W., Buchmayer F., Klug F., and Monsberger C. M. (2019). "Distributed fibre-optic sensing applications at the Semmering Base Tunnel, Austria." *Proceedings of the Institution of Civil Engineers - Smart Infrastructure and Construction* 172(4): 148–159. DOI: 10.1680/jsmic.20.00006.

Lienhart W. and Galler R. (2016). "Tübbingelement mit Dehnungsmessung." AT516158 (B1). Technische Universität Graz, Graz, Austria.

Lim H. S. and Yang Y. H. (2007). "Soil nailing reinforcement member using wood having environment - friendly effect and proceeding construction work easily by using a bamboo or a wood as a reinforcement member." KR 2005119021A.

Liu T., Huang H., and Yang Y. (2020). "Crack Detection of Reinforced Concrete Member Using Rayleigh-Based Distributed Optic Fiber Strain Sensing System." *Advances in Civil Engineering*: 8312487, 1–11. DOI: 10.1155/2020/8312487.

Luna (2019). *OBR 4600 Optical Backscatter Reflectometer, Datasheet*. Luna Technologies Inc., Roanoke, VA, USA, 4 p.

Luna (2021). *si255 HYPERION Optical Sensing Instrument, Datasheet*. Luna Technologies Inc., Roanoke, VA, USA, 2 p.

Mang H. and Hofstetter G. (2018). *Festigkeitslehre*. 5th ed., Springer Vieweg, Berlin, Germany. DOI: 10.1007/978-3-662-57564-2.

Matta F., Bastianini F., Galati N., Casadei P., and Nanni A. (2008). "Distributed Strain Measurement in Steel Bridge with Fiber Optic Sensors: Validation through Diagnostic Load Test." *Journal of*

Performance of Constructed Facilities 22(4): 264–273. DOI: 10.1061/(ASCE)0887-3828(2008)22:4(264).

Megson T. H. G. (2005). *Structural and stress analysis*. 2nd ed., Elsivier Ltd., London, United Kingdom. DOI: 10.1016/B978-0-7506-6221-5.X5000-0.

Minardo A., Bernini R., Amato L., and Zeni L. (2012). "Bridge Monitoring Using Brillouin Fiber-Optic Sensors." *IEEE Sensors Journal* 12(1): 145–150. DOI: 10.1109/JSEN.2011.2141985.

Monsberger C. M., Bauer P., Buchmayer F., and Lienhart W. (2022). "Large-scale distributed fiber optic sensing network for short and long-term integrity monitoring of tunnel linings." *Journal of Civil Structural Health Monitoring*. DOI: 10.1007/s13349-022-00560-w.

Monsberger C. M. and Lienhart W. (2017). "In-situ Deformation Monitoring of Tunnel Segments using High-resolution Distributed Fibre Optic Sensing." *Proc., 8th Int. Conf. on Structural Health Monitoring of Intelligent Infrastructure (SHMII-8)*. Brisbane, Australia, 12 p.

Monsberger C. M. and Lienhart W. (2019). "Design, Testing, and Realization of a Distributed Fiber Optic Monitoring System to Assess Bending Characteristics Along Grouted Anchors." *Journal of Lightwave Technology* 37(16): 4603–4609. DOI: 10.1109/JLT.2019.2913907.

Monsberger C. M. and Lienhart W. (2021a). "Distributed fiber optic shape sensing along shotcrete tunnel linings: Methodology, field applications, and monitoring results." *Journal of Civil Structural Health Monitoring* 11(2): 337–350. DOI: 10.1007/s13349-020-00455-8.

Monsberger C. M. and Lienhart W. (2021b). "Distributed Fiber Optic Shape Sensing of Concrete Structures." *Sensors* 21(18): 6098. DOI: 10.3390/s21186098.

Monsberger C. M., Lienhart W., and Caporossi P. (2018a). "Distributed Fiber Optic Sensing along Grouted Anchors to Assess Curvature and Bending Characteristics." *Proc., 26th Int. Conf. on Optical Fiber Sensors*. Lausanne, Switzerland, TuE98, 4 p.

Monsberger C. M., Lienhart W., and Hayden M. (2020). "Distributed fiber optic sensing along driven ductile piles: Design, sensor installation and monitoring benefits." *Journal of Civil Structural*

Health Monitoring 10(4): 627–637. DOI: 10.1007/s13349-020-00406-3.

Monsberger C. M., Lienhart W., Hirschmüller S., and Marte R. (2018b). "Monitoring of soil nailed slope stabilizations using distributed fiber optic sensing." *Proc., SPIE 10598, Sensors and Smart Structures Technologies for Civil, Mechanical, and Aerospace Systems*. Denver, Colorado, United States, pp. 1059835, 1–12.

Monsberger C. M., Lienhart W., Kluckner A., and Schubert W. (2019). "In-situ assessment of distributed strain and curvature characteristics in shotcrete tunnel linings based on fiber optic strain sensing." *Proc., ISRM 14th Int. Congr. on Rock Mechanics*. Iguazu, Brazil, pp. 1324–1331.

Monsberger C. M., Lienhart W., and Moritz B. (2018c). "In-situ assessment of strain behaviour inside tunnel linings using distributed fibre optic sensors." *Geomechanics and Tunnelling* 11(6): 701–709. DOI: 10.1002/geot.201800050.

Monsberger C. M., Woschitz H., and Hayden M. (2016). "Deformation measurement of a driven pile using distributed fibre-optic sensing." *Journal of Applied Geodesy* 10(1): 61–69. DOI: 10.1515/jag-2015-0021.

Monsberger C. M., Woschitz H., Lienhart W., Račanský V., and Hayden M. (2017). "Performance assessment of geotechnical structural elements using distributed fiber optic sensing." *Proc., SPIE 10168, Sensors and Smart Structures Technologies for Civil, Mechanical, and Aerospace Systems*. Portland, Oregon, United States, pp. 101680Z, 1–12.

Moore J. P. and Rogge M. D. (2012). "Shape sensing using multi-core fiber optic cable and parametric curve solutions." *Optics Express* 20(3): 2967–2973. DOI: 10.1364/OE.20.002967.

Moritz B., Heissenberger R., Schachinger T., and Lienhart W. (2021). "Long-term monitoring of railway tunnels." *Geomechanics and Tunnelling* 14(1): 35–46. DOI: 10.1002/geot.202000049.

Moser F., Lienhart W., Woschitz H., and Schuller H. (2016). "Longterm monitoring of reinforced earth structures using distributed fiber optic sensing." *Journal of Civil Structural Health Monitoring* 6(3): 321–327. DOI: 10.1007/s13349-016-0172-9.

Nassif N. and Fayyad D. K. (2013). *Introduction to numerical analysis and scientific computing*. 1st ed., CRC Press LLC, Boca Raton, Florida, United States. DOI: 10.1201/b15285.

Neubrex (2018). *Neural Optical Fiber Scope NEUBRESCOPE NBX-7021*. Neubrex Co., Ltd., Kobe, Japan, 4 p.

Niemeier W. (2008). *Ausgleichungsrechnung*. 2nd ed., De Gruyter, Berlin, Germany. DOI: 10.1515/9783110206784.

Nöther N. (2010). "Distributed Fiber Sensors in River Embankments: Advancing and Implementing the Brillouin Optical Frequency Domain Analysis." PhD thesis, BAM Bundesanstalt für Materialforschung und -prüfung, Berlin, Germany.

Omnisens (2016). *DITEST INTERROGATOR, Manual (Version 1-3)*. Omnisens SA, 17 p.

Othonos A. and Kalli K. (1999). *Fiber Bragg Gratings: Fundamentals and Applications in Telecommunications and Sensing*. 1st ed., Artech House Publishers, Boston, USA.

OZ (2018). *Fiber Optic Distributed Strain and Temperature Sensors (DSTS) BOTDA Module*. OZ Optics Ltd., Ottawa, Canada, 11 p.

Pauer H. (2017). "Auf metrischen und differentialgeometrischen Konzepten basierende neue mathematische Algorithmen zur Sensordatenfusion mit Anwendungen in der Faser-Bragg-Gitter-Formsensorik." PhD thesis, Karlsruher Institut für Technologie (KIT), Karlsruhe, Germany.

Pauer H. and Ledermann C. (2020). "Deformation device, including an optical waveguide and method for measuring deformation of a tubular structure at multiple measuring points." US 10,551,168 B2. Karlsruher Institut für Technologie (KIT), Karlsruhe, Germany.

Pei H.-F., Yin J.-H., and Jin W. (2013). "Development of novel optical fiber sensors for measuring tilts and displacements of geotechnical structures." *Measurement Science and Technology* 24(9): 10 p.

Poldon J. J., Hoult N. A., and Bentz E. C. (2019). "Distributed Sensing in Large Reinforced Concrete Shear Test." *ACI Structural Journal* 116(5): 235–245. DOI: 10.14359/51716765.

Presl R. (2009). "Entwicklung eines automatisierten Messsystems zur Charakterisierung faseroptischer Dehnungssensoren." MA thesis, FH Upper Austria, Wels, Austria.

Rabensteiner K. (1996). "Advanced tunnel surveying and monitoring." *Felsbau* 14(2): 98–102.

Radončić N., Kern M., Weissnar M., and Moritz B. (2015). "Strain gauges in pre-cast concrete segments: working principle, evaluation and interpretation." *Geomechanics and Tunnelling* 8(3): 265–272. DOI: 10.1002/geot.201500004.

Rastogi V. K. (2008). "Instrumentation and monitoring of underground structures and metro railway tunnels." *Proc., Proc. of 34th AITES-ITA World Tunnel Congr.* Agra, India, pp. 795–808.

Regier R. and Hoult N. A. (2014). "Distributed Strain Behavior of a Reinforced Concrete Bridge: Case Study." *Journal of Bridge Engineering* 19(12): 05014007, 1–9. DOI: 10.1061/(ASCE)BE.1943-5592.0000637.

Schubert W. and Moritz, B. (eds) (2014). *Handbook – Geotechnical Monitoring in Conventional Tunnelling*. 1st ed., OeGG – Austrian Society for Geomechanics, Salzburg, Austria.

Schubert W., Steindorfer A., and Button E. A. (2002). "Displacement monitoring in tunnels–an overview." *Felsbau* 20(2): 7–15.

Sensuron (2021). *Sensuron Summit Multi-sensing, Datasheet*. Sensuron LLC, Austin, Texas, United States, 2 p.

SHM (2021). *3DSensor*. SHM Systems Company, Krakow, Poland, 2 p.

Sieńko R., Bednarski Ł., Howiacki T., Zuziak K., and Labocha S. (2021). "Possibilities of Composite Distributed Fibre Optic 3DSensor on the Example of Footing Pulled Out from the Ground: A Case Study." *Proc., Civil Structural Health Monitoring*. Naples, Italy, pp. 775–792.

Sigurdardottir D. H. (2015). "Strain-based monitoring methods for beam-like structures." PhD thesis, Princeton University, Department of Civil and Environmental Engineering, Princeton, United States.

Sigurdardottir D. H., Stearns J., and Glišić B. (2017). "Error in the determination of the deformed shape of prismatic beams using the double integration of curvature." *Smart Materials and Structures* 26(7): 075002, 1–13. DOI: 10.1088/1361-665x/aa73ec.

Smartec (2017). *SMARTprofile II Strain Sensing cable*. SMARTEC SA, Manno, Switzerlan, 2 p.

Smartec (2018). *SOFO Deformation Sensor*. SMARTEC SA, Manno, Switzerlan, 2 p.

Soga K., Kwan V., Pelecanos L., Rui Y., Schwamb T., Seo H., and Wilcock M. (2015). "Geotechnical Engineering for Infrastructure and Development". In: Winter M. G., Smith D. M., Eldred P. J. L., and Toll D. G. (eds.) *The Role of Distributed Sensing in Understanding*

the Engineering Performance of Geotechnical Structures. ICE Publishing, London, United Kingdom: pp. 13–48. DOI: 10.1680/ecsmge.60678.vol1.002.

Solifos (2019a). *BRUsens DSS 3.2mm V9 grip 3_50_2_005*. Solifos AG, Windisch, Switzerland, 1 p.

Solifos (2019b). *BRUsens DSS 7.2mm V3 grip 3_50_2_002*. Solifos AG, Windisch, Switzerland, 1 p.

Solifos (2019c). *BRUsens DTS STL PA 3_50_1_001*. Solifos AG, Windisch, Switzerland, 1 p.

Soller B. J., Wolfe M. S., and Froggatt M. E. (2005). "Polarization resolved measurement of Rayleigh backscatter in fiber-optic components." *Proc., Optical Fiber Communication Conf. and Expo. and The Nat. Fiber Optic Engineers Conf.* Anaheim, California, United States, pp. NWD3, 1–6.

Sun Y., Shi B., Zhang D., Tong H., Wei G., and Xu H. (2016). "Internal Deformation Monitoring of Slope Based on BOTDR." *Journal of Sensors* 2016: 9496285, 1–8. DOI: 10.1155/2016/9496285.

Sylex (2021). *SC-01 Strain cable sensor*. Sylex s.r.o., Bratislava, Slovakia, 2 p.

TLC (2020). *Data Sheet: Tight Buffer*. The Light Connection Inc., Oriskany, New York, United States, 1 p.

Vurpillot S., Krueger G., Benouaich D., Clement D., and Inaudi D. (1998). "Vertical Deflection of a Pre-Stressed Concrete Bridge Obtained Using Deformation Sensors and Inclinometer Measurements." *ACI Structural Journal* 95: 518–526.

Wagner L., Kluckner A., Monsberger C. M., Wolf P., Prall K., Schubert W., and Lienhart W. (2020). "Direct and Distributed Strain Measurements Inside a Shotcrete Lining: Concept and Realisation." *Rock Mechanics and Rock Engineering* 53: 641–652. DOI: 10.1007/s00603-019-01923-4.

Webb G. T., Vardanega P. J., Hoult N. A., Fidler P. R. A., Bennett P. J., and Middleton C. R. (2017). "Analysis of Fiber-Optic Strain-Monitoring Data from a Prestressed Concrete Bridge." *Journal of Bridge Engineering* 22(5): 05017002, 1–14. DOI: 10.1061/(ASCE)BE.1943-5592.0000996.

Woschitz H., Klug F., and Lienhart W. (2015). "Design and Calibration of a Fiber-Optic Monitoring System for the Determination of

Segment Joint Movements Inside a Hydro Power Dam." *Journal of Lightwave Technology* 33(12): 2652–2657.

Wuilpart M. (2011). "Advanced Fiber Optics: Concepts and Technology". In: Thévanez L. (ed.) *Rayleigh scattering in optical fibers and applications to distributed measurements*. EPFL Press, Lausanne, Switzerland: pp. 207–262.

Zhang S., Liu H., Coulibaly A. A. S., and DeJong M. (2021). "Fiber optic sensing of concrete cracking and rebar deformation using several types of cable." *Structural Control and Health Monitoring* 28(2): e2664, 1–23. DOI: 10.1002/stc.2664.

Zhang W., Gao J., Shi B., Cui H., and Zhu H. (2006). "Health Monitoring of Rehabilitated Concrete Bridges Using Distributed Optical Fiber Sensing." *Computer-Aided Civil and Infrastructure Engineering* 21(6): 411–424. DOI: 10.1111/j.1467-8667.2006.00446.x.

Zhao Z., Soto M. A., Tang M., and Thévenaz L. (2016). "Distributed shape sensing using Brillouin scattering in multi-core fibers." *Optical Express* 24(22): 25211–25223. DOI: 10.1364/OE.24.025211.

Zheng Y., Zhu Z.-W., Deng Q.-X., and Xiao F. (2019). "Theoretical and experimental study on the fiber Bragg grating-based inclinometer for slope displacement monitoring." *Optical Fiber Technology* 49: 28–36. DOI: 10.1016/j.yofte.2019.01.031.

Zheng Y., Zhu Z.-W., Xiao W., and Deng Q.-X. (2020). "Review of fiber optic sensors in geotechnical health monitoring." *Optical Fiber Technology* 54: 102127. DOI: 10.1016/j.yofte.2019.102127.